



**FACULTY OF ELECTRICAL ENGINEERING
UNIVERSITY OF BANJA LUKA**

ELECTRONICS

FACULTY OF ELECTRICAL ENGINEERING UNIVERSITY OF BANJA LUKA

Address: Patre 5, 78000 Banja Luka, Bosnia and Herzegovina

Phone: +387 51 211824

Fax: +387 51 211408

Web: www.etfbl.net

ELECTRONICS

Web: www.electronics.etfbl.net

E-mail: electronics@etfbl.net

Editor-in-Chief:

Branko L. Dokić, Ph. D.

Faculty of Electrical Engineering, University of Banja Luka, Bosnia and Herzegovina

E-mail: branko.dokic@etfbl.net

Co Editor-In-Chief:

Prof. Tatjana Pešić-Brdanin, University of Banja Luka, Bosnia and Herzegovina

E-mail: tatjanapb@etfbl.net

International Editorial Board:

- Prof. Goce Arsov, St. Cyril and Methodius University, Macedonia
- Prof. Zdenka Babić, University of Banja Luka, Bosnia and Herzegovina
- Prof. Petar Biljanović, University of Zagreb, Croatia
- Prof. Milorad Božić, University of Banja Luka, Bosnia and Herzegovina
- Prof. Octavio Nieto-Taladriz Garcia, Polytechnic University of Madrid, Spain
- Dr Zoran Jakšić, IHTM, Serbia
- Prof. Vladimir Katić, University of Novi Sad, Serbia
- Prof. Tom J. Kazmierski, University of Southampton, United Kingdom
- Prof. Vančo Litovski, University of Niš, Serbia
- Dr Duško Lukač, University of Applied Sciences, Germany
- Prof. Danilo Mandić, Imperial College, London, United Kingdom
- Prof. Bratislav Milovanović, University of Niš, Serbia
- Prof. Vojin Oklobdžija, University of Texas at Austin, USA
- Prof. Predrag Pejović, University of Belgrade, Serbia
- Prof. Ninoslav Stojadinović, University of Niš, Serbia
- Prof. Robert Šobot, Western University, Canada
- Prof. Slobodan Vukosavić, University of Belgrade, Serbia
- Prof. Volker Zerbe, University of Applied Sciences of Erfurt, Germany

Secretary:

Aleksandar Pajkanović

Drago Čavka

Svjetlana Kovačević

Jovica Bulović

Publisher:

Faculty of Electrical Engineering, University of Banja Luka, Bosnia and Herzegovina

Number of printed copies: 100

Preventive Thermographic Diagnostic of a HV Busbar Disconnecter

Predrag Šaraba, Zoran Ljuboje, Božidar Popović and Dražan Krsmanović

Abstract — For the purpose of increasing quality, continuity and, at the same time, of increasing reliability and decreasing the losses in an electric power system (EPS), there is an emerging need for preventive diagnostic testing. From the standpoint of an electric power system availability, it is desirable to perform as many tests as possible without a violation of operating conditions of the system itself. The paper presents the thermographic testing of a HV disconnector, as an online testing with the aim of preventive maintenance and condition diagnosis of particular elements, as well as the suggestions for taking adequate measures with the aim of removing potential malfunctions.

For the testing results to be quality and to give a reliable information, the load of a facility must be bigger that 50% of the nominal power. On the basis of obtained thermograms, the analysis of the disconnector and its contacts is performed, as well as of the contacts towards other elements in the facility.

Key words: Paper - thermography, diagnostics, disconnector, availability, preventive.

Original Research Paper
DOI: 10.7251/ELS1620003S

I. INTRODUCTION

Electric energy consumers require a reliable and quality electric energy supply, and, at the same time, it is the basic requirement imposed to an electric power system (EPS). The operation reliability of an EPS largely depends on the condition (characteristics, age, functionality) of high voltage equipment, due to the fact that the characteristics of high voltage equipment change during exploitation because of different factors. The age and exploitation time also affect the reliability and availability of and EPS. For this purpose, it is necessary to perform the so-called high voltage condition evaluation. The evaluation can be

(Manuscript received 01 September 2015. Received in revised form 01 December 2015. Accepted for publication 12 May 2016.

Predrag Šaraba is with the Elektroprenos- Elektroprijenos B&H a.d., Banja Luka, Banja Luka, Bosnia and Herzegovina (e-mail: pedja_saraba@yahoo.com).

Zoran Ljuboje is with the Faculty of Electrical Engineering, University of East Sarajevo, East Sarajevo, Bosnia and Herzegovina (e-mail: zoran.ljuboje@etf.unssa.rs.ba).

Božidar Popović is with the Faculty of Electrical Engineering, University of East Sarajevo, East Sarajevo, Bosnia and Herzegovina (e-mail: bozidar.popovic@etf.unssa.rs.ba).

Dražan Krsmanović is with the Elektroprenos- Elektroprijenos B&H a.d., Banja Luka, Banja Luka, Bosnia and Herzegovina (e-mail: drazan.krsmanovic@teol.net).

performed on the basis of tests performed in voltage-free conditions (off-line) and the tests which do not require voltage-free conditions (on-line). From the standpoints of efficiency, availability and economy, on-line methods for high voltage equipment evaluation are preferred. Although these methods are less reliable, their application gives an overview on equipment condition pursuant to which preventive activities can be defines and decisions made for taking service activities or additional tests.

A facility in an EPS loses its defined characteristics and functionality during exploitation, what is a consequence of influence of operating conditions, environment and aging during the life cycle. All the facilities and their elements have a lifetime, and they are expected to work within it in accordance with the indicated characteristics, without a greater number of stoppages and cancellations. The function of cancellation intensity change $\lambda(t)$ in time, i.e. the number of cancellations in plants during a life cycle is shown in Figure 1. In practice, the dependence has the form as in the figure, where three areas can be singled out: the area of early cancellations in the period of equipment exploitation after the plant has been put into operation (I), the area of normal exploitation where the number of cancellations is small and relatively constant (II), and, at the end of the life cycle, the area with the increased number of cancellations which occur because of the age of the observed element (III). By aging, the equipment gradually loses its characteristics and properties, so its cancellation occurs more often, and that affects the decrease of availability, facility reliability, and increase of maintenance costs. To act preventively with the aim to eliminate such phenomena, preventive and regular maintenance is performed. [1]

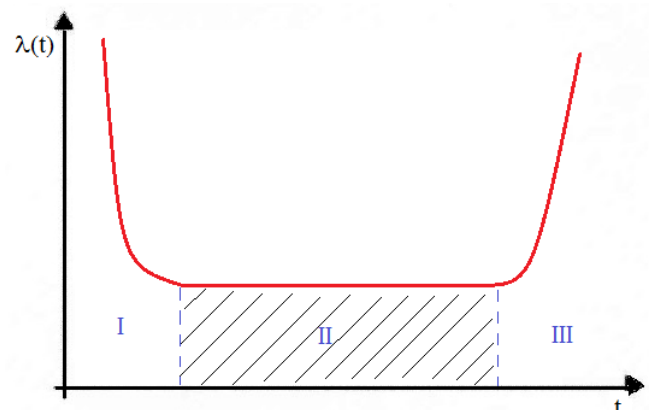


Figure 1. Function of cancellation intensity of an electric power system element.

Thermographic testing presents a diagnostic on-line testing which is becoming largely applied in monitoring and diagnostics of high voltage plants elements. The problems which occur at the end of a thermographic testing are related to determining of a deadline for servicing the equipment where temperature anomalies have been noticed. Observed in the long term, the temperature anomalies (dissipation) can be used as the indicators of exploited equipment quality, as well as of performed service operations. On the basis of dissipation and features of tested equipment, a decision can be made regarding the service, repair or replacement of each particular element. [2]

II. PHYSICAL PROPERTIES OF THERMOGRAPHY

Thermography presents the recording of thermal differences in different objects by means of thermographic cameras. This recording registers thermal radiation, and in that an image is converted into the visible part of spectrum. This recording does not require any additional lighting, i.e. the objects invisible to a human eye can be recorded.

When a body heats to a certain temperature, it emits a thermal radiation in the form of electromagnetic waves. Solids and liquids emit a continuous spectrum of electromagnetic waves, and gases emit a discrete or line spectrum. Also, the bodies reflect and absorb the electromagnetic radiation which falls on them.

If a body, at a certain temperature on a given wavelength emits a radiation to a certain degree, the same radiation will be absorbed in the same conditions and to the same degree. If the body completely absorbs the radiation, then it presents the *absolutely black body*.

Let us define the *integral emission capacity* (E_T) which presents a *power flux density*, i.e. the energy emitted by a body heated to the temperature T in the time unit from the surface unit.

If only a small part is extracted from the power flux density, $dE_{\lambda,T}$ i.e. $dE_{\omega,T}$ which is emitted in the wavelength $d\lambda$, that is in the frequency range $d\omega$, we can write that $dE_{\lambda,T} = e_{\lambda,T}d\lambda$, or $dE_{\omega,T} = e_{\omega,T}d\omega$, where the unit $e_{\lambda,T}$, i.e. $e_{\omega,T}$ presents a *monochromatic emissivity* or the so-called *emission capacity*. It follows that:

$$E_T = \int_0^{\infty} e_{\omega,T} d\omega \quad (1)$$

On the basis of experiments and theoretic calculations in the second half of the 19th century, Stefan-Boltzmann law has been defined:

$$E_T = \sigma T^4 \quad (2)$$

where σ - is the *Stefan-Boltzmann constant* and T is *temperature*.

The experiments have shown that the relation of emissivity and absorptivity is equal and given by the universal Kirchoff function, i.e. $f(\omega, T) = (e_{\omega,T}) / (a_{\omega,T})$.

Because for the absolutely black body the absorptivity is

$a_{\omega,T} = 1$, it follows that for the absolutely black body monochromatic emissivity is equal to the universal Kirchoff function $f(\omega, T) = (e_{\omega,T})_{a.c.t}$. In calculations, it is more suitable to use the Kirchoff function dependant on frequency $f(\omega, T)$ while in experiments it is more suitable to use the function of wavelength $\varphi(\lambda, T)$. Figure 2 presents an example of experimental results of emissivity of the absolutely black body.

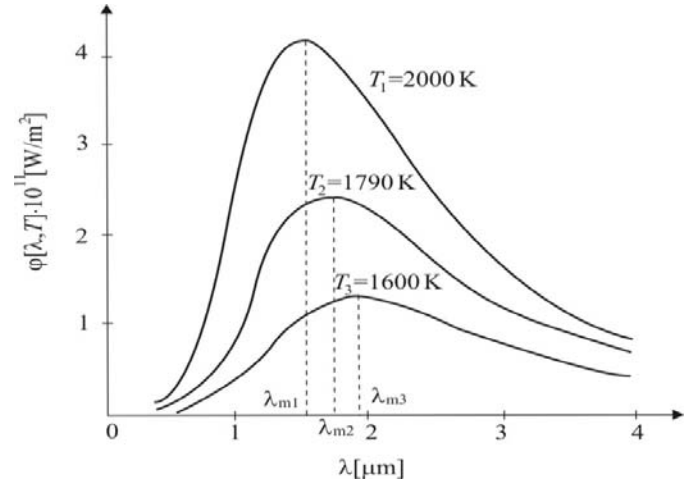


Figure 2. Dependence of emissivity on wavelength for different values of temperature.

Among the others, the results in Figure 2 show that with the increase of temperature the maximum of curves moves right, that is defined by the so-called Wien's law: $\lambda_m T = b$, where b is the constant, i.e. Wien's law can be given in the form:

$$\lambda_{\max} = \frac{2898}{T} [\mu m] \quad (3)$$

The explanation of the results in Figure 2, including Wien's law, by using the equation (1) stating that $f(\omega, T) = (e_{\omega,T})_{a.c.t}$ could not be given with the laws of classical physics. On the basis of laws of classical thermodynamics, Rayleigh and Jeans have come to the form of function

$$f(\omega, T) = \frac{\omega^2}{4\pi^2 c^2} kT. \quad (4)$$

The solution from (1) gives the result known as the ultraviolet catastrophe, because it is completely wrong in the ultraviolet part of the spectrum (Figure 3).

In 1900, Max Planck solved the problem with a new theory stating that electromagnetic waves are emitted in the form of electromagnetic quanta of energy, where the value of quantum energy is proportional to the frequency of radiation:

$$\varepsilon = h\nu = \hbar\omega \quad (5)$$

where \hbar is Planck constant. Planck obtained the function given by the expression:

$$f(\omega, T) = \frac{1}{4\pi^2 c^2} \frac{\hbar \omega^3}{e^{\frac{\hbar \omega}{kT}} - 1} \quad (6)$$

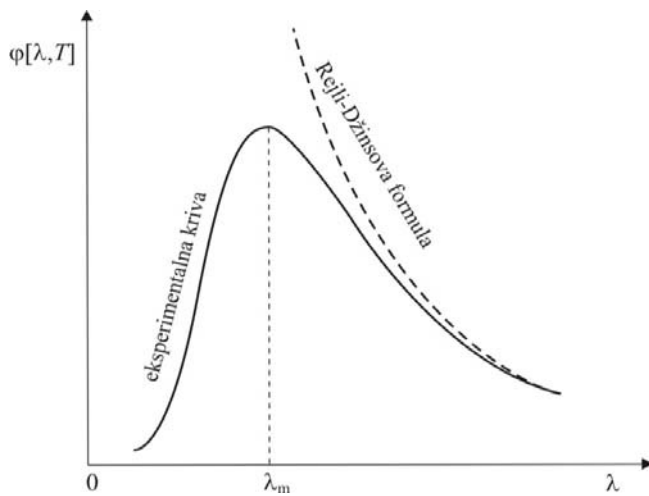


Figure 3. Experimental and Rayleigh-Jeans result

By including this function in the expression (1), solutions are obtained confirming the experimental results (2) and (3).

III. THERMOGRAPHY

A. Operation principle of thermography

Thermographic testing is based on contactless measurement of surface temperatures. The testing is based on the fact that an object which has a temperature above the temperature of absolute zero emits a thermal radiation of spectral band ($>0,7 \mu\text{m}$). The named radiation becomes visible for a human eye if the body reaches the temperature in the range from $500\div 550^\circ\text{C}$. Thermographic camera detects the radiations emitted by the heated object and presents it in the form of a thermogram. [2]

Thermographic testing can record the temperature distribution at the visible part of the tested object surface. For the testing results to be quality and offer a reliable information, the load of a facility must be bigger than 50% of nominal power. It is recommended to perform a thermographic testing in cloudy weather, because if the weather is sunny, a reflection may occur because of which the measurement is not useful. It should be taken into account not to neglect the influence of wind which can significantly cool down the place of a potential malfunction, the influence of dust and humidity which absorb the part of the infrared spectrum. [3], [4].

Thermographic testing is performed with the measurement method which is called the method of comparison. The method of comparison is based on the temperature comparison of elements with the same element of another phase under the same load. In a measurement, it is necessary to determine the place of referent temperature, environmental temperature, as well as the current for all three phases. The deviation of the measured temperature from the referent one indicates the malfunction of an object. The temperature excess is determined as the difference between the measured and referent temperature of the place

of temperature increase on the object. The attention should be paid to whether the place of operating temperature is of the same material as the place of temperature increase for the emissivity factor to be approximately equal. Thermographic testing is performed on the visible parts of tested elements. There are numerous advantages of using thermographic tests: [5]

- testing is performed during the plant operation,
- availability of the plant is increased,
- malfunction of equipment is located precisely in an early phase,
- unnecessary servicing is avoided,
- repair time is shortened,
- maintenance is improved,
- maintenance costs in the exploitation period are decreased,
- correct determination of control deadlines decreases the number of bigger malfunctions,
- number of plant outages is minimized,
- energy supply quality is increased and losses decreased.

B. Equipment for thermographic testing and thermogram processing

For the needs of electric power plants testing, the cameras of the producer FLIR have been used, models ThermoCAM PM 675 and E40.

Thermographic camera forms a thermal image by measuring the infrared radiation of a certain body or area part. The software, contained by the camera, performs the correction at the conversion of thermal image to an adequate thermogram, which presents the approximation of the exact temperature of the recorded object or the temperature distribution in the area.

The camera measurement range is from $-40\div 120^\circ\text{C}$ (range 1), from $80\div 500^\circ\text{C}$ (range 2). The camera accuracy is $\pm 2\%$ of reading. The permitted operating temperature of the environment is from $-15\div 50^\circ\text{C}$. The measurement is performed pursuant to the manufacturer's instruction. [6]

FLIR R&D Software 3.3. has been used for the analysis of the obtained thermograms, having the possibility to control the regime of recording the thermograms, setting of conditions regarding the temperature (min, max) of particular zones on a thermogram, warning of an user on the exceeding of set conditions and generating of reports for the selected thermogram. Figure 4 presents the operating environment of the application. [7]

IV. DISCONNECTORS AND THEIR MAINTENANCE

The basic task of disconnectors is a visible and contact separation of a part of a high voltage plant, which is in voltage condition, from the network. The ability to conduct a current in a primary cycle is crucial for the reliability of a high voltage disconnector, and that is violated with the appearance of "bad" connections, contacts and other primary cycle points in which a heating occurs increasing the probability that a damage of disconnector itself will occur together with the interruption of supply for consumers. The named defects are removed by periodic

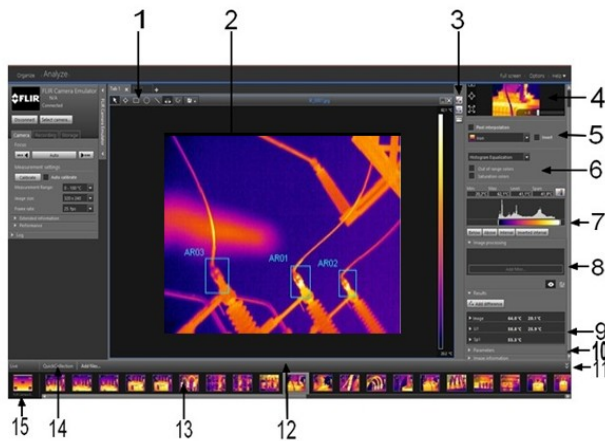


Figure 4. Operating environment of FLIR R&D Software 3.3.

1. *Measurement toolbar*: selection of points or areas for which a thermogram is analysed.
2. *Image window*: overview of a thermogram.
3. *Image Window*: selection of a thermogram, graphs and tables with measurement parameters.
- 4.-7. *Zoom, Controls, (Pixel interpolation, Color palette, Invert color palette), Image enhancements pane (Histogram equalization, Plateau equalization, Signal Linear, Temperature Linear, Digital Detail Enhancement), Scale pane*: options for setting a thermogram.
8. *Image processing pane*: selection of filters for processing
9. *Results pane*: overview results of all measurements
10. *Display parameters*: focus, calibration, measurement range...
- 11.-15. *Button, Recording toolbar, Recording snapshot location, Quick Collection pane, Live source control*: management of files.

diagnostic testing and regular maintenance [8]. At the service of a disconnector, it is necessary to disassemble both contact places of disconnectors, clear them properly and lubricate the bearings. The testing of the main current cycles includes the measurement of voltage drops at a disconnector, which must not be higher than the allowed ones. If the voltage drops are too high it is necessary to localize the place of malfunction by moving the current and voltage connectors and repair the places of bad connections.

V. ANALYSIS OF THERMOGRAPHIC TESTING

The testing was performed in the transformer substations which belong to the Field Unit (FU) Višegrad. These were TS 400/220/110/35/10 kV Višegrad, FU 110/35/20/10 kV Goražde 1, FU 110/20/10 kV Goražde 2, FU 110/35/10 kV Sokolac, FU 110/35/10 kV Rogatica and FU 110/35/10 kV Foča. The recordings were performed at the distance of 5m from the observed object, and the average emissivity was 0.95. The results present the cases where an increased heating of disconnectors and their belonging contacts occurs.

On the basis of the recording from 2014, the heating at the busbar disconnector F0 at the transmission line TL 110 kV Goražde 2 was noticed in the FU 110/35/20/10 kV Goražde 1. The thermogram of this disconnector is shown in Figure 5.

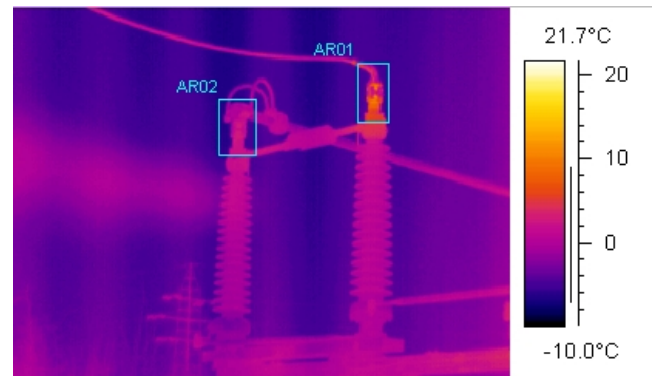


Figure 5. Thermogram of the busbar disconnector F0 in TL 110 kV Goražde 2 in the FU 110/35/20/10 kV Goražde 1

During the recording, the environmental temperature was -3°C , and the air humidity was 74% RH. The current per a phase was 100 A. The analysis showed the heating at the contact to the busbar (AR01 area in Figure 5). The temperature was 10.6°C . When it is compared to the environmental temperature and other (AR01, temperature 6°C), it can be concluded that the heating occurs at the contacts to the busbar and the repairing of the heating place is recommended. After thermographic recordings and noticed heating, the repairing of the heating place was performed. Before the repairing, the voltage drop of 204mV had been measured at the heating place, and after the performed repairing it was 10.25mΩ.

The next heating was noticed at the busbar disconnector in the transmission line TL 110 kV Goražde 2 was noticed in the FU 110/35/20/10 kV Goražde 1. At During the recording, the environmental temperature was -3°C , and the air humidity was 74% RH. The thermogram of this disconnector is shown in Figure 6.



Figure 6. Thermogram of the busbar disconnector F4 in TL 110 kV Goražde 2 in the FU 110/35/20/10 kV Goražde 1

During the recording, the current per a phase was 100 A. By a detailed analysis of thermogram, an increased heating can be noticed at the contacts to the busbar (AR01). The temperature of a contact was 31.2°C , while by the comparison to the contact on the other disconnector, where the temperature was 7°C , it can be concluded that an increased heating occurs at the contacts between disconnectors and busbars. During the repairing, the voltage drop of 316 mV had been measured at the heating place, while after the removal of the named defect the voltage drop at the contact was 11.35 mV.

During the testing in 2015, the heating on particular disconnectors was noticed in the FU 110/20/10 kV Goražde 2. The analysis of the thermogram showed the heating at the busbar disconnector F0 in the transmission line field transmission line (TL) 110 kV Višegrad. The thermogram of this disconnector is shown in Figure 7.

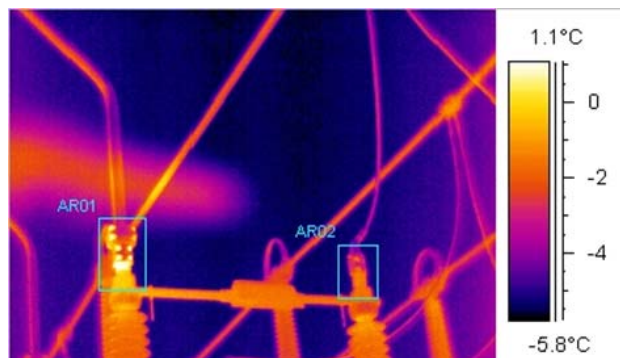


Figure 7. Disconnector F0 in TL 110 kV Višegrad in the FU 110/20/10 kV Goražde 2

During the recording, the environmental temperature was -4°C , and the air humidity was 66% RH. At this part of the facility, the current per phase was 103 A. On the basis of the analysis of the thermogram, it can be seen that there is an increased heating at the contact of the disconnector towards the switch (AR01). The temperature of the contact was 5.8°C . After the heating had been noticed, the repairing of the contact was performed. During that, a voltage drop of 98.8 mV had been measured at the contact. After the repairing (cleaning and tightening of connections), the voltage drop at the same place was 13.1 mV.

The heating at the busbar disconnectors F0 and F4 in the transmission line TL 110 kV Goražde 1 was noticed. The thermogram of this disconnector is shown in Figure 8.

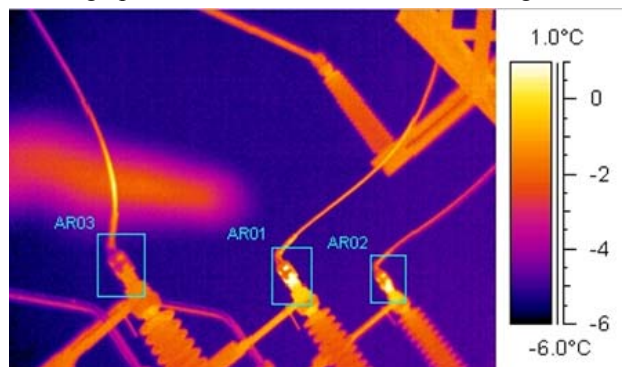


Figure 8. Thermogram of the disconnector F0 and F4 in TL 110 kV Goražde 1 in the FU 110/20/10 kV Goražde 2

During the recording in this part of the plant, the current per phase was 100 A. The thermogram showed the heating at the contacts of the disconnectors towards the busbar (AR01 and AR02). The temperature of the heated contacts was 1.6°C (AR01), 1.1°C (AR02). During the repairing of the contacts, a voltage drop of 87.5 mV (AR01) and 84.3 mV (AR02) had been measured. After the repairing (tightening of the connections), the voltage drop was 2.01 mV and 1.94 mV.

At the Figure 9 shown thermogram of the disconnector F8 in TL 110 kV Višegrad in the FU 110/10/35 Rogatica.

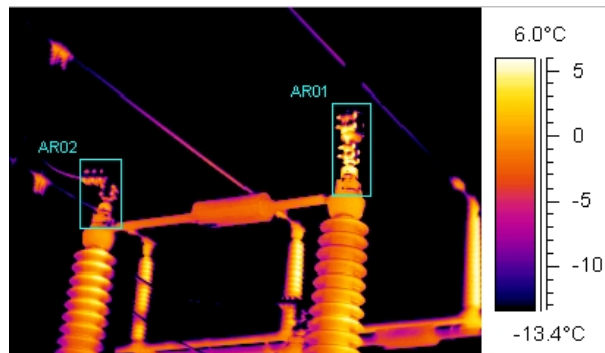


Figure 9. Thermogram of the disconnector F8 in TL 110 kV Višegrad in the FU 110/10/35 Rogatica

During the recording, the environmental temperature was -9°C , and the air humidity was 38% RH. The current per a phase was 85 A. The analysis showed the heating at the contact to the busbar (AR01 area in Figure 9). The temperature was 7.1°C . When it is compared to the environmental temperature and other (AR01, temperature 1.3°C), it can be concluded that the heating occurs at the contacts to the busbar and the repairing of the heating place is recommended. After thermographic recordings and noticed heating, the repairing of the heating place was performed. Before the repairing, the voltage drop of 256mV had been measured at the heating place, and after the performed repairing it was 2.51mΩ.

The heating at the busbar disconnector F0 in the the transformer field 1, 110 kV in the FU 110/10/35 kV Foča was noticed. The thermogram of this disconnector is shown in Figure 10.

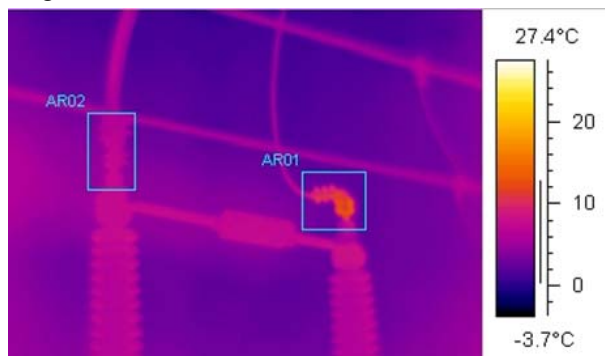


Figure 10. Thermogram of the disconnector F0 in the transformer field 1, 110 kV in the FU 110/10/35 kV Foča

During the recording, the environmental temperature was 5°C , and the air humidity was 75% RH. The current per a phase was 30 A. By the analysis of the thermogram at the contact of the disconnector towards the busbar, the temperature of 13.3°C was measured. If it is compared to the environmental temperature, it is concluded that an increased heating occurs at this contact and is recommended to repair the contact to prevent a bigger heating. At the repairing of the contact, the voltage drop of 127.8 mV had been measured. After the repairing (tightening of the contact) it was 2.14 mV.

VI. CONCLUSION

The application of thermograph as one of the methods in the monitoring of distribution facilities has an increasing

significance in the world. The advantage of this method is the fact that a facility is in the operating regime during the testing. By a detailed analysis of thermograms, the heating places can be noticed which may lead to serious damaging of elements in the facility. So, this analysis can locate precisely the elements, contacts which can cause interruptions and outages of the entire facility or its part and thus significantly decrease the availability and reliability. By a precise locating and identification of critical places, interventions can be done promptly and efficiently.

It is noticeable that the heating mostly occur at the contacts of the disconnecter, at the contacts of the disconnecter towards the switch and busbar, what is manifested by the heating of contacts to the temperatures which significantly deviate from the environmental temperature. The cause of this heating is a big transitional resistance of contacts which can be caused by the oxidation of contacts or bad connections.

To decrease the phenomena, it is necessary to perform regularly the preventive thermographic control (minimally once a year), so that the points in which the temperature increased, possibly leading to the damaging of elements or the entire facility, which may cause a significant material

and financial damage both for the producer and the consumer, can be noticed in time.

LITERATURE

- [1] Davor Bajs, "Metoda i kriteriji u revitalizaciji elektroenergetske prijenosne mreže", Sveučilište u Splitu, Fakultet Elektrotehnike, strojarstva i brodogradnje, Split 2007.
- [2] Žarko Barbarić, "Termovizija formiranje i primena termovizijske slike", Akademska Misao, Beograd 2014.
- [3] Mileta Žarković, Dr Zlatan Stojković, „Automatizacija termovizijskog postupka u monitoringu i dijagnostici elemenata prenosne mreže“ Infoteh- Jahorina, mart 2012.
- [4] Igor Kuzle, Dijagnostika u održavanju elemenata elektroenergetskog sustava, Sveučilište u Zagrebu, Fakultet elektrotehnike i računarstva, Zagreb 2013.
- [5] Predrag Šaraba, Božidar Popović, Dražan Kršmanović, „Preventivno termovizijsko snimanje elektroenergetskih postrojenja metodom IR termografije“, Infoteh- Jahorina, mart 2015.
- [6] Therma CAM PM 675 Operator's manual", Decembar 2000 – Publ. No. 1 557 455 – Rev. A.
- [7] FLIR, User's manual Flir R&D Software 3.3.
- [8] P. Šaraba, B. Popović, D. Kršmanović, "Preventivno termovizijsko snimanje VN rastavljača", Crnogorski komitet međunarodnog vijeća za velike električne mreže –CIGRE 2015.

Design of Ternary Content-Addressable Memories with Dynamically Power-gated Storage Cells Using FinFETs

Meng-Chou Chang, Kai-Lun He, and Yu-Chieh Wang

Abstract—An independent-gate FinFET can operate in two modes: SG (shorted-gate) and IG (independent-gate) modes, and thus a FinFET-based circuit offers rich design options for lower power, better performance or reduced transistor count. In this paper, we present two novel dynamically power-gated FinFET TCAM cells, called DPG-17T and DPG-16T, which power-gate the prefix data storage unit when storing a ‘don’t care’ value. With the dynamic power-gating mechanism, DPG-17T/DPG-16T achieve lower power dissipation by eliminating the switching power of the comparison FinFETs and suppressing the leakage power of the prefix data storage when storing a ‘don’t care’ value. Moreover, the discharge path of the matchline in DPG-17T/DPG-16T can be constructed with only one FinFET instead of two FinFETs, greatly boosting the search speed. Simulation results have shown that a TCAM of 64-word×128-bit using DPG-17T/DPG-16T can reduce the worst-case search delay by 53.0%/53.6% and improve the energy-delay product by 68.5%/70.4% when operating under a search rate of 4.0 GHz.

Index Terms—Ternary content-addressable memories (TCAM), FinFET, power gating, low-power electronics.

Original Research Paper
DOI: 10.7251/ELS1620009C

I. INTRODUCTION

FINFET (fin-type field-effect transistor) has emerged as one of the best substitutes for planar MOSFET technology to enable further CMOS scaling. As shown in Fig. 1, the FinFET device structure consists of a thin fin-shaped silicon body surrounded by shorted or independent gates on either side of the

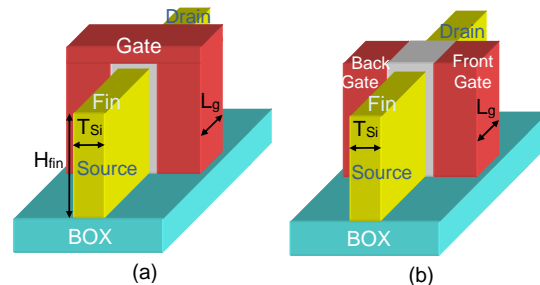


Fig. 1. FinFET device structures. (a) Shorted-gate FinFET. (b) Independent-gate FinFET.

fin, constructed on SOI (silicon-on-insulator) [1]–[3] or bulk substrates [4], [5]. The FinFET device offers the following advantages [6]: 1) As the fin silicon body is generally thin enough with the thickness of the fin, denoted by T_{si} , smaller than the channel length, denoted by L_g , the gate electrode of the FinFET device has superior control over the channel, thereby suppressing the short-channel effects and leading to reduced subthreshold leakage, steeper subthreshold swing, and a higher I_{on}/I_{off} ratio; 2) As the thin silicon body of the FinFET device is typically undoped or lightly doped, the carrier mobility is thus enhanced with ionized dopant scattering eliminated, and the device variations due to random dopant fluctuation (RDF) are reduced.

As illustrated in Fig. 1, a FinFET device can be constructed as a shorted-gate FinFET (Fig. 1(a)) or as an independent-gate FinFET (Fig. 1(b)). In the shorted-gate FinFET, the gate controls the channel from both sides and the top of the thin silicon body, leading to increased process transconductance. In the independent-gate FinFET, the top part of the gate is etched away, resulting in two independent gates, the front gate and the back gate. The front gate and back gate of an independent-gate FinFET can be separately controlled by two independent signals, and thus an independent-gate FinFET can be used as a pair of parallel planar MOSFETs controlled by two independent signals.

Manuscript received 4 September 2015. Accepted for publication 25 December 2015.

Meng-Chou Chang is with Department of Electric Engineering, National Changhua University of Education, Taiwan (e-mail: mchang@cc.ncue.edu.tw).

Kai-Lun He is with Department of Electric Engineering, National Changhua University of Education, Taiwan.

Yu-Chieh Wang is with Department of Electric Engineering, National Changhua University of Education, Taiwan.

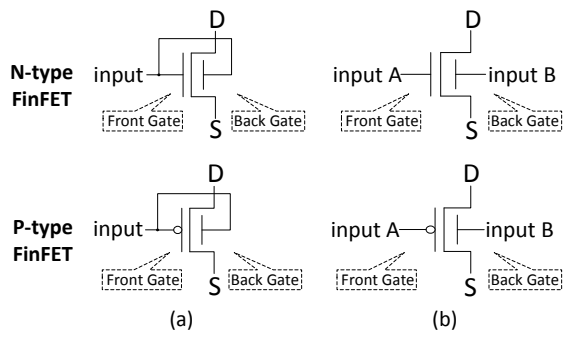


Fig. 2. Two operating modes of a FinFET. (a) Shorted-gate (SG) mode. (b) Independent-gate (IG) mode.

As illustrated in Fig. 2, a FinFET can operate in two modes: shorted-gate (SG) and independent-gate (IG) modes. In the SG mode, the front gate and the back gate of the FinFET are tied together and controlled by a single input signal (see Fig. 2(a)). A SG-mode FinFET has the advantage of providing the maximum drive strength when it is turned on. In the IG mode (see Fig. 2(b)), the front gate and the back gate of the FinFET are separately controlled. An IG-mode FinFET can be employed to replace a pair of parallel planar MOSFETs. As a FinFET device can operate in two modes: SG and IG modes, a FinFET-based circuit offers rich design options for lower power dissipation or reduced transistor count. Many innovative FinFET-based circuit styles have been proposed in the literature [7]-[13]. In [7], a single independent-gate FinFET is used to replace a pair of parallel transistors in the pull-up or pull-down networks of logic gates to obtain a compact low-power implementation of the same Boolean function. In [8], the authors explored the performance and power characteristics of FinFET-based NAND gates configured in various modes, including the SG, IG, LP (low-power) modes and a hybrid IG/LP mode. In [9], the authors investigated the design space of elementary logic gates, latches, and flip-flops in FinFET technology for optimal tradeoffs in leakage versus delay. In [10], the authors explored the possibility of using a single dual- V_{th} independent-gate FinFET to replace series transistors in the pull-up or pull-down networks of logic gates. Particularly, many published works are devoted to the design of FinFET-based SRAM cells [11]-[13].

A content-addressable memory (CAM) is a special type of memory that compares the input search word with all data words stored in the memory simultaneously and then returns the address of the matching data word. CAMs facilitate high-speed lookup operation and have been employed in numerous applications, such as data compression [14], image coding [15], Hough transform [16], and associative caches [17]. CAM is classified into two types: binary CAM (BCAM) and ternary CAM (TCAM). A BCAM cell stores either a logic '0' or a logic '1' while a TCAM cell can store an additional state, 'don't care' (denoted by 'x'), for supporting wildcard matching. Owing to this partial-match feature, TCAMs can be used to implement the routing tables in network routers for accelerating IP packet classification and forwarding [18]. However, CAMs consume substantial dynamic and static power due to their

parallel search operation and large memory array. Various low-power techniques have been developed to reduce the dynamic power dissipation of CAMs [19]-[22]. These techniques include low-swing schemes [19], current-racing schemes [20], current-saving schemes [21], pipelining schemes [22], and so on. Particularly, in [23], the dynamic power source (DPS) scheme was proposed to suppress the leakage power dissipation of TCAM. The key idea behind the DPS scheme is that the prefix storage unit in an asymmetric TCAM cell with 'x' state can be power-gated to suppress leakage dissipation since the prefix data associated with an 'x' bit is useless for determining the match result.

In this paper, we propose two novel dynamically power-gated FinFET TCAM cells, called DPG-17T and DPG-16T, which power-gate the prefix data storage unit when storing a 'don't care' value. With the dynamic power-gating mechanism, DPG-17T/DPG-16T can achieve lower power dissipation by eliminating the switching power of the comparison FinFETs and suppressing the leakage power of the prefix data storage when storing a 'don't care' value.

The remainder of this paper is organized as follows. In Section II, we present the operation of the asymmetric TCAM cell and introduce a FinFET TCAM cell, called Base-16T, which is used as a basis for comparison with the proposed dynamically power-gated FinFET TCAM cells. In Section III, we present the proposed dynamically power-gated FinFET TCAM cells, DPG-17T and DPG-16T. Section IV presents the simulation results which are obtained from HSPICE simulations using the PTM (Predictive Technology Model) 32-nm FinFET models [24]. Section V concludes this paper.

II. BACKGROUND

A. Traditional Asymmetric TCAM Cells

Fig. 3 shows the block diagram of a typical TCAM, consisting of an array of TCAM cells, a search data register, and a column of sense amplifiers.

Each row of the TCAM cell array stores one data word

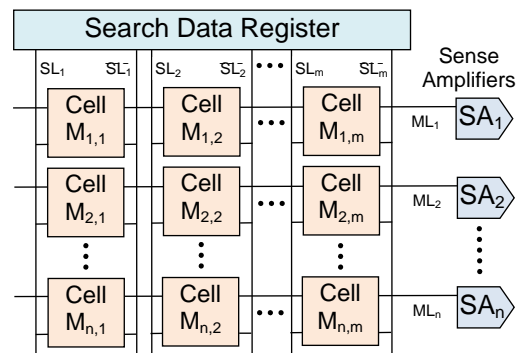


Fig. 3. Block diagram of a typical TCAM with a size of n -word $\times m$ -bit.

together with the associated mask word, and has one associated matchline (ML), which is used to indicate whether the stored data word on this row matches or mismatches the search data word. Each column of the TCAM cell array has a

pair of searchlines, SL and \overline{SL} , which are used to broadcast the associated search data bit and its complement to all TCAM cells in this column.

Before the search operation begins, all matchlines are precharged to HIGH, and all searchlines are discharged to LOW. The search operation begins by loading the search data word into the search data register and enabling the searchline drivers to broadcast the search data word to the TCAM cell array via searchlines. Then, each TCAM cell compares its stored data bit with the search bit on the corresponding searchlines, and the result of comparison, match or mismatch, affects whether the associated matchline should be discharged.

In a NOR-matchline TCAM, all the TCAM cells belonging to the same row are connected in parallel, and any single-bit mismatch on this row will create a conducting path from the associated matchline to ground, causing the associated matchline to discharge. That is, in a NOR-matchline TCAM, after the search process, a matchline remaining precharged indicates a match condition (i.e., the associated stored data word matches the search data word), and a discharged matchline indicates a mismatch condition (i.e., the associated stored data word mismatches the search data word).

A TCAM cell provides two basic functions: bit storage and bit comparison. The structure of the asymmetric TCAM cell is shown in Fig. 4. An asymmetric TCAM cell consists of four subunits: the prefix data storage, the mask storage, the XOR unit, and the matchline control unit.

The prefix data storage stores the associated data bit, D , together with its complement, \overline{D} ; the mask storage stores the

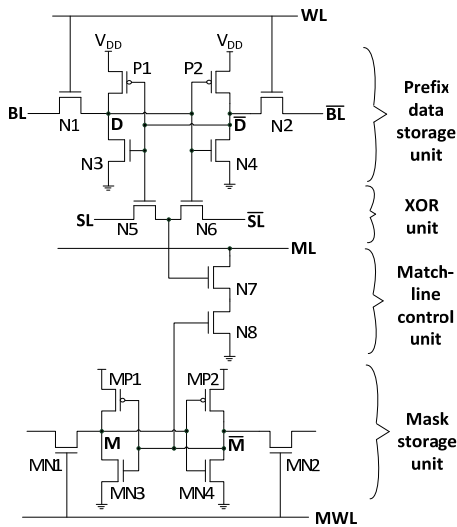


Fig. 4. The structure of the asymmetric TCAM cell.

associated mask bit, M , together with its complement, \overline{M} . A TCAM cell can store a ternary value ('0', '1', and 'x'): if the TCAM cell stores a logic '1', $D=1$ and $M=0$; if the TCAM cell stores a logic '0', $D=0$ and $M=0$; if the TCAM cell stores an 'x', $M=1$ and D can be either 0 or 1.

The XOR unit is used to compare the stored data bit, D/\overline{D} , with the associated search data bit, SL/\overline{SL} , on the searchline. If the stored data bit mismatches the search data bit, the gate of

NMOS $N7$ is set to HIGH, and thus $N7$ is turned on; otherwise, the gate of NMOS $N7$ is set to LOW, and $N7$ is turned off.

The matchline-control unit, comprised of transistors $N7$ and $N8$, controls whether the precharged matchline (ML) should be discharged. If the mask bit M/\overline{M} is 0/1 (i.e., the stored data bit is not an 'x'), transistor $N8$ is turned on, and the matchline-control unit creates a conducting pull-down path from the matchline ML to ground if $N7$ is also turned on (i.e., the stored data bit mismatches the search data bit). On the contrary, if the mask bit M/\overline{M} is 1/0 (i.e., the stored data bit is an 'x'), transistor $N8$ is turned off, cutting off the discharge path (comprised of $N7$ and $N8$) from the matchline, which is consistent with the fact that a stored 'x' bit always matches the search data bit no matter whether the search data bit is 0 or 1.

B. The Base FinFET TCAM cell

As stated earlier, a FinFET can operate in two modes: SG and IG modes (Fig. 2). In the SG mode, the front gate and the back gate of the FinFET are tied together and controlled by a single input signal. A SG-mode FinFET has the advantage of providing the maximum drive strength when it is turned on. In the IG mode, the front gate and the back gate of the FinFET are separately controlled. Thus, an IG-mode FinFET can be employed to replace a pair of parallel planar MOSFETs.

In our previous work [25], we have explored the optimal configuration for the asymmetric FinFET-based TCAM cell. By varying the operating mode (SG/IG) for every FinFET in the TCAM cell, and measuring the resultant performance for various combinations of operating modes, we have acquired the best FinFET TCAM cell configuration, called Base-16T and depicted in Fig. 5(a), in terms of minimum energy-delay product. In Base-16T, FinFETs $N5$ and $N6$ are assigned SG mode to accelerate the XOR operation; FinFETs $N7$ and $N8$ are also assigned SG mode because they are on the matchline discharge path and play a critical role in determining the worst-case search delay of the TCAM; the other FinFETs, which are not critical in determining the worst-case search delay, are assigned the IG mode to reduce the leakage powerdissipation of the TCAM.

In the following sections, Base-16T will be used as the base FinFET TCAM cell for performance comparison with the proposed dynamically power-gated FinFET TCAM cells.

III. DYNAMICALLY POWER-GATED FINFET TCAM CELLS

A TCAM cell can store a ternary value: '0', '1', or 'x'. If an asymmetric TCAM cell stores an 'x' (i.e., $M/\overline{M}=1/0$), the stored data bit, D/\overline{D} , is meaningless and useless for determining the final match result during a search operation. Hence, the prefix data storage unit in a TCAM cell storing an 'x' can be dynamically power-gated to suppress the power dissipation of the TCAM cell without impeding the normal search operation of the TCAM. In this work, we propose two novel dynamically power-gated FinFET TCAM cells, called DPG-17T (Fig. 6(a)) and DPG-16T (Fig. 7(a)), which power-gate the prefix data storage unit when storing an 'x' in order to suppress the leakage power dissipation of the TCAM.

In order to assess and compare the performance of three types of FinFET TCAM cells - including Base-16T, DPG-17T, and DPG-16T - we have implemented a NOR-matchline TCAM with a size of 64-word \times 128-bit for each type of FinFET TCAM

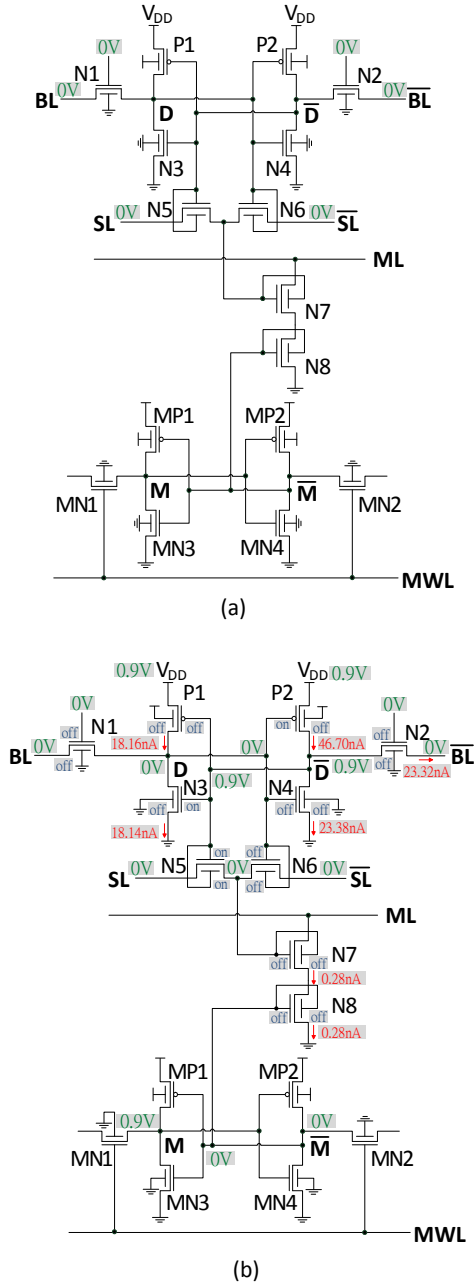


Fig 5. (a) The base FinFET TCAM cell – Base-16T. (b) Base-16T with node voltages and I_{sub} labeled for $D = 0$, $M = 1$ and $SL/SL = 0/0$.

cells, and have performed the associated HSPICE simulations using the PTM (Predictive Technology Model) 32-nm FinFET models [24] at the typical PVT case (i.e., TT process corner, 25 °C, $V_{DD} = 0.9$ V). In our simulations, all FinFETs in the TCAM cells are sized minimum with fin height $H_{fin} = 32$ nm, fin thickness $T_{si} = 16$ nm, and channel length $L_g = 32$ nm. Table I shows the subthreshold leakage current (I_{sub}) and the leakage power (P_{leak}) for each FinFET in the three types of FinFET

TABLE I. SUBTHRESHOLD LEAKAGE CURRENT (I_{sub}) AND LEAKAGE POWER (P_{leak}) FOR EACH FINFET IN THREE TYPES OF FINFET TCAM CELLS.

FinFET	Base FinFET TCAM cell Base-16T		FinFET TCAM cell DPG-17T		FinFET TCAM cell DPG-16T	
	I_{sub} (nA)	P_{leak} (nW)	I_{sub} (nA)	P_{leak} (nW)	I_{sub} (nA)	P_{leak} (nW)
P1	18.16	16.35	6.67	1.10	0.00	0.00
P2	46.70	0.00	6.67	1.10	0.00	0.00
P3	-	-	13.34	9.81	-	-
N1	0.00	0.00	0.00	0.00	0.00	0.00
N2	23.32	20.99	0.00	0.00	0.00	0.00
N3	18.14	0.00	6.67	0.00	0.00	0.00
N4	23.38	21.04	6.67	0.00	0.00	0.00
N5	0.00	0.00	0.00	0.00	0.00	0.00
N6	0.00	0.00	0.00	0.00	0.00	0.00
N7	0.28	0.01	0.66	0.02	0.66	0.02
N8	0.28	0.00	0.00	0.00	0.00	0.00
MP1	46.70	0.00	46.70	0.00	46.72	0.00
MP2	18.15	16.34	18.15	16.34	18.15	16.34
MN1	23.32	20.99	23.32	20.99	23.32	20.99
MN2	0.00	0.00	0.00	0.00	0.00	0.00
MN3	23.39	21.05	23.39	21.05	23.39	21.05
MN4	18.14	0.00	18.14	0.00	18.14	0.00
Total P_{leak}	-	116.76	-	70.41	-	58.40

TCAM cells when the TCAM cell stores an 'x' and is idle (i.e., not in the process of a search operation).

Let us first consider Base-16T (see Fig. 5(b)) and assume that the stored data bit D/\bar{D} is 0/1 (i.e., the voltage level of node D/\bar{D} is 0 V/0.9 V) and the TCAM is not performing a search operation (i.e., the TCAM is idle and SL/\bar{SL} is 0 V/0 V). As given in Table I and Fig. 5(b), even though FinFETs P1, N2, and N4 in Base-16T are turned off, there still exist significant subthreshold leakage currents flowing through those FinFETs due to a large voltage drop of 0.9 V across the drain and source of those FinFETs (i.e., P1, N2, and N4). From Table I, Base-16T has a static power dissipation of 116.76 nW when storing an 'x' and being idle.

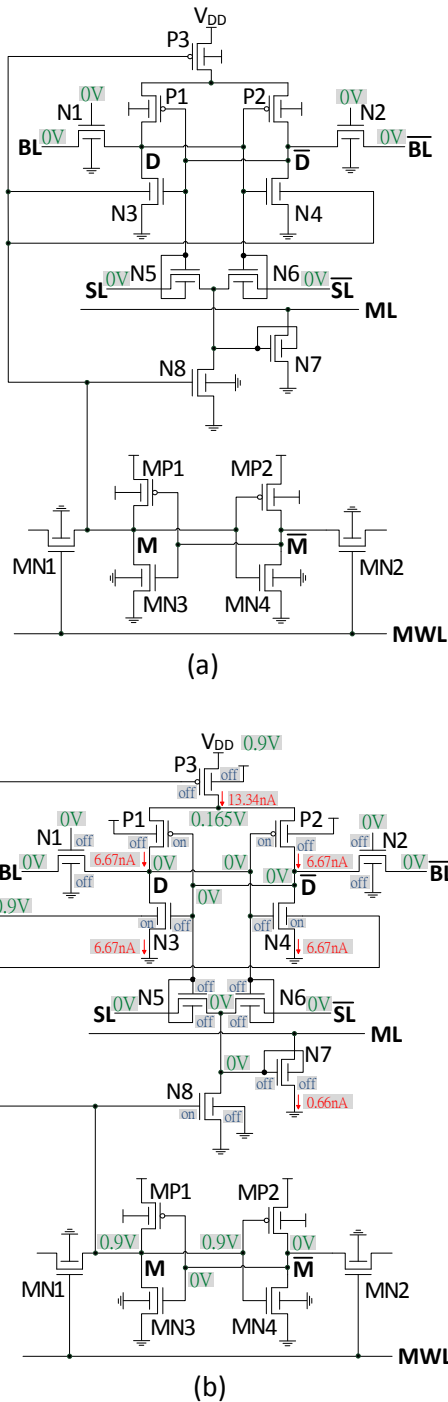


Fig 6. (a) The proposed dynamically power-gated FinFET TCAM cell DPG-17T. (b) DPG-17T with node voltages and I_{sub} labeled for $M = 1$ and $SL/SL = 0/0$.

The first proposed dynamically power-gated FinFET TCAM cell DPG-17T is shown in Fig. 6 (a). The differences between DPG-17T and Base-16T include: 1) DPG-17T has an additional sleep FinFET P3, 2) the operating mode of both N3 and N4 in DPG-17T is changed from SG mode to IG mode with the back gates of both N3 and N4 connected to the mask data bit (node M), and 3) the discharge path of the matchline in DPG-17T is comprised of only one FinFET N7 instead of two FinFETs,

leading to a much smaller worst-case search delay. Noted that FinFET N8 is not located on the discharge path of the matchline, and its purpose is just to set the gate voltage of N7 to 0 V when the TCAM cell stores an 'x'.

Let us consider DPG-17T (see Fig. 6(b)) and assume that DPG-17T stores an 'x' (i.e., the voltage level of node M/M-bar is 0.9 V/0 V) and the TCAM is not performing a search operation (i.e., the TCAM is idle and SL/SL-bar is 0 V/0 V). As given in Fig. 6(b), P3 is turned off, causing the voltage level of the drain of P3 to converge to 0.165 V, and the back gates of both N3 and N4 are turned on, causing the voltage level of nodes D and D-bar to become 0 V. As given in Table I, compared with the case of Base-16T, the subthreshold leakage currents flowing through P1, N2, and N4 in DPG-17T are greatly reduced because the voltage drop across those FinFETs is very small (see Fig. 6(b)). Overall, a TCAM cell using DPG-17T instead of Base-16T can reduce the leakage power dissipation by 40% when storing an 'x'.

Note that a DPG-17T TCAM cell storing an 'x' does not impede the normal search operation of the TCAM. Suppose that the TCAM wants to perform a search operation now. The search data register begins to drive values on the searchlines, and SL/SL-bar in Fig. 6(b) will become either 0.9 V/0 V (if the associated search data bit is '1') or 0 V/0.9 V (if the associated search data bit is '0'). In either case, FinFETs N5, N6, and N7 in Fig. 6(b) stay turned off, and thus the TCAM cell storing an 'x' will not create a discharge path for the associated matchline. That is, whether the associated matchline will eventually discharge is determined by other TCAM cells with $M = 0$.

The second proposed dynamically power-gated FinFET TCAM cell DPG-16T is shown in Fig. 7 (a).

In contrast to DGP-17T, which needs an additional sleep FinFET P3 to fulfill power gating, DPG-16T needs no sleep FinFET and accomplishes power gating by connecting node M directly to the sources of both FinFETs P1 and P2.

Let us consider DPG-16T (see Fig. 7(b)) and assume that DPG-16T stores an 'x' (i.e., the voltage level of node M/M-bar is 0.9 V/0 V) and the TCAM is not performing a search operation (i.e., the TCAM is idle and SL/SL-bar is 0 V/0 V). As given in Fig. 7(b), the sources of both FinFETs P1 and P2 are connected to 0 V, and the back gates of both N3 and N4 are turned on, causing the voltage level of nodes D and D-bar to become 0 V. As given in Table I, the subthreshold leakage currents flowing through P1, P2, N1, N2, N3, N4, N5, N6, and N8 in DPG-16T all become 0. Overall, a TCAM cell using DPG-16T instead of Base-16T can reduce the leakage power dissipation by 50% when storing an 'x'.

As in the case of DPG-17T, a DPG-16T TCAM cell storing an 'x' does not impede the normal search operation of the TCAM.

IV. SIMULATION RESULTS

Table II gives static power consumption comparison of a TCAM of 64-word \times 128-bit implemented with three types FinFET TCAM cells - including Base-16T, DPG-17T, and DPG-16T. As the percentage of 'x' bits in the TCAM cell array

has an influence on TCAM power consumption, during our HSPICE simulation, we have set the prefix length distributions of the TCAM simulated close to those of ‘AS2.0 IPv6 BGP (Border Gateway Protocol) table data’ given in [26]. Since

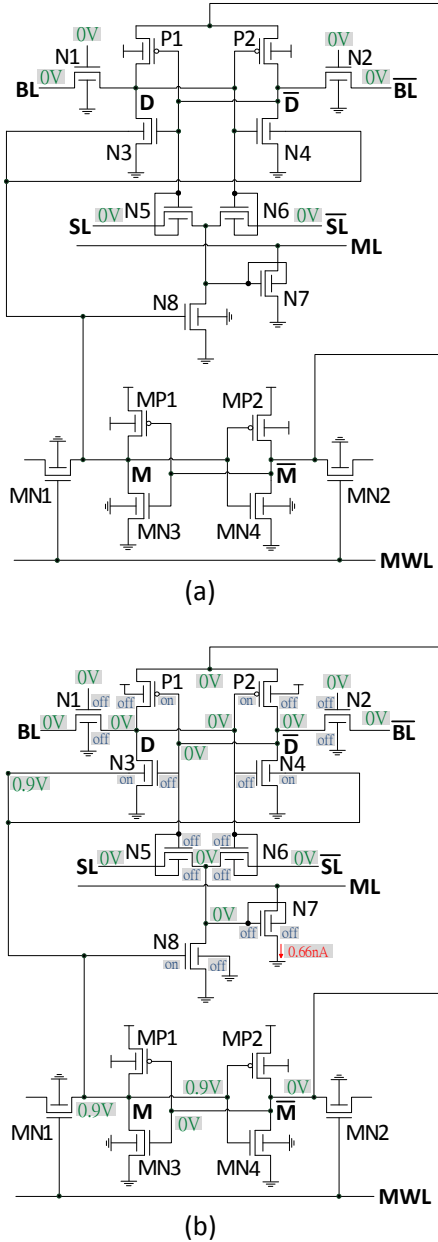


Fig 7. (a) The proposed dynamically power-gated FinFET TCAM cell DPG-16T. (b) DPG-16T with node voltages and I_{sub} labeled for $M = 1$ and $SL/SL = 0/0$.

68.5% of the prefix data bits in the AS2.0 IPv6 BGP table are ‘x’, the same percentage (i.e., 68.5%) of the prefix data bits in the TCAM simulated are set as ‘x’. From Table II, a TCAM employing DPG-17T/DPG-16T, instead of Base-16T, can reduce the static power dissipation by 27.2%/34.2%.

TABLE II. STATIC POWER CONSUMPTION COMPARISON OF A TCAM OF 64-WORD \times 128-BIT IMPLEMENTED WITH THREE TYPES OF FINFET TCAM CELLS.

	Type of the FinFET TCAM cells used in the TCAM		
	Base-16T	DPG-17T	DPG-16T
Static power consumption of the whole TCAM (μ W)	961.3	700.2	632.9

Table III gives performance comparison of three FinFET TCAM cells - including Base-16T, DPG-17T, and DPG-16T - used to implement a TCAM of 64-word \times 128-bit operating at a search rate of 4.0 GHz. As given in Table III, the use of DPG-17T/DPG-16T, instead of Base-16T, can reduce the TCAM power dissipation by 32.9%/36.3%. The lower power dissipation of DPG-17T/DPG-16T comes from 1) A TCAM cell storing an ‘x’ always turns off FinFETs N5 and N6, eliminating the switching power of N5 and N6 during comparison, and 2) The prefix data storage unit of a TCAM cell storing an ‘x’ is power-gated during the search process, consuming only little leakage power. Moreover, since the discharge path of the matchline in DPG-17T/DPG-16T is comprised of only one FinFET rather than two FinFETs as in Base-16T, the worst-case search delay of a TCAM employing DPG-17T/DPG-16T can be greatly reduced. As given in Table III, the use of DPG-17T/DPG-16T, instead of Base-16T, can reduce the worst-case search delay by 53.0%/53.6%, and improve the energy-delay product by 68.5%/70.4%.

TABLE III. PERFORMANCE COMPARISON OF THREE FINFET TCAM CELLS USED TO IMPLEMENT A TCAM OF 64-WORD \times 128-BIT OPERATING AT A SEARCH RATE OF 4.0 GHz

	Type of the FinFET TCAM cells used in the TCAM		
	Base-16T	DPG-17T	DPG-16T
Average power for whole TCAM (mW) [A]	2.95	1.98	1.88
Worst-case search delay (ps) [B]	71.25	33.48	33.07
Search energy for whole TCAM (fJ) [C=A \cdot 0.25ns]	736.90	495.15	469.73
Search energy per bit (aJ) [D=C/64/128]	89.95	60.44	57.34
Energy-delay product (10^{-27} J \cdot s) [E=B \cdot D]	6.41	2.02	1.90

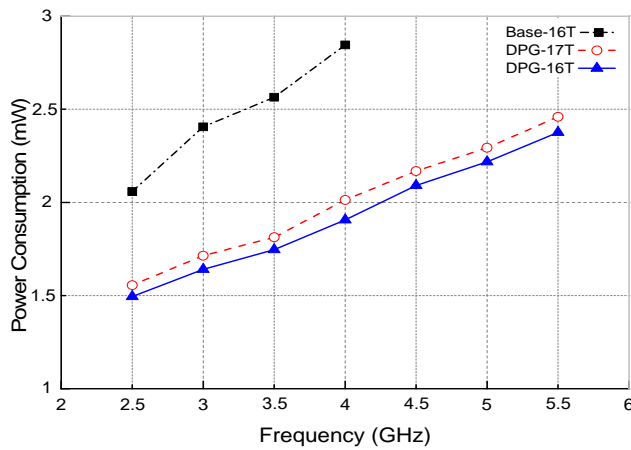


Fig. 8. Power consumption comparison of a TCAM of 64-word \times 128-bit implemented with three types of FinFET TCAM cells.

Fig. 8 gives power consumption comparison of a TCAM of 64-word \times 128-bit implemented with three types of FinFET TCAM cells, for various search rates. The maximum search rate for the TCAM implemented with Base-16T/DPG-17T/DPG-16T is 4.0/5.5/5.5 GHz. Note that a TCAM with DPG-17T/DPG-16T operating at a higher frequency of 5.5 GHz even consumes less power than a TCAM with Base-16T operating at a lower frequency of 3.5 GHz.

V. CONCLUSION

In this paper, we have proposed two dynamically power-gated FinFET TCAM cells, DPG-17T and DPG-16T. When operating under a search rate of 4.0 GHz, a TCAM of 64-word \times 128-bit using DPG-17T/DPG-16T instead of Base-16T can 1) reduce the power dissipation by 32.9%/36.3%, 2) reduce the worst-case search delay by 53.0%/53.6%, and 3) improve the energy-delay product by 68.5%/70.4%.

The advantages of the dynamically power-gated TCAM cells, DPG-17T and DPG-16T, are summarized as follows: 1) The discharge path of the matchline in DPG-17T/DPG-16T is comprised of only one FinFET instead of two, greatly reducing the worst-case search delay, 2) A TCAM cell storing an 'x' always turns off FinFETs N5 and N6, eliminating the switching power of N5 and N6 during comparison, and 3) The prefix data storage unit of a TCAM cell storing an 'x' is power-gated during the search process, suppressing leakage power dissipation.

REFERENCES

- [1] Y. Bin, C. Leland, S. Ahmed, W. Haihong, S. Bell, Y. Chih-Yuh, C. Tabery, H. Chau, X. Qi, K. Tsu-Jae, J. Bokor, H. Chenming, L. Ming-Ren, and D. Kyser, "FinFET scaling to 10 nm gate length," *IEDM Tech. Digest*, pp. 251-254, 2002.
- [2] A. Bansal, S. Mukhopadhyay, and K. Roy, "Device-optimization technique for robust and low-power FinFET SRAM design in nanoscale era," *IEEE Trans. Electron Devices*, vol. 54, pp. 1409-1419, Jun 2007.
- [3] K. Akarvardar, C.D. Young, M.O. Baykan, I. Ok, T. Ngai, K.-W. Ang, M.P. Rodgers, S. Gausepohl, P. Majhi, C. Hobbs, P.D. Kirsch, and R. Jammy, "Impact of Fin Doping and Gate Stack on FinFET (110) and (100) Electron and Hole Mobilities," *IEEE Electron Device Letters*, vol. 33, no. 3, pp. 351-353, Mar. 2012.
- [4] T.-S. Park, S. Choi, D.-H. Lee, U.-I. Chung, J. T. Moon, E. Yoon, and J.H. Lee, "Body-tied triple-gate NMOSFET fabrication using bulk Si wafer," *Solid-State Electronics*, vol. 49, pp. 377-383, Mar 2005.
- [5] T.-H. Hsu, T. Lue, Y.-C. King, J.-Y. Hsieh, E.-K. Lai, and K.-Y. Hsieh, "A high-performance body-tied FinFET bandgap engineered SONOS (BE-SONOS) for NAND-type flash memory," *IEEE Electron Device Letters*, vol. 28, pp. 443-445, May 2007.
- [6] C. Hu, "Thin-body FinFET as scalable low voltage transistor," in *Proc. Int. Symp. VLSI Technol. Syst. Appl.*, 2012, pp. 1-4.
- [7] A. Datta, A. Goel, R. T. Cakici, H. Mahmoodi, D. Lekshmanan, and K. Roy, "Modeling and circuit synthesis for independently controlled double gate FinFET devices," *IEEE Trans. Comput.-Aided Design of Integr. Circuits Syst.*, vol. 26, no. 11, pp. 1957-1966, Nov. 2007.
- [8] A. Muttreja, N. Agarwal, and N. K. Jha, "CMOS logic design with independent-gate FinFETs," in *Proc. Int. Conf. Comput. Design*, 2007, pp. 560-567.
- [9] A. N. Bhoj and N. K. Jha, "Design of logic gates and flip-flops in high-performance FinFET technology," *IEEE Trans. Very Large Scale Integr. (VLSI) Syst.*, vol. 21, no. 11, pp. 1975-1988, Nov. 2013.
- [10] M. Rostami and K. Mohanram, "Dual- V_{th} independent-gate FinFETs for low power logic circuits," *IEEE Trans. Comput.-Aided Design of Integr. Circuits Syst.*, vol. 30, no. 3, pp. 337-349, Mar. 2011.
- [11] S. A. Tawfik, Z. Liu, and V. Kursun, "Independent-gate and tied-gate FinFET SRAM circuits: Design guidelines for reduced area and enhanced stability," in *Proc. Int. Conf. Microelectronics*, 2007, pp. 171-174.
- [12] C.-Y. Hsieh, M.-L. Fan, V. P.-H. Hu, P. Su, and C.-T. Chuang, "Independently-controlled-gate FinFET Schmitt trigger sub-threshold SRAMs," *IEEE Trans. Very Large Scale Integr. (VLSI) Syst.*, vol. 20, no. 7, pp. 1201-1210, Jul. 2012.
- [13] A. B. Sachid and C. Hu, "Denser and more stable SRAM using FinFETs with multiple fin heights," *IEEE Trans. Electron Devices*, vol. 59, no. 8, pp. 2037-2041, Aug. 2012.
- [14] R.-Y. Yang and C.-Y. Lee, "High-throughput data compressor designs using content addressable memory," in *Proc. IEEE Int. Symp. Circuits Syst. (ISCAS)*, vol. 4, 1994, pp. 147-150.
- [15] S. Panchanathan and M. Goldberg, "A content-addressable memory architecture for image coding using vector quantization," *IEEE Trans. Signal Process.*, vol. 39, no. 9, pp. 2066-2078, Sep. 1991.
- [16] M. Nakanishi and T. Ogura, "Real-time CAM-based Hough transform and its performance evaluation," *Machine Vision Appl.*, vol. 12, no. 2, pp. 59-68, Aug. 2000.
- [17] A. Efthymios and J. D. Garside, "A CAM with mixed serial-parallel comparison for use in low energy caches," *IEEE Trans. Very Large Scale Integr. (VLSI) Syst.*, vol. 12, no. 3, pp. 325-329, Mar. 2004.
- [18] K. Zheng, C. Hu, H. Lu, and B. Liu, "A TCAM-based distributed parallel IP lookup scheme and performance analysis," *IEEE/ACM Trans. Networking*, vol. 14, no. 4, pp. 863-875, Aug. 2006.
- [19] G. Kasai, Y. Takarabe, K. Furumi, and M. Yoneda, "200MHz/200MSPS 3.2W at 1.5V Vdd, 9.4Mbits ternary CAM with new charge injection match detect circuits and bank selection scheme," in *Proc. IEEE Custom Integr. Circuits Conf. (CICC)*, 2003, pp. 387-390.
- [20] I. Arsovski, T. Chandler, and A. Sheikholeslami, "A ternary content-addressable memory (TCAM) based on 4T static storage and including a current-race sensing scheme," *IEEE J. Solid-State Circuits*, vol. 38, no. 1, pp. 155-158, Jan. 2003.
- [21] I. Arsovski and A. Sheikholeslami, "A mismatch-dependent power allocation technique for match-line sensing in content-addressable memories," *IEEE J. Solid-State Circuits*, vol. 38, no. 11, pp. 1958-1966, Nov. 2003.
- [22] K. Pagiamtzis and A. Sheikholeslami, "Pipelined match-lines and hierarchical search-lines for low-power content-addressable memories," in *Proc. IEEE Custom Integr. Circuits Conf. (CICC)*, 2003, pp. 383-386.
- [23] Y.-J. Chang, "Using the dynamic power source technique to reduce TCAM leakage power," *IEEE Trans. Circuits Syst. II, Exp. Briefs*, vol. 57, no. 11, pp. 888-892, Nov. 2010.
- [24] Predictive Technology Model (PTM). [Online]. Available: <http://ptm.asu.edu/>
- [25] M.-C. Chang, K.-L. He, and Y.-C. Wang, "Design of ternary content-addressable memories using FinFET," in *Proc. 24th VLSI Design/CAD Symp.*, 2013, pp. (p1-3) 1-2.
- [26] BGP Routing Table Analysis Reports. [Online]. Available: <http://bgp.potaroo.net/v6/as2.0/index.html/>

An Improved Design of Gallager Mapping for LDPC-coded BICM-ID System

Lin Zhou, Weicheng Huang, Shengliang Peng, Yan Chen and Yucheng He

Abstract—Gallager mapping uses different signal points with different probabilities by assigning several labels for one signal point, and thus provides a promising approach to achieving shaping gains. An important issue in Gallager mapping is how to assign labels for signal points. In this paper, two optimized design rules for Gallager mapping of bit-interleaved coded modulation scheme with iterative decoding (BICM-ID) are proposed, where the Hamming distance among the labels for one signal point should be minimized. The extrinsic information transfer (EXIT) technique is utilized to design and analyze the proposed mapping patterns. Compared with conventional Gallager mapping, our proposed method provides extra shaping gain for the LDPC-coded BICM-ID system. And our proposed method supplies better performance than conventional uniform mapping with the same spectrum efficiency.

Index Terms—low-density parity-check (LDPC) codes, Gallager mapping, quantization mapping, bit-interleaved, iterative decoding.

Original Research Paper
DOI: 10.7251/ELS1620016Z

I. INTRODUCTION

In classical communication theory, coding and modulation had been treated as two separate parts. However, in recent decades, some new techniques [1]–[5] which integrate coding and modulation were devised to improve the performance of system.

The thinking of combined coding and modulation design was first suggested by Massey in [6] and then developed by Ungerboeck (trellis-coded modulation, TCM) [1] and Imai (multilevel coding, MLC) [2]. TCM scheme performs good over the Additive White Gaussian Noise (AWGN) channels but not so good over fading channels. Moreover, the complexity of MLC was very high because the multistage decoder costs too much. In 1992, a scheme named bit-interleaved coded modulation (BICM) was first

introduced by Zehavi [3], and then developed by Li [7] as BICM with iterative decoding (BICM-ID). In past years, BICM-ID scheme with turbo-like decoding had been found very good performance over both AWGN and fading channels [4].

By Shannon's Information Theory, the shaping gain with non-uniform input signal and multi-dimensional signal constellation can asymptotically approach 1.53 dB at most [8]. As so far, a few approaches [10]–[14] have been developed to provide this kind of shaping gain. Among which, non-uniformly spaced signals [11] with equal probability were extensively studied [10], [12], while another kind of shaping method with non-equiprobable signals attracted little attention [9], [13]. Quantization mapping works by generating non-uniform distribution of signal probabilities to approach the optimum input distributions. For the first introduction by Gallager in [8], quantization mapping is also called Gallager mapping. In 2004, a scheme using Gallager mapping and maximum likelihood (ML) decoding was proposed by Bennatan [9], and it could provide some shaping gain. However, the mapping distribution he used in the mapper was not optimally designed and the ML decoding prohibited practical applications for long codes.

In this paper, an improved Gallager mapping scheme for the BICM-ID system based on low-density parity-check (LDPC) codes is presented, where the extrinsic messages are transferred between the LDPC decoder and the signal demapper. No extra shaping code is needed in the proposed scheme, and the improvement of Gallager mapping results in no extra complexity for communication systems.

II. SYSTEM MODEL

The system proposed in this paper is described in Fig. 1, where LDPC codes and quantization mapper are utilized. Assume a two-dimensional constellation $\mathcal{A}_x = \{a_i | 0 \leq i \leq M-1, a_i \in \mathbb{C}\}$ of size M is used. The input vector $\mathbf{u} = (u_0, u_1, \dots, u_{K-1})$ of information symbols is first encoded by the LDPC encoder into a codeword $\mathbf{c} = (c_0, c_1, \dots, c_{N-1})$, then interleaved and producing a bit sequence $\mathbf{v} = (v_0, v_1, \dots, v_{N-1})$. The Gallager mapper generates signal vectors $\mathbf{x} = (x_0, x_1, \dots, x_j, \dots)$ with $x_j = \mathcal{M}(v'_j)$, where j denotes the index of the modulated symbols, $\mathcal{M}(\cdot)$ stands for the signal mapping function and

Manuscript received 4 September 2015. Accepted for publication 25 December 2015.

The authors wish to thank Prof. Bai of Xidian University and the referees for their helpful reviews.

This work was supported in part by the Natural Science Foundation of China (No. 61302095, 61101127, 61201264, 61401165), the Natural Science Foundation of Fujian Province of China (No.2014J05076, 2014J01243), and the Natural Science Foundation of Huaqiao University (No. 12BS219, 13Y0384).

Lin Zhou, Weicheng Huang, Shengliang Peng, Yan Chen and Yucheng He are with Xiamen Key Lab of Mobile Multimedia Communications, Huaqiao University, Xiamen, 361021, China, and Lin Zhou and Yucheng He are also with the State Key Lab of ISN, Xidian University, Xi'an, 710071, China (e-mail: linzhou@hqu.edu.cn).

$\mathbf{v}'_j = (v'_{j,1}, v'_{j,2}, \dots, v'_{j,T})$ is a T -bit-length vector which extracted from \mathbf{v} , and the value of T depends on the mapping function $\mathcal{M}(\cdot)$.

Suppose the complex signal vector \mathbf{x} is transmitted over the AWGN channel. The received vector $\mathbf{y} = (y_0, y_1, \dots, y_j, \dots)$ is then given by

$$y_j = x_j + n_j \quad (1)$$

where $n_j \sim CN(0, N_0)$ are independent and identically distributed complex Gaussian random variables with zero mean and variance $N_0/2$ per dimension.

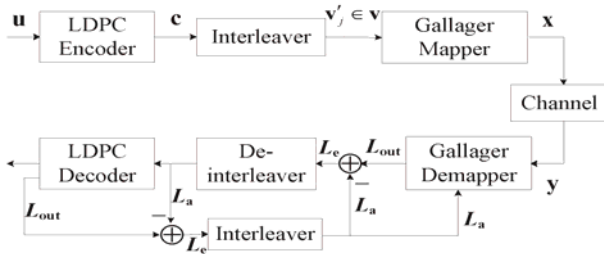


Fig.1 Block diagram of the system model

At the receiver, the received signal y from the channel is firstly processed by the Gallager demapper, and the extrinsic information L_e is delivered to the LDPC decoder after the interleaving. Then the output extrinsic information of the demapper is de-interleaved and fed back to the LDPC decoder as the *a priori* information L_a . This iterative process continues until certain condition is satisfied.

The Gallager demapper processes the received symbol y_j and the corresponding a priori log-likelihood ratio (LLR)

$$L_a(v'_{j,t}) = \log \left(\frac{P(v'_{j,t} = 0)}{P(v'_{j,t} = 1)} \right) \quad (2)$$

where $j = 0, 1, 2, \dots$, and $t = 1, 2, \dots, T$ to generate the extrinsic information L_e as follows,

$$\begin{aligned} L_e(v'_{j,t}) &= L_{out}(y_j, L_a(v'_{j,t})) - L_a(v'_{j,t}) \\ &= \log \left(\frac{P(v'_{j,t} = 0 | y_j, L_a(\mathbf{v}'_j))}{P(v'_{j,t} = 1 | y_j, L_a(\mathbf{v}'_j))} \right) - L_a(v'_{j,t}) \end{aligned} \quad (3)$$

which is then delivered to the LDPC decoder and taken as the *a priori* information for decoding. Next, the extrinsic information of the LDPC decoder should be fed back to the Gallager demapper as the *a priori* information. Apparently, the demapper and decoder exchange the extrinsic information in an iterative manner.

III. IMPROVED GALLAGER MAPPING

A. Quantization Mapping

Let $\{P(x) | x \in \mathcal{A}_x\}$ be a probability mass function set associated with constellation \mathcal{A}_x . For a conventional signal mapper, the signal points are used with equal possibility, and the corresponding mapping function can be expressed as $P(x) = 1/M$.

Definition 1. As described in [8], A quantization $\mathcal{Q}_{P(x)}(\mathbf{v}'): \{0, 1\}^T \rightarrow \mathcal{A}_x$ is a mapping from labels \mathbf{u} of length T to $x \in \mathcal{A}_x$, such that the number of labels mapped to x is $2^T P(x)$. For brevity, we use $\mathcal{Q}(\mathbf{v}')$ for $\mathcal{Q}_{P(x)}(\mathbf{v}')$.

Note that, $P(x)$ can be a non-uniform distribution. Thus when applying the quantization mapping distribution to input sequences, the resulted signals $\{x_0, x_1, \dots, x_j, \dots\}$ over the constellation space has the potential to provide shaping gain.

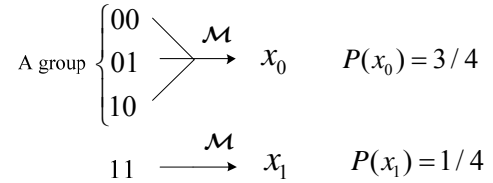


Fig.2 An example of quantization mapping

Example 1. Quantization mapping for 2-bit-length symbols

An example is presented to help understanding the definition of quantization mapping. The two points of the constellation are used with the unequal probability of 3/4, 1/4, respectively. In this paper, all symbol sequences which are corresponding to a same point are called labels within a group, and are shown in Fig. 2.

B. Optimal Input Distribution

Let X denotes the transmitted symbol, Y denotes the received symbol. The channel capacity will be approached when the mutual information $I(X; Y)$ is maximized. For a discrete-time memoryless AWGN channel, according to [16], X should be subjected to Gaussian distributed to maximize the mutual information $I(X; Y)$.

Lemma 1. If a random variable satisfy the following restriction

$$\sigma_v^2 = \int_{-\infty}^{+\infty} p(v)(v-m)^2 dv < \infty \quad (4)$$

, where σ_v and m are the covariance and mean value of v , respectively. Then

$$H(V) \leq \log \sqrt{2\pi e} \sigma_v \quad (5)$$

with equality if and only if v is subject to Gaussian

distribution, where V is the set of v , and $H(V)$ denotes the entropy of V .

Theorem 1. For a discrete-time memoryless AWGN channel, the optimal input distribution of X , which maximizes the mutual information $I(X;Y)$ is subject to Gaussian distribution.

Let $C \triangleq \text{Max}I(X;Y)$, where C denotes channel capacity, since

$$I(X;Y) = H(Y) - H(Y|X) = H(X+N) - H(N) \quad (6)$$

According to *Lemma 1*, X should be Gaussian distributed to achieve the channel capacity.

In 2004 [9], Bennatan found some good non-uniform input distributions close to optimal distribution for the discrete-time AWGN channel. However, the mapping labels in natural (ascending or descending) order were used in his scheme, which resulted performance loss for practical schemes.

C. Improved Gallager Mapping

As pervious description, for Gallager mapping, every constellation point may correspond to one or more coded symbol sequences. The problem of finding good mapping patterns is how to design the probabilities of every point and which labels should be assigned into a same group. Based on the theory of optimal input distribution and the characteristic of overlapped labels in Gallager mapping, we propose two mapping rules to solve the problem and improve the performance of BICM-ID system with Gallager mapping. And the academic explanations will be given in section IV.

Rule 1: Let the probability mass function of the signal points in the employed constellation approach the discrete-time Gaussian distribution;

Rule 2: Try to minimize the Hamming distance among the different labels within every group.

Note that the mathematical demonstration of *Rule 1* has been given in the foregoing Section III B for a discrete signaling over an AWGN channel, the output of the mapper should follow the discrete Gaussian distribution as much as possible. While according to *Rule 2*, the number of reliable coded bits is guaranteed to be as large as possible when recovering the coded bits sequences from the signal points. In other words, the number of bits recovered with low reliability is as few as possible by *Rule 2*. Unfortunately, it is hardly to analysis *Rule 2* by mathematical equations, so computer-based analysis and simulations will be provided in the next sections.

IV. ANALYSIS OF PROPOSED GALLAGER MAPPING

In the previous section, two rules for the improved Gallager mapping method based on BICM-ID system are presented. To further illustrate the effect of the proposed

mapping rules and find good mapping patterns, the technique of EXIT chart [15] is employed to analyze the iterative system.

As is known, the LDPC decoder can be seen as concatenation of variable-node decoder (VND) and check-node decoder (CND). Thereby, we could expressly partition the receiver in Fig. 1 into two blocks, which is depicted in Fig. 3, where block **A** mainly consists of the demapper and variable-node decoder, and block **B** solely comprises the check-node decoder. I_A , I_B and I_D denote the mutual information at the output end of block **A**, **B**, and demapper, respectively.

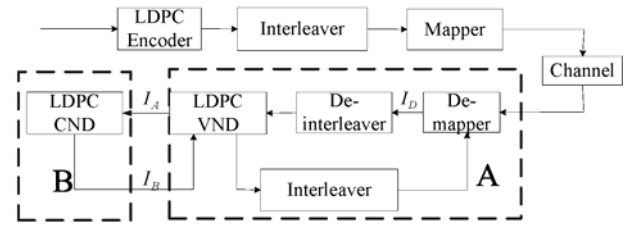


Fig. 3. EXIT Chart analysis model of our scheme

At the receiving end, the Soft-In-Soft-Out (SISO) demapper processes the channel-corrupted sequences, and generates the posteriori log-likelihood ratios (LLRs) to the LDPC decoder for reconstruction. Indeed, the information exchange not only exists between the SISO demapper and the decoder, but also inside the LDPC decoder. Hence, based on Fig. 3, the overall decoding process can be formulated as follows.

Step 1. The SISO modulator computes LLRs and sends them to the LDPC VND after de-interleaving, and the output of LDPC VND is what block **B** received from block **A**.

Step 2. The LDPC CND, i.e., block **B** operates on the received extrinsic information to compute what to be passed to block **A**.

Note that only extrinsic information is exchanged in between. Hence, it is possible to draw EXIT curves for both blocks. According to [17], [18] the approximate formulas to compute I_A and I_B are given as follows.

$$I_B = 1 - \sum_j \rho_j J\left(\sqrt{j-1}J^{-1}(1-I_A)\right) \quad (7)$$

$$I_A = \sum_j \lambda_j J\left(\sqrt{(i-1)(J^{-1}(I_B))^2 + (J^{-1}(I_D))^2}\right) \quad (8)$$

, where the details of the $J(\bullet)$ function was defined in [17], and $\lambda(x)$, $\rho(x)$ express the degree distributions of LDPC codes.

Then given a regular LDPC code assemble $C(3,6)$ over the AWGN channel, the design of good Gallager mapping patterns will be presented by EXIT Chart analysis. As is known, the best performance will be achieved when the curves of variable-node decoder and signal demapper

proposed scheme. That is to say, when E_b/N_0 is larger than 9.6 dB or 5.4 dB, respectively, the two proposed schemes can successfully work without any errors by using good enough channel codes.

V. SIMULATION RESULTS

In this section, a rate-1/2, length-9216 regular binary (3,6) LDPC code from China Mobile Multimedia Broadcasting (CMMB) [19] and a rate-2/3 length-9216 regular (3,9) LDPC code will be used to demonstrate the effectiveness of our proposed mapping method for the LDPC-coded BICM-ID system over AWGN channels. As known, the standard sum-product decoding algorithm (SPA) is the most popular algorithm for LDPC decoding [20], and the most common number of iteration should be 50. To ensure the fairness of comparison between the proposed Gallager-mapping-based system and the traditional system, the maximum inner iteration number of our proposed LDPC decoder is set to be 10, and furthermore, the outer iteration number between the demapper and LDPC decoder is set to be 5. So the computational complexity of our proposed scheme is almost the same as the traditional LDPC-coded BICM-ID scheme.

Fig. 8 shows the performance of length-4 symbols which are mapped to the conventional 8-PAM (shown in Fig. 4) and conventional 16-PAM set by using the rate-1/2 LDPC code. At the BER of 10^{-5} , almost 0.5 dB and 0.2 dB of extra shaping gain are attained by proposed Gallager mapping over the conventional Gallager mapping and traditional 16-PAM mapping, respectively. The spectral efficiency of the proposed scheme is 2 bit/s/Hz. Fig. 9 shows the performance of length-4 symbols which are mapped to the conventional 8-PAM set (shown in Fig. 4) and conventional 16-PAM set by using the rate-2/3 LDPC code. Similar results will be obtained. At the BER of 10^{-5} , almost 1.2 dB and 0.2 dB of extra shaping gain are attained by proposed Gallager mapping over the conventional Gallager mapping and traditional 16-PAM mapping, respectively. The spectral efficiency of the proposed scheme is 2.67 bit/s/Hz.

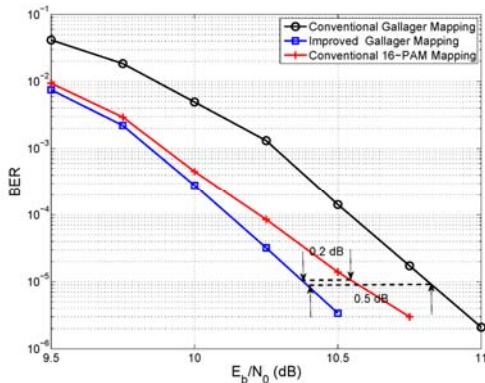


Fig. 8. Performance of 8-PAM Gallager mapping, R=1/2

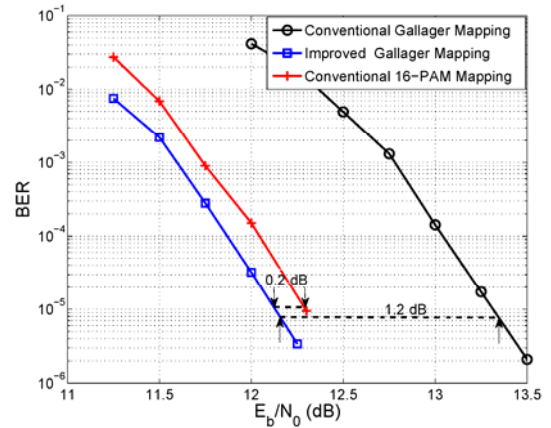


Fig. 9. Performance of 8-PAM Gallager mapping, R=2/3

As known, 16-QAM signaling is one of the most popular modulation types in modern digital communication system. Fig. 10 shows the performance of different modulation schemes with the same spectral efficiency of 2.5 bit/s/Hz. It can be observed that, at the BER of 10^{-5} , the proposed Gallager mapping outperforms the conventional Gallager mapping by 1dB and is 0.2 dB better than the conventional 32-QAM with outer iteration.

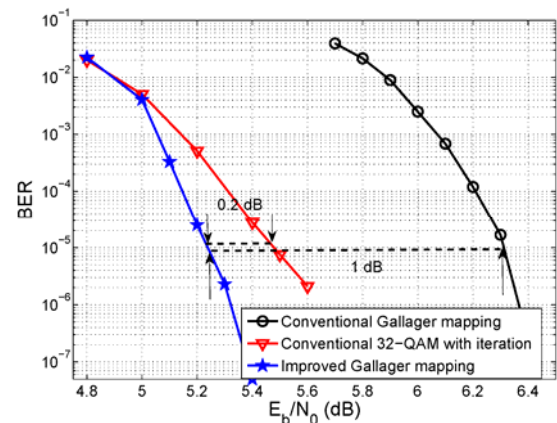


Fig. 10. Performance of 16-QAM Gallager mapping, R=1/2

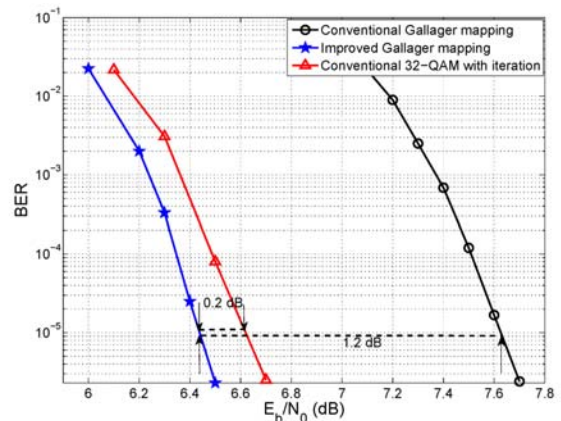


Fig. 11. Performance of 16-QAM Gallager mapping, R=2/3

Fig. 11 shows the performance of different modulation schemes with the same spectral efficiency of 3.33 bit/s/Hz. Comparing with the conventional Gallager mapping and the traditional 32-QAM mapping, our improved Gallager mapping obtain 1.2 dB and 0.2 dB extra shaping gain, respectively.

VI. CONCLUSION

In this paper, we presented an improved Gallager mapping method for the BICM-ID scheme based on LDPC codes, which could generate Gaussian-like input distributions and improved mapping within each group to obtain extra shaping gain without any other shaping codes. In fact, the proposed scheme could be generalized to any codes with iterative decoding, such as turbo-like codes.

The EXIT chart analyses were used to optimize the mapping patterns and supply some information-theoretic explanations for the proposed method. The threshold of the proposed scheme was improved obviously. Numerical results demonstrated that the proposed scheme were not only much better than conventional Gallager mapping, but also a little bit better than BICM-ID systems based on traditional uniform mapping with the same spectral efficiency.

The advantages of the proposed scheme are manifested in two aspects: 1) BER performance is improved because of the extra shaping gain and coding gain; 2) Higher spectral efficiency can be achieved by using lower-order modulation types, which can decrease the complexity of the signal mapper. The above advantages will make it to be an attractive candidate for future communication systems with turbo-principle-based receivers.

REFERENCES

- [1] G. Ungerboeck, "Channel coding with multilevel/phase signals," *IEEE Trans. Inform. Theory*, vol. IT-28, pp.55-67, 1982.
- [2] H. Imai and S. Hirakawa, "A new multilevel coding method using errorcorrecting codes," *IEEE Trans. Inform. Theory*, vol. IT-23, pp. 371-377, May 1977.
- [3] E. ZEHAVI, "8-PSK trellis coeds for a Rayleigh fading channel," *IEEE Trans. Commun.*, vol. 40, pp. 873-884, May 1992.
- [4] G. Caire, G. Taricco, and E. Biglieri, "Bit-interleaved coded modulation," *IEEE Trans. Inf. Theory*, vol. 44, no. 3, pp. 927-946, May 1998.
- [5] G. D. Forney, Jr. and G. Ungerboeck, "Modulation and coding for linear Gaussian channels," *IEEE Trans. Inform. Theory*, vol.44, no.6, pp. 2384-2415, Oct. 1998.
- [6] J. L. Massey, "Coding and modulation in digital communications," *Proc. 1974 Int. Zurich Seminar on Digital Comm.*, Zurich, Switzerland, pp. E2(1)-(4), Mar. 1974.
- [7] X. Li and J. A. Ritcey, "Bit-interleaved coded modulation with iterative decoding using soft feedback," *IEEE Commun. letters*, vol. 1, pp. 169-171, November 1997.
- [8] R. G. Gallager, *Information Theory and Reliable Communication*. New York: Wiley, 1968.
- [9] A. Bennatan and D. Burshtein, "On the application of LDPC codes to arbitrary discrete-memoryless channels," *IEEE Trans. Inf. Theory*, vol. 50, no. 3, pp. 417-438, Mar. 2004.
- [10] C. Fragouli, R. D. Wesel, D. Sommer, and G. Fettweis, "Turbo codes with nonuniform QAM constellations," in *Proc. IEEE Int. Conf. Commun.*, Helsinki, Finland, Jun. 2001, vol. 1, pp. 70-73.
- [11] Mao-Ching Chiu, "Bandwidth-Efficient Modulation Codes Based on Nonbinary Irregular Repeat-Accumulate Codes," *IEEE Transactions on Information Theory*, vol.56, no.1, pp.152-167, Jan. 2010
- [12] M. J. Hossain, A. Alvarado and L. Szczecinski, "BICM trasmission using non-uniform QAM constellations: performance analysis and design," in *Proc. IEEE Int. Conf. Commun.*, Cape Town, South Africa, 2010.
- [13] A. G. Fabregas and A. Martinez, "Bit-interleaved coded modulation with shaping," in *Proc. IEEE Inf. Theory Workshop*, Dublin, Ireland, 2010.
- [14] H. S. Cronie, "Signal Shaping for Bit-Interleaved Coded Modulation on the AWGN Channel," *Communications, IEEE Transactions on* , vol.58, no.12, pp.3428-3435, December 2010
- [15] S. ten Brink, "Convergence behaviour of iteratively decodable parallel concatenated codes," *IEEE Trans. Commun.*, vol. 49, pp. 1727-1737, Oct. 2001.
- [16] T. M. Cover, *Element of Information Theory*. New York: Wiley, 1991.
- [17] S. ten Brink, G. Kramer, and A. Ashikhmin, "Design of low-density parity-check codes for modulation and detection," *IEEE Trans. Commun.*, vol. 52, no. 4, pp. 670-678, Apr. 2004.
- [18] W. H. Press, S. A. Teukolsky, W. T. Vetterling, and B. P. Flannery, *Numerical Recipes* in C. New York: Cambridge Univ. Press, 1997.
- [19] "Mobile Multimedia Broadcasting Part 1: Framing Structure, Channel Coding and Modulations for Broadcasting Channel," <http://gb123.sac.gov.cn/gb/showGb?gbCode=GB>
- [20] M. K. Roberts, R. Jayabalan, "An improved low complex Sum-Product decoding algorithm for low-density parity-check codes," *Frontiers of Information Technology and Electronic Engineering* , pp.1-8, Jan. 2015

Design and Implementation of a Novel Directional Coupler for UHF RFID Reader

Jianxiong Li, Shanlin Song, Xiaoyu Chen, Hua Nian and Weiguang Shi

Abstract—The directional coupler is applied to isolating RX from TX because of low cost and simplicity compared to the circulator in the radio-frequency identification (RFID) reader. Because of unequal phase velocity between odd and even mode, the drawback of the traditional microstrip directional coupler is poor isolation. In this paper, to obtain a good isolation between RX and TX, a novel directional coupler is proposed to be applied to the UHF RFID system with a single antenna. Measurement result shows that the proposed directional coupler possesses a good isolation of -35dB in operating frequency band.

Index Terms—Isolation, Directional Coupler, Radio-frequency identification (RFID)

Original Research Paper

DOI: 10.7251/ELS1620022L

I. INTRODUCTION

Radio-frequency identification (RFID) technology is becoming more and more popular from the 1990s [1], its applications are extending rapidly and the commercial potential is getting huger and huger [2]. It uses radio-frequency signal to realize automatic identification of object through space coupling. The biggest advantage of the UHF RFID is that it can complete identification without physical contact [3]. A set of the UHF RFID system is composed of the reader, the electronic tag and the application software. In the common passive UHF RFID system, the reader transmits continuous waves to the tag, part of the continuous waves will be converted into energy by the tag, and the tag sends its back-scattered data to the reader. Because continuous wave from the reader and back-scattered wave from the tags simultaneously occupy the same frequency band, TX leakage to RX leads to many technical difficulties. For example, the strong TX leakage makes the low noise amplifier (LNA) of the

receiver saturated and the dynamic range of the LNA decreased [1]. In order to improve the performance of the RFID reader, a novel directional coupler is proposed to obtain high isolation between RX and TX. An attenuator, a phase shifter and a power synthesizer are added at the coupling port of the transmit chain at the same time. The signal of the anti-phase and equal magnitude of the TX leakage is designed by using the attenuator and the phase shifter at the coupling port, and combined with the TX leakage at the isolation port. Consequently, these two signals are offset by using the power synthesizer. Accordingly, RX is isolated from the TX leakage effectively and thus the proposed directional coupler can be applied to the UHF RFID reader.

II. INTRODUCTION OF THE PRINCIPLE

A. Introduction of the directional coupler

The directional coupler is a kind of passive microwave component and power distribution component, which is widely used in power distribution and synthesis [4]. The four ports of directional coupler are the input port, the output port, the coupling port and the isolation port, respectively. The transmitted signals from the input port are moved to the output port and the coupling port according to certain proportion, no signals to the isolation port ideally.

As reciprocal network, the function of each port is interchangeable. Each port can be the input port, the function of other ports changes in turn.

Because of its port reciprocity, the proposed directional coupler is applied to the RFID reader which shares a single antenna, as shown in Fig. 1. In TX, transmitter connects port 1 of the directional coupler. At this point, port 1 serves as the input port, port 2 as the isolation port, port 3 as the coupling port, port 4 as the output port. The transmitted signals transferred to the output port are radiated through the antenna. In RX, the antenna connects port 4 of the directional coupler. At this point, port 4 serves as the input port, port 1 as the output port, port 2 as the coupling port, port 3 as the isolation port. The received signals are transferred through the coupling port. In this way, the directional coupler provides the maximum isolation between RX and TX.

The isolation between the transmitter and the receiver is provided by the directional coupler completely. Nevertheless, the isolation of the directional coupler is limited, and the

Manuscript received 4 September 2015. Accepted for publication 25 December 2015.

Jianxiong Li is with the School of Electronics and Information Engineering, Tianjin Polytechnic University, Tianjin, China (e-mail: lijianxiong@tjpu.edu.cn).

Shanlin Song is with the School of Electronics and Information Engineering, Tianjin Polytechnic University, Tianjin, China.

Xiaoyu Chen is with the School of Electronics and Information Engineering, Tianjin Polytechnic University, Tianjin, China.

Hua Nian is with the School of Electronics and Information Engineering, Tianjin Polytechnic University, Tianjin, China.

Weiguang Shi is with the School of Electronics and Information Engineering, Tianjin Polytechnic University, Tianjin, China.

transmitted signal will leak to RX inevitably, which makes the performance of the receiver worse.

B. Analysis of the carrier leakage

The passive UHF RFID system communicates by back-scattered communication. Although the reader and the tag send information in half-duplex communication which agreement stipulated, back-scattered communication requires that the tag sends signal when energy signal is transmitted by the reader, so it also can be regarded as full-duplex communication. Other full-duplex communication devices cannot be interfered with each other by using different frequency band. However, continuous wave from the reader and back-scattered wave from the tags simultaneously occupy the same frequency band. Therefore, they cannot be filtered by the filter if they enter into RX at the same time. At present, the directional couplers are extensively applied to insulate RX from TX in the UHF RFID reader, as shown in Fig. 2. The transmitted signal of the transmitter will leak into RX inevitably due to the fact that the directional coupler has limited isolation. And the leakage signal is stronger than the back-scattered signal of tags, which makes the LNA of the receiver saturation easily. As a result, the received signal cannot be amplified effectively. Since the leakage signal will lower the signal to noise ratio, it has an adverse effect on the detection rang of the tag [5].

If the transmitted power of the transmitter is 30dBm, according to the formula of Friss:

$$P_r = \frac{P_t G_t G_r \lambda^2}{(4\pi R)^2} \quad (1)$$

where G_t is the gain of the reader antenna, G_r the gain of the tag antenna, P_t the transmitted power by the reader, P_r the received power by the reader, λ the wavelength.

When the tag is 10 meters away from the reader, $G_t = 8\text{dBi}$ and $G_r = 1.2\text{dBi}$, the back-scattered power of the tag is above -60dBm for proper communication. If the isolation of the directional coupler is -20dB, there will be 10dBm transmitted signal leaks into RX. In this way, the 10dBm noise added to the -60dBm effective signal, which will lead to the signal to noise ratio very poor inevitably. In addition, the linearity of the LNA will not very high, if the 1dB compression point of the LNA less than 10dBm, the 10dBm noise will cause the LNA saturation which is unable to enlarge effective signal. Therefore, we must try to increase the isolation of the

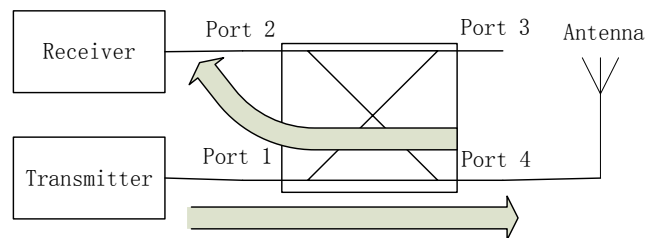


Fig.1 Structure of single antenna transceiver

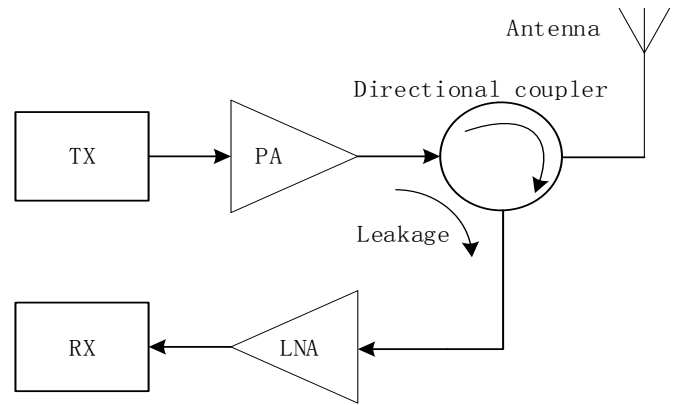


Fig.2 Circuit diagram of the transceiver isolation

directional coupler.

C. Improving method of the directional coupler

This paper uses directional coupler chip RCP890A05 as the isolation component of the transceiver. The proposed technique to increase the isolation is that the canceling loop is designed and offsets TX leakage. The canceling loop includes the attenuator, the phase shifter and the power synthesizer and the principle circuit is created in Agilent ADS 2009 as shown in Fig. 3. The model of the directional coupler is set by the parameters of the RCP890A05 chip in the simulation. Port 1 connects the transmitter as the input port, port 2 connects the antenna as the output port, port 3 is the coupling port, port 4 is the isolation port. The coupling signal travels through the attenuator and the phase shifter, and combines with the leakage of the isolation port by the power synthesizer which connects to the receiver. The phase difference between the coupling signal and the leakage changes from 90° to 180° through the phase shifter. Then the coupling signal becomes the same magnitude with the leakage through the attenuator. At last, two signals are cancelled out in the power synthesizer. Consequently, the proposed directional coupler increases the isolation.

Assuming the leakage of the isolation port is

$$S_{leak}(t) = A_{leak} \cdot \cos(\omega t) \quad (2)$$

The back-scattered signal which the antenna receives is

$$S_V(t) = A_V(t) \cdot \cos(\omega t + \varphi) \quad (3)$$

The coupling signal of the transmitter is

$$S_{C0}(t) = A_C \cdot \cos(\omega t + 90^\circ) \quad (4)$$

The coupling signal through the attenuator and the phase shifter is

$$S_C(t) = kA_C \cdot \cos(\omega t + 90^\circ + \varphi_C) \quad (5)$$

where k is the coefficient of the attenuation and φ_C is the amount of the phase-shift.

Three signals are combined in the power synthesizer, that is

$$S_R(t) = S_{leak}(t) + S_C(t) + S_V(t) \quad (6)$$

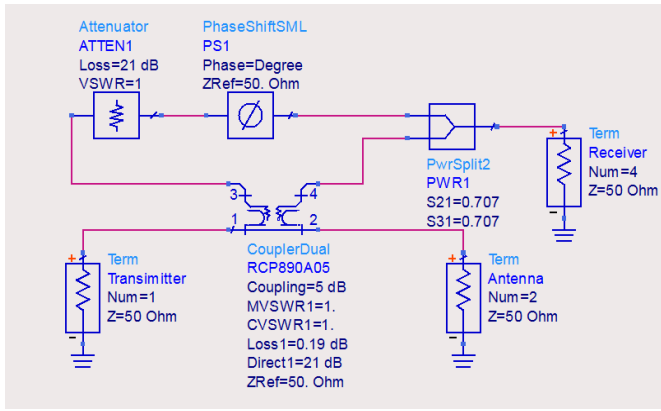


Fig.3 Principle circuit of the proposed directional coupler

If one wants to increase the isolation, the leakage S_{leak} should be reduced as much as possible. Ideally, $S_{leak} + S_C = 0$. As a result, two signals will be cancelled out for the same magnitude and the contrary phase, as shown in (7) and (8):

$$A_{leak} = kA_C \quad (7)$$

$$90^\circ + \varphi_C = 180^\circ \quad (8)$$

In practice, however, it is difficult to obtain absolutely equal value, and the frequency change will cause phase change. So it can only minimize the leakage, but cannot cancel out the leakage completely.

The simulation results using Agilent ADS 2009 in Table I show that the proposed directional coupler improves the isolation of the chip from -26dB to -342dB, which all the components are ideal. Therefore, in theory, the proposed method is feasible.

III. DESIGN OF THE DIRECTIONAL COUPLER

Actual model is added in Agilent ADS 2009, as shown in Fig. 4. The attenuator uses the π attenuation network instead, the phase shifter uses the microstrip line instead, and the power synthesizer is the Wilkinson power synthesizer which is made up of microstrip line. Adjusting the attenuation of the attenuation network makes the leakage of the isolation port and the coupling signal the same magnitude, then only adjusting the size of the microstrip line of the phase shifter makes the phase difference between the leakage and the phase-shifted signal equal to 180° . Layout is made to do electromagnetic simulation and frequency band of the simulation is from 860MHz to 960MHz. The simulation results of the physical layout at frequency of 915MHz are shown in Fig. 5. The insertion loss (m4) is about -1.7dB in TX, the isolation (m6) between RX and TX is -53dB which shows that the proposed directional coupler has higher isolation, and the coupling (m5) between the antenna and the receiver is -8dB in RX.

Because the actual board and the layout are not ideal, we also need to adjust the size of the phase shifter and the attenuator according to measured results finally.

	RCP890A05	directional coupler
Isolation.	-26dB	-342.769dB

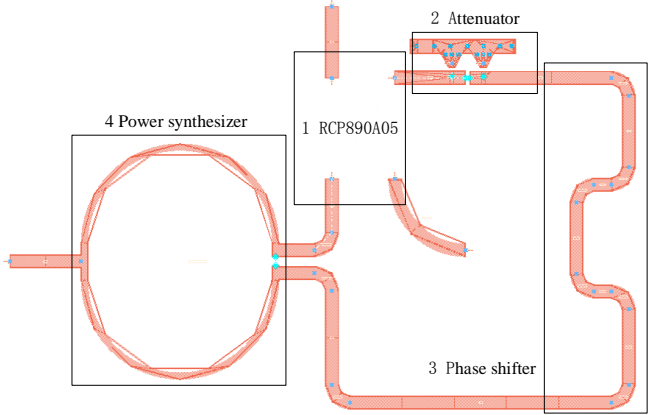


Fig.4 Layout of the proposed directional coupler

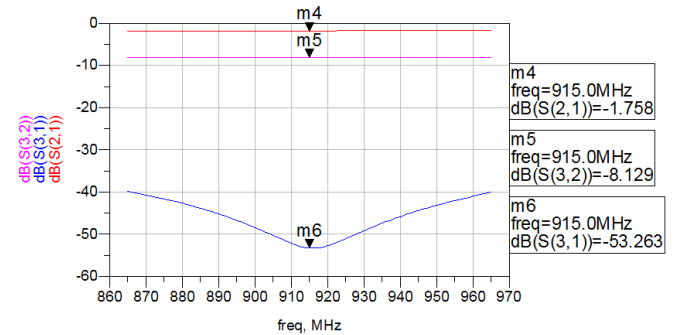


Fig.5 Simulation results of the layout

IV. TEST AND ANALYSIS OF THE PROPOSED DIRECTIONAL COUPLER

The main function of the directional coupler is to isolate RX from TX, so the important index of testing is the isolation. There will be energy loss when the signal is transmitted from the transmitter to the antenna through the directional coupler, so one needs to test the insertion loss between the input and the output. One also needs to test the coupling of RX due to the fact that the received wave is transferred through the coupling port [6]. Fig. 6 shows the physical picture of the proposed directional coupler. To demonstrate the correctness of the proposed directional coupler, the experimental set-up uses a network analyzer for measuring the S-parameters of the directional coupler.

The proposed directional coupler has the isolation of -35dB at 915MHz as shown in Fig. 7 which is higher isolation than the directional coupler chip as expected. The actual circuit has many unideal factors so that the measured result is not -53dB obtained by the simulation. As shown in Fig. 8, the insertion loss is almost similar with that of the directional coupler chip.

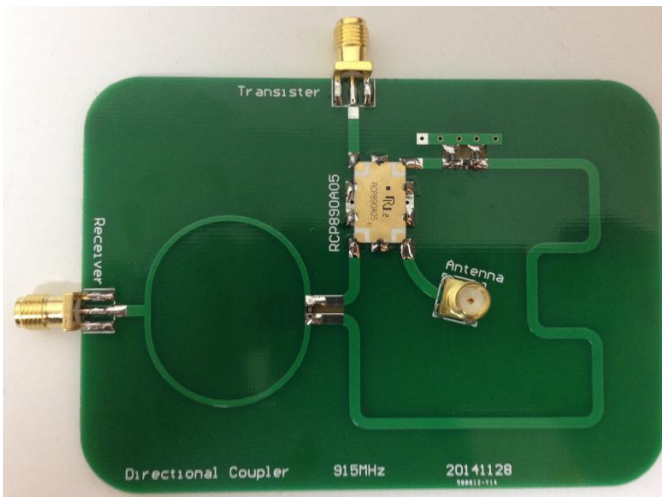


Fig.6 Physical picture of the proposed directional coupler

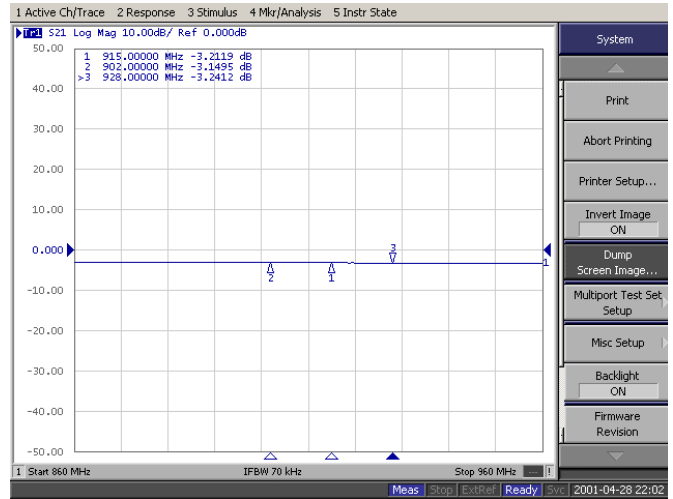


Fig.8 Insertion loss of the proposed directional coupler

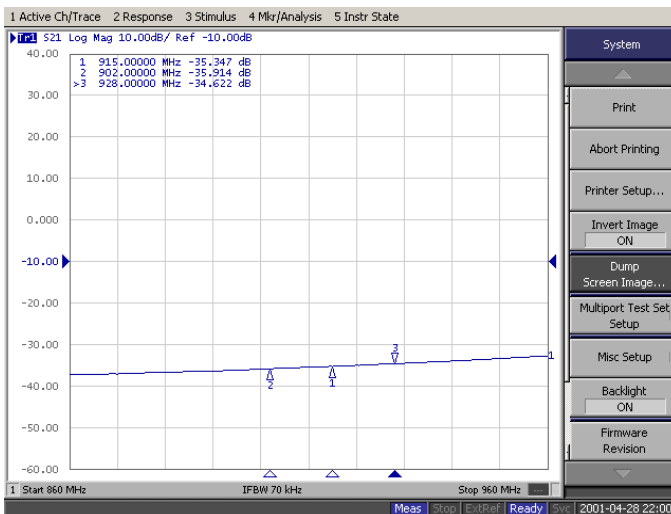


Fig.7 Isolation of the proposed directional coupler

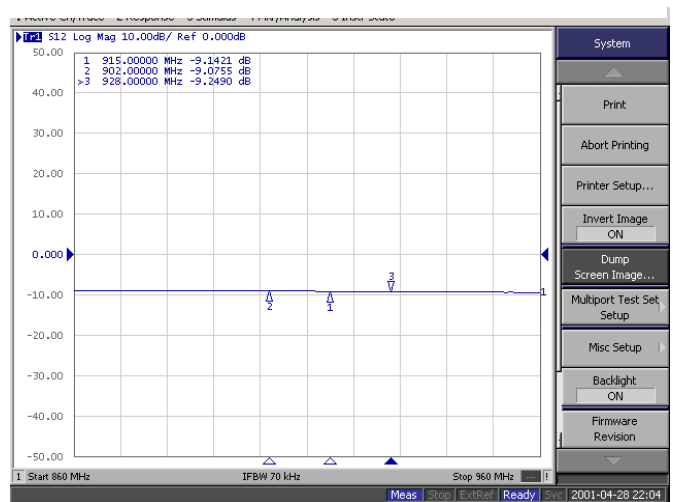


Fig.9 Coupling of the proposed directional coupler

In Fig. 9, the coupling of the proposed directional coupler exhibits -9.1dB. The return loss of each port is less than -10dB which is a good match to the 50Ω load.

TABLE II is the performance contrast of the chip RCP890A05 and the proposed directional coupler. The proposed directional coupler improves the isolation of about 10dB compared with the chip, which decreases the design difficulty of the LNA to a great extent, achieving the purpose of improvement. However, the coupling lowers a little and it is still in the acceptable range. In general, the proposed directional coupler has reached the purpose.

V. CONCLUSION

New method for increasing the isolation of the directional coupler of the UHF RFID reader has been presented. The proposed directional coupler includes the canceling loop to offset TX leakage. The proposed directional coupler possesses a good isolation of -35dB at 915MHz, about 10dB higher than before, and is able to remarkably enhance the sensitivity of the receiver.

TABLE II
PERFORMANCE CONTRAST OF THE DIRECTIONAL COUPLER

	<i>RCP890A05</i>	<i>directional coupler</i>
<i>Isolation</i>	-26dB	-35dB
<i>Coupling</i>	-6.2dB	-9.1dB
<i>Insertion loss</i>	-3.2dB	-3.2dB

REFERENCES

- [1] Kim. Wan-Kyu, Lee. Moon-Que, Kim. Jin-Hyun, Lim. Hyung-Sun, Yu. Jong-Won, Jang. Byung-Jun, Park. Jun-Seok, A passive circulator with high isolation using a directional coupler for RFID, IEEE MTT-S International Microwave Symposium Digest, p 1177-1180, 2006.
- [2] Desong Wan, Bin You, Lingling Sun. Radio link analysis and design of directional coupler with high isolation for UHF RFID reader, Communication Technology, 2008. ICCT 2008. 11th IEEE International Conference on.
- [3] K. Finkenzerler, RFID Handbook, Radio-Frequency Identification Fundamentals and Applications, New York, Wiley, 2003.
- [4] Jin - Wook Jung, Kwan - Kyu Nae, Jay Prakash Thakur, Hong - Gu Cho, Jun - Seok Park. Directional coupler for UHF mobile RFID reader, Microw. Opt. Technol. Lett.,2007,497.

- [5] Quan Xu, Kang Xie, Jun Tang, Jiang Ping. Directional coupler design based on coupled cavity waveguides in photonic crystals, *Optik - International Journal for Light and Electron Optics*,2010,12213.
- [6] Zhongbao Wang, Shaojun Fang, Shiqiang Fu, Xiaoming Li. A Broadband 3 dB Coplanar Waveguides Directional Coupler with Conductor-backed Asymmetric Coplanar Waveguides Compensation, *IETE Journal of Research*,2012,581.

High Dimensional Electromagnetic Interference Signal Clustering Based On SOM Neural Network

Hongyi Li , Di Zhao, Shaofeng Xu, Pidong Wang and Jiaxin Chen

Abstract— In this paper, we study the spectral characteristics and global representations of strongly nonlinear, non-stationary electromagnetic interferences (EMI), which is of great significance in analysing the mathematical modelling of electromagnetic capability (EMC) for a large scale integrated system. We firstly propose to use Self-Organizing Feature Map Neural Network (SOM) to cluster EMI signals. To tackle with the high dimensionality of EMI signals, we combine the dimension reduction and clustering approaches, and find out the global features of different interference factors, in order to finally provide precise mathematical simulation models for EMC design, analysis, forecasting and evaluation. Experimental results have demonstrated the validity and effectiveness of the proposed method.

Keywords - EMI, mathematical simulation models, SOM.

Original Research Paper

DOI: 10.7251/ELS1620027L

I. INTRODUCTION

With the rapid development of science and technology, the electromagnetic equipment gradually tends to be the large-scale integrated system. The existing measurements are designed for the whole system, and the interference elements are generated by the system components. Thus, the precision and accuracy of the EMI factor analysis will have a certain deviation and uncertainty, and we cannot accurately diagnose various interference factors. Therefore, we need to study

mathematical modelling and simulation, namely mathematical representation, of EMI elements from the whole system. Due to the large scale integration of electromagnetic system, EMI signals present high-dimensional, strongly nonlinear and non-stationary characteristics, which existing mathematical models always fail to work. We need to study new mathematical representation methods, that is, to separate and decompose the various interference factors out of the system signal, based on which, we could find out the typical EMI elements such as clustering and so on. Finally, we can provide precise mathematical simulation model for the electromagnetic compatibility design, analysis, prediction and evaluation.

Existing institutions to carry out research in EMC technology can be roughly divided into two categories. One is the national research institution, such as the American NIST, the British NPL and German PTB and so on. They mainly engaged in all kinds of measuring probe antenna, magnetic field, electric field probe calibration and EMC test site research, and provide services. The other is specially engaged in calibration services companies and calibration laboratory of EMC test equipment manufacturers.

On the theoretical research, the IEEE have long noted the problem of radio interference, in October 1957 set up the RF interference professional group, and in May 1959 published the Journal of Radio Frequency Interference (RFI) volumes. In 1964, IEEE proceedings turned the RFI volumes to EMC volumes, the Institute (EMC Society) organizes an important academic conference every year [1].

Several typical existing methods to solve the problem of EMC are the differential equation method based on communication space discretization, the integral equation method based on the scattering body surface or internal discretization and the hybrid method. Sparse matrix can be achieved by using differential equation method, and the field propagation is discrete described in space, which would result in the space dispersion error. Additionally, this kind of methods require initial boundary conditions. Integral equation method analyses the scattering problem by solving the scattering body surface or volume of the induced current, there is no space dispersion error. Differential equation method is often easier to implement than the integral

Manuscript received 4 September 2015. Accepted for publication 25 December 2015.

The research work was supported by National Natural Science Foundation of China under Grant No. 61379001 and Key Project of Beihang University under Grant No. 201412 (“Exploration and Practice of Innovation Ability Cultivation in Mathematical Education”).

Hongyi Li is with the LMIB, School of Mathematics and Systems Science, Beihang University, Beijing 100191, China (e-mail: Hongyili_buaa@163.com).

Di Zhao is with the LMIB, School of Mathematics and Systems Science, Beihang University, Beijing 100191, China .

Shaofeng Xu is with the School of Software, Beihang University, .

Pidong Wang is with the School of Reliability and Systems Engineering, Beihang University, Beijing 100191, China.

Jiaxin Chen is with the School of Computer Science and Engineering, Beihang University, Beijing 100191, China.

equation method. For uniform background medium open domain problem, we often use integral equation method to solve. For problems that use single integral equation method or differential equation method that are difficult to solve, we often analyse by using hybrid method. Common integral equation method includes method of moment (MOM), volume integral equation method (VIEM). Existing methods of differential equations include finite difference time domain method (FDFD), finite element method (FEM), the domain decomposition method (DDM), etc.

This paper focuses on the clustering applications in EMC analysis, on which topic there are few existing works for electromagnetic signals, to the best of our knowledge.

Commonly used clustering algorithms are K-means, KNN (K-Nearest Neighbour) and FCM (Fuzzy C-Means), they all can be directly used for EMC analysis. However, they have some disadvantages as follows:

K-means algorithm is not suitable for a large class cluster found in the non-convex shape or a big difference size between the clusters. In signal clustering, the number of different types of signals can vary widely, so the effect of K-means algorithm will be affected.

KNN algorithm has a major drawback, that is, its computation consuming is rather large, since in classification, the distance between any data pair needs to be calculated to obtain its K nearest neighbour points. [2] While, the EMC signals are always with high dimensional, KNN is not suitable for clustering on EMC signals.

FCM algorithm itself has two fatal weaknesses: Firstly, fuzzy clustering objective function is a non-convex function, there are a lot of local extreme points, where improper initialization will lead to convergence to the local extreme value point and get the optimal fuzzy partition of a data set; Secondly, large amount of data takes algorithm seriously, restrict its practical application.

In this paper, for multiple sets of EMI signals, we use a self-organizing feature map (SOM) for clustering. The topology structure of SOM algorithm is simple, and its self-stability and clustering results can be visualized. Meanwhile, the two-dimensional plan after SOM Fabric class also reflect the relevance of different types of signals.

Before using SOM neural network clustering, it is necessary to adopt some dimension reduction method of the signal of the high-dimensional data into low-dimensional that can cluster the data, which is also discussed in this paper.

The remaining part of the organizational structure of this paper is organized as follows: Section 2 describes the basic principles of SOM neural network, Section 3 describes the SOM neural network applications in high-dimensional signal processing, and Section 4 demonstrates the experimental results and analysis to verify the performance of the proposed method.

II. SIGNAL DIMENSION REDUCTION TECHNIQUES

A. High-dimensional clustering research background

Clustering is an important data analysis tool, which in accordance with certain requirements and rules for data set to distinguish and classify data objects, which then make a no category labelled data set divided into several subsets (classes) in accordance with certain criteria. Similar data objects are classified as a class, and dissimilar data objects are classified as different classes. Cluster analysis can effectively find the data distribution which is implicit in the data set, so as to lay a good foundation for further full and effective use of data. Meanwhile, with the rapid development of information technology, clustering is not only facing the problem of increasing amount of data, but also encounter with the high-dimensional problem.

In applications that high-dimensional data related to, the curse of dimensionality is a very common phenomenon. The term was first proposed by Bellman, it refers to a series of problems due to the excessive variables (properties) encountered in the data analysis. Since then, many researchers have done a lot of research dedicated to reduce or even eliminate the impact of the disaster on the dimension of high-dimensional data processing [3, 4].

B. Two dimension reduction techniques

When clustering high-dimensional data sets, traditional clustering method mainly encounter two problems. First, there are a lot of unrelated attributes in high-dimensional data set, which makes the possibility of clusters in all the dimensions almost zero. Second, data distribution in high-dimensional data space is sparser than in lower-dimensional space, distance between the data is almost equal is generally phenomenon. Moreover, since traditional clustering methods are based on distance, it is then unable to build clusters based on the distance in high-dimensional space.

There are generally two ways to solve the problem above:

1) *Feature Transform* [5, 6]: This kind of methods includes many traditional methods, including PCA [7] and SVD [8]. They transform the original data set to a k-dimensional new space by linear combination, making such a class of traditional clustering algorithm can be effective in this new data space, and finally achieve the purpose of reducing the dimension. But the disadvantage of this approach has three points: k is difficult to be determined; there are a lot of unrelated categories in high-dimensional space and it brings difficulties to clustering; it's prone to produce meaningless clusters. [9]

2) *Feature Selection*: Different from feature transform, feature selection performs mining tasks only on those relevant subspaces. Therefore, it is more efficient than the feature conversion to reduce dimensions. Feature selection generally uses greedy strategies to search different feature subspace, and then use some criteria to evaluate these subspaces, in

order to find the desired clusters.

And we are using the second method - feature selection for dimension reduction of high-dimensional signal, enabling clustering in low-dimensional space.

III. THE BASIC PRINCIPLE OF SOM NEURAL NETWORK

SOM clustering algorithm was first put forward by Finn Kohonen in 1982 [10], it is a kind of unsupervised training of neural network [11], and the self-organizing process in fact is unsupervised, which automatically clusters input patterns without label information.

SOM consists of the input layer and competition layer (output layer). The number of input layer neurons is N , the competitive layer is one-dimensional or two-dimensional planar array consisting of m neurons, which can also be seen as a three-dimensional cubic lattice. The network is fully connected.

IV. A HIGH-DIMENSIONAL SIGNALS CLUSTERING METHOD BASED ON SOM

In the previous section, we introduced signal dimension reduction techniques and SOM theory. Now we propose a high dimensional electromagnetic interference signal clustering method based on SOM neural network, and then find out the global features of different interference factors, in order to finally provide precise mathematical simulation models for EMC design, analysis, forecasting and evaluation technology.

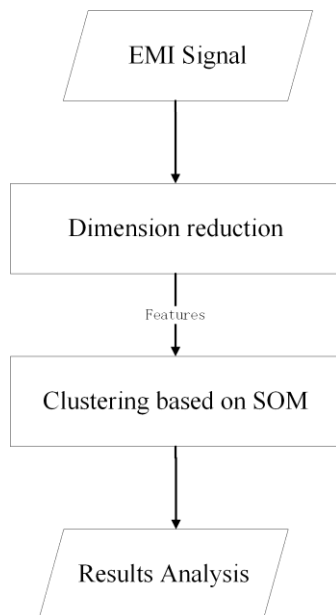


Fig. 1 Flow chart of the proposed method

As the above chart shows, our method mainly consists of the following three steps.

A. Signal dimension reduction

Based on the spectrum features of the signal, we choose the following five features instead of the original signal high dimensional information: number of crest, number of trough, expectation, variance and bandwidth.

The mathematical definitions of features are defined as follows:

Crest: for each sampling point X , if the function value of this sampling point is greater than the left sample point (if any) and the right sample point (if any), then that point is defined as a crest.

Trough: for each sampling point X , if the function value of this sampling point is smaller than the left sample point (if any) and the right sample point (if any), then that point is defined as a trough.

Expectation: the mean of all sampling points

Variance: the mean of all the square of difference between the actual values and expectations.

Bandwidth: for every 10 sampling points, calculate the mean of crest and trough, meantime subtraction, and then averaged.

B. Clustering based on SOM

Through the choice of above features, we can turn thousands of dimension of signal data of each group into five dimension data of each group, this greatly facilitate the use of SOM neural network clustering. [12]

V. RESULTS AND DISCUSSION

In order to test the performance of the proposed method, we choose 158 groups of frequency domain EMI signal data. EMI signals in this dataset are high-dimensional (with thousands of dimension), and the frequency domain information can help us explore more general features from the signals and get better clustering results.

In this experiment, the signals in the dataset can be reconstructed with the five selected features proposed above and then they are processed as the input of the SOM neural network.

After a SOM network clustering, the 158 groups of signal clustering results are as follows:

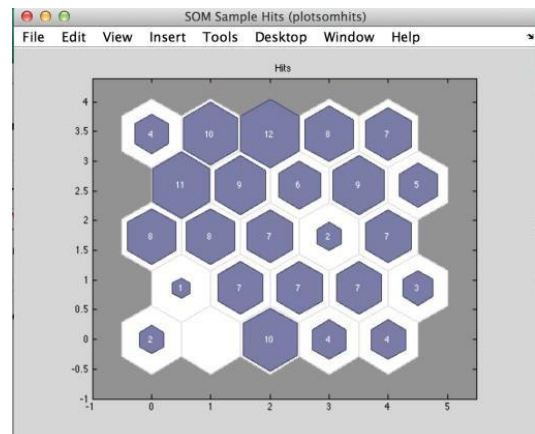


Fig. 2 SOM neural network clustering results

The number of the above represent sets of data gathered in this class, the adjacent hexagons shows some features of this two category are similar.

Fig. 3-Fig. 6 show parts of the clustering results.

Through the comparison, we found that the effect of whole SOM neural network for the 5-d eigenvalue is more satisfactory. From Fig. 3 to Fig. 6, it can be seen that signal spectrum are similar in the same class (as shown in Fig. 3 and Fig. 4), the spectrum between two classes have some similar features. Fig. 5 shows that different signal frequency spectrum features are big different in this kind of class. It indicates two aspects, one is the selected five eigenvalues for dimension reduction are not accurate enough, they cannot on behalf of the entire signal features; the other is SOM neural network still has optimize space, by adjusting the node number of competitive layer, changing the final clustering number, through the experiment to find the most suitable clustering number, can also help accurate clustering.

To illustrate the effect of SOM neural network clustering, we use the K-means clustering method on source data again, the results are partly shown as Fig. 7 - Fig. 8.

Through the above part of the clustering results we can see that, K-means clustering method although can group similar signal together, but compared with the SOM clustering, two small classes distinct signal are easy to cluster into a broad class, for example, in Fig. 7, the middle line of three signal and other signal features are big different in the graph; In Fig. 8, the features of the last two signals and other signals are big different also. It shows that performance of K-means clustering method is poor compared to SOM neural network.

Generally speaking, since EMI signals are high-dimensional and non-linear, it is thus computationally cost and difficult to directly conduct clustering. However, by using the proposed low dimensional features representation of EMI signals, SOM can treat the five features as normal input to cluster and yield significantly better performance.

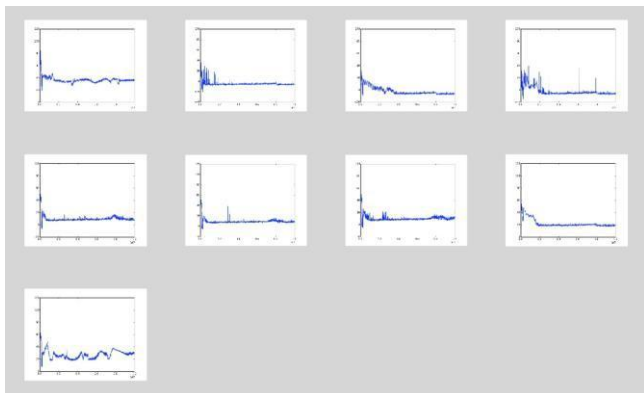


Fig. 3 Class 8

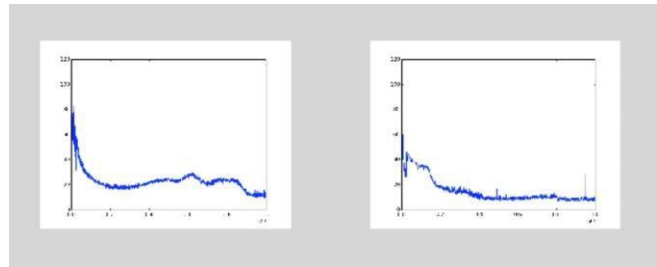


Fig. 4 Class 9

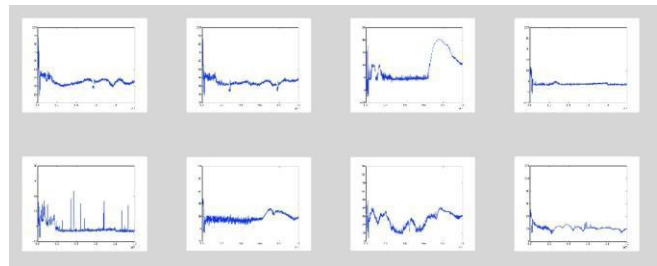


Fig. 5 Class 12

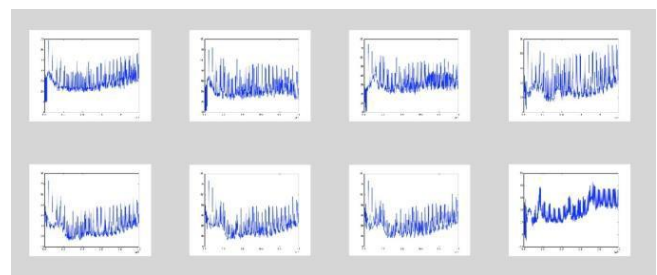


Fig. 6 Class 25

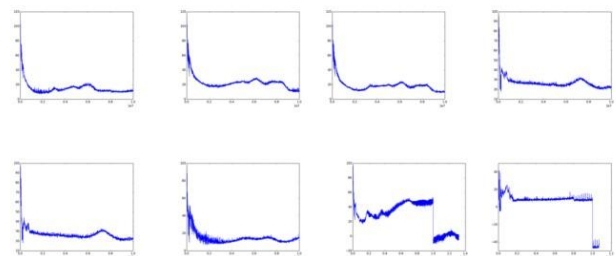


Fig. 7 Class 1

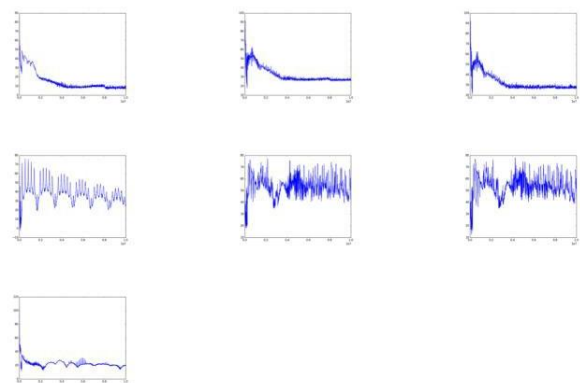


Fig. 8 Class 4

VI. CONCLUSIONS

In this paper, through the clustering of EMI signal, we have studied the global representation of EMI, and provided research methods for EMC mathematical model building. Meanwhile, to deal with the high dimensionality of EMI signals, we have introduced the dimension reduction approaches, which could further improve the clustering effect of EMI signals.

REFERENCES

- [1] R. Kohavi, G. John, Wrappers for feature subset selection. *Artificial Intelligence*, (1–2), pp. 273–324, 1997.
- [2] D. Zhao, Y. Fu, C. Wang and H. Li, A novel algorithm for classifying measuring curves based on interval estimation. *Advanced Materials Research*, 734–737, pp. 3061–3064, 2013.
- [3] T. Kohonen, The self-organizing map. *Proceedings of the IEEE*, 78(9), pp. 1464–1480, 1990.
- [4] L. Ertöz, M. Steinbach, V. Kumar, Finding clusters of different sizes, shapes, and densities in noisy, high dimensional data. *SDM*, pp. 47–58, 2003.
- [5] J. H. Ham, D. D. Lee, L. K. Saul, Learning high dimensional correspondences from low dimensional manifolds. *Proc. of ICML Workshop on the Continuum from Labeled to Unlabeled Data in Machine Learning and Data Mining*, pp. 34–41, 2003.
- [6] C. Ding , et al, Adaptive dimension reduction for clustering high dimensional data. *Proc. of the Second IEEE International Conference on Data Mining*, pp. 147–154, 2002.
- [7] C. Farhat, J. Mandel, F. X. Roux, Optimal convergence properties of the FETI domain decomposition method. *Computer methods in applied mechanics and engineering*, 115(3), pp. 365–385, 1994.
- [8] S. Wold, K. Esbensen, P. Geladi, Principal component analysis. *Chemometrics and intelligent laboratory systems*, 2(1), pp. 37–52, 1987.
- [9] H. Li, M. Ye and D. Zhao, An improved ICA algorithm based on the negative entropy and simulated annealing algorithm. *Applied Mechanics and Materials*, 411–414, pp. 1125–1128, 2013.
- [10] J. C. Bezdek, R. Ehrlich, W. Full, FCM: The fuzzy c-means clustering algorithm. *Computers & Geosciences*, 10(2), pp. 191–203, 1984.
- [11] H. Li, X. Wu, T. Wang and D. Zhao, A simulation and prediction method of the height of wheat based on BP neural networks and the ant colony algorithm. *Advanced Materials Research*, 659, pp. 113–117, 2013.
- [12] D. Zhao, H.F. Liu and H.Y. Li, A Method Based on Grey Correlation Clustering for Improving the Hierarchy of Analytic Hierarchy Process. *Proc. IEEE/WIC/ACM International Conference on WI-IAT*, 3, pp. 156-159, 2010.

Active Comb Filter Using Voltage Differencing Transconductance Amplifiers

Dinesh Prasad, Akshat Jain, Pankaj Dhingra and Aditya Panchal

Abstract— A new active comb filter employing Voltage Differencing Transconductance Amplifiers (VDTAs) is proposed to eliminate the selected frequencies of different signals. The proposed filter is based on VDTAs, capacitors and resistors. The functionality of the circuit is verified using PSPICE with TSMC CMOS 0.18 μ m process parameters for test signals of 50, 150, 250, and 350 Hz.

Index Terms— Active Comb Filter, Voltage differencing transconductance amplifier, Analog signal processing.

Original Research Paper
DOI: 10.7251/ELS1620032P

I. INTRODUCTION

THE field of biomedical signal analysis or processing has advanced to the stage of practical application of signal processing and pattern analysis techniques for efficient and improved noninvasive diagnosis and online monitoring of critical patients. Filtering of power line interference is very meaningful in the measurement of biomedical events recording, particularly in the case of recording signals as weak as the ECG (clinical tool for investigating the activities of heart). The most common are power line interference and baseline drift [1]. The fundamental frequency of this interference is usually 50 Hz or 60 Hz, depending on the local power-line frequency and often has heavy harmonic content above 50–60 Hz [2-5]. Power line interference around transformers is caused by stray magnetic fields causing the enclosure and accessories to vibrate. A phenomenon called “Magnetostriction” is also a source of vibration, where the core iron changes direction rapidly when magnetic field is applied. The intensity of the vibrations is a

Manuscript received 13 April 2015. Received in revised form 09 April 2016. Accepted for publication 17 June 2016.

This work was performed at the Advanced Analog Signal Processing Lab, Department of Electronics and Communication Engineering, Faculty of Engineering and Technology, Jamia Millia Islamia, New Delhi-110025, India.

Dinesh Prasad is with the Faculty of Engineering & Technology, Jamia Millia Islamia, New Delhi, India (phone: +91-11-26981284, e-mail: dprasad@jmi.ac.in)

Akshat Jain is with the Faculty of Engineering & Technology, Jamia Millia Islamia, New Delhi, India (phone: +91-11-26981284, e-mail: akshatjain119@gmail.com)

Pankaj Dhingra is with the Faculty of Engineering & Technology, Jamia Millia Islamia, New Delhi, India (phone: +91-11-26981284, e-mail: pankajdh.jmi@gmail.com)

Aditya Panchal is with the Faculty of Engineering & Technology, Jamia Millia Islamia, New Delhi, India (phone: +91-11-26981284)

function of the applied voltage. Hence physiological signal gets distorted by power line frequency and its harmonics.

Recently, the VDTA is a widely used active device for analog signal processing. In reference [6] the authors presented a CMOS structure of VDTA and its RF filter. There are many other applications of VDTA is reported in references [7-8] and references cited therein.

In this paper, a new design of active comb filter has been proposed consisting of VDTAs and few passive components to remove the harmonic interferences present in the various signals and functionality of the circuit is verified using PSPICE for test signals of 50, 150, 250, and 350 Hz.

II. CIRCUIT DESCRIPTION

A 2nd order passive band reject filter is shown in Fig. 1. It consists of a series combination of R, L and C where the output is taken across the series combination of L and C.

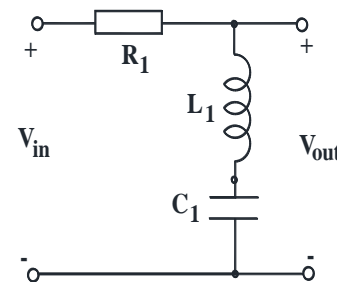


Fig. 1: RLC circuit of notch filter

The analysis of Figure 1 results in a voltage transfer function $H(s)$ as:

$$\frac{V_o}{V_{in}} = \frac{s^2 + \frac{1}{LC}}{s^2 + s\left(\frac{R}{L}\right) + \frac{1}{LC}} \quad (1)$$

The parameters from the above transfer function are obtained as

$$\omega_0 = \sqrt{\frac{1}{LC}} \quad (2)$$

$$Q_0 = \frac{1}{R} \sqrt{\frac{L}{C}} \quad (3)$$

$$BW = \frac{R}{L} \quad (4)$$

Where,

W_0 is notch frequency of the filter.
 Q_0 is quality factor of the filter.
 BW is the bandwidth of the filter.

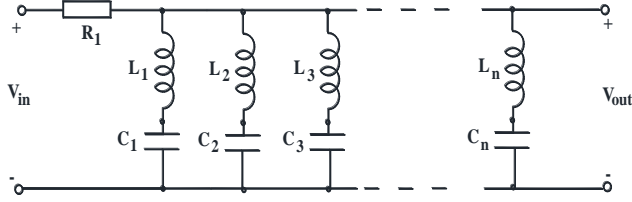


Fig. 2 Comb Filter using a basic RLC circuit

The extension of L - C section of circuit in Fig. 1 gives a comb filter as shown in Fig. 2. It can eliminate n -number of harmonics of the power line interference, which distort the input signal $V_{in}(t)$.

By applying the circuit analysis technique in Fig. 2, we obtain the voltage transfer function of the active comb filter as:

$$H^k(s) = \frac{1}{\left(\frac{sC_k R}{s^2 L_k C_k + 1} + 1 \right)} \quad (5)$$

where the K^{th} notch filter is used to eliminate the K^{th} harmonic component from the input signal.

A. Proposed active comb filter

It is known that it is difficult to implement inductance in integrated circuits. Hence to overcome the above problem, the proposed comb filter is implemented using VDTAs. The notch filter is taken from the published paper [8]. When a series of notch filters using VDTAs are cascaded; there is a drastic reduction in the number of active components as compared to reference [9] as it uses 10 OTAs while our design uses just 4 VDTAs.

The symbolic notation of VDTA is shown in Figure 3.

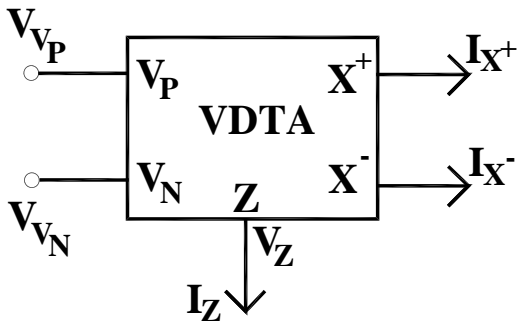


Fig. 3 Symbolic notation of VDTA

An ideal VDTA is characterized by following set of equations:

$$\begin{bmatrix} i_z \\ i_{x+} \\ i_{x-} \end{bmatrix} = \begin{bmatrix} g_{m1} & -g_{m1} & 0 \\ 0 & 0 & g_{m2} \\ 0 & 0 & -g_{m2} \end{bmatrix} \begin{bmatrix} V_p \\ V_n \\ V_z \end{bmatrix} \quad (6)$$

Where g_{m1} and g_{m2} are the transconductances of the VDTA.

The circuit of the notch filter using VDTA and passive component is shown in Figure 4[7]. Hence, Q_0 , and bandwidth (BW) can be adjusted electronically by using bias current of VDTAs. The proposed active comb filter using VDTAs which can eliminate four undesired frequencies is shown in Fig. 6. The expressions of the characteristic parameters of n^{th} notch filter are:

$$Q_n = \sqrt{\frac{g_{mn1} g_{mn2} C_n^2 R_n^2}{C_{n1} C_{n2}}} \quad (7)$$

$$\omega_n = \sqrt{\frac{g_{mn1} g_{mn2}}{C_{n1} C_{n2}}} \quad (8)$$

$$BW_n = \frac{1}{R_n C_n} \quad (9)$$

Where,

Q_n is the quality factor of the n^{th} notch filter.

W_n is the notch frequency of n^{th} notch filter.

BW_n is the bandwidth of the n^{th} notch filter.

It can be seen that once the values of C_{n1} , C_{n2} and R_n are fixed as per requirement, the notch frequencies can still be adjusted by varying G_{mn1} and G_{mn2} by changing bias currents of n^{th} VDTA.

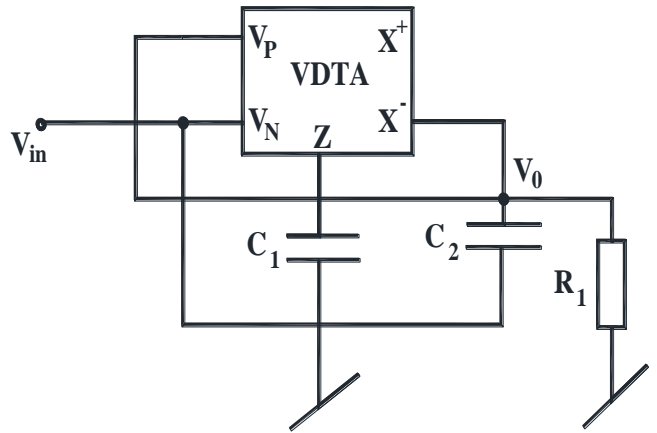


Fig. 4: Notch Filter using VDTA [8]

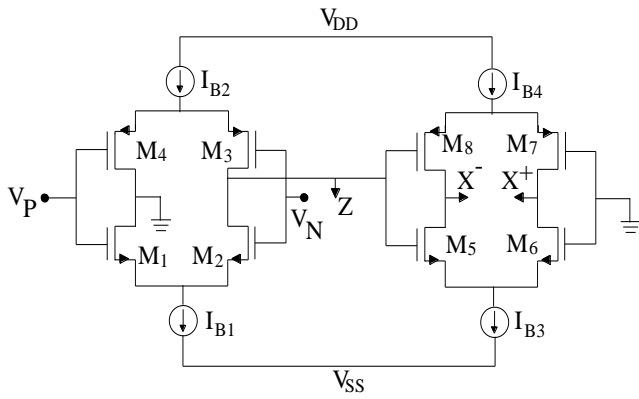


Fig. 5: CMOS implementation of VDTA [6]

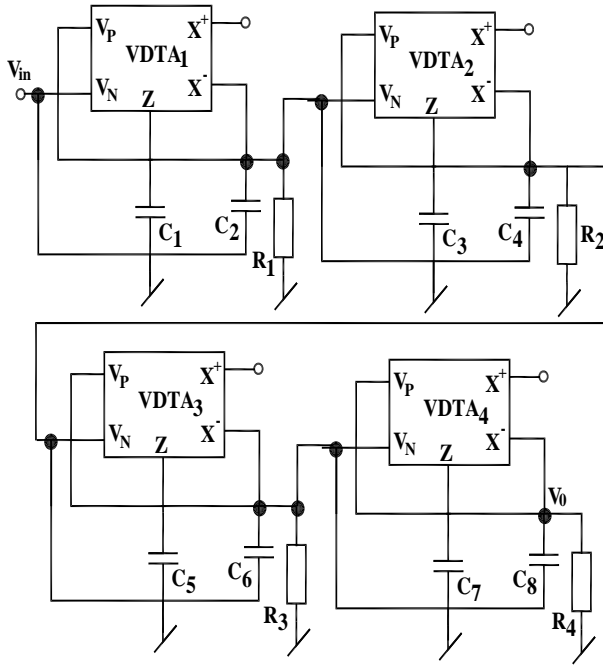


Fig. 6 Active comb filter using four VDTAs

III. SIMULATION AND RESULTS

The VDTA has been simulated using PSPICE in CMOS Technology [6]. The internal structure of VDTA using TSMC CMOS technology is shown in Figure 5. The supply voltages used for simulation are $V_{dd} = 0.9V$ and $V_{ss} = -0.9V$. The proposed comb filter is designed using four VDTAs so that it can remove four unwanted frequencies (harmonic frequencies). In power line interferences, odd harmonics interference plays an important role. So, in this paper, odd harmonics have been removed, that is first VDTA removes the fundamental frequency of 50Hz, then second VDTA removes third harmonic of 150Hz, then third VDTA removes fifth harmonic of 250Hz, then fourth VDTA removes seventh harmonic of 350Hz.

The values of the passive components used are $C_1 = 466.184nF$, $C_2 = 233.092nF$, $R_1 = 70K$, $C_3 = 155.394nF$, $C_4 = 77.697nF$, $R_2 = 75K$, $C_5 = 93.225nF$, $C_6 = 46.612nF$, $R_3 = 150K$, $C_7 = 66.595nF$, $C_8 = 33.298nF$, $R_4 = 400K$. G_{m1} and G_{m2} of all the VDTAs are $103.5\mu A/V$ for $I_B = 10\mu A$.

The time response of the input signals having frequencies 50Hz, 150Hz, 250Hz, and 350Hz and their corresponding outputs are shown in Figures 7, 8, 9 and 10 respectively. It can be seen from the graphs that the amplitude of the output sinusoidal signals (shown in green color) which is around 100mV is very small as compared to sinusoidal input signals (shown in blue color) of 1V at the above odd harmonics which means that the above frequencies are being highly attenuated. The frequency response of the comb filter is shown in Figure 11. The simulation results justify the validity of the structure.

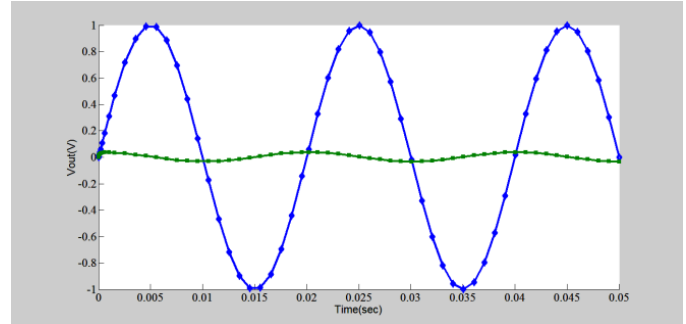


Fig. 7: Input and Output response at 50Hz

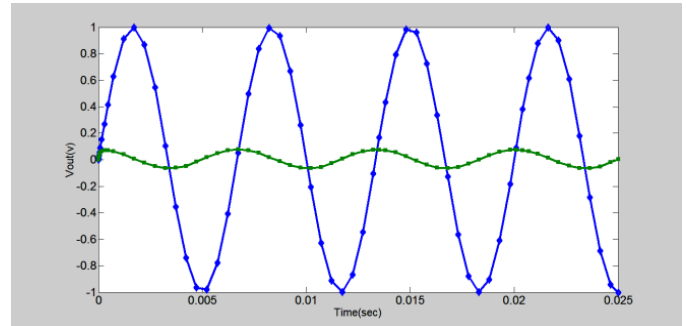


Fig. 8: Input and Output response at 150Hz

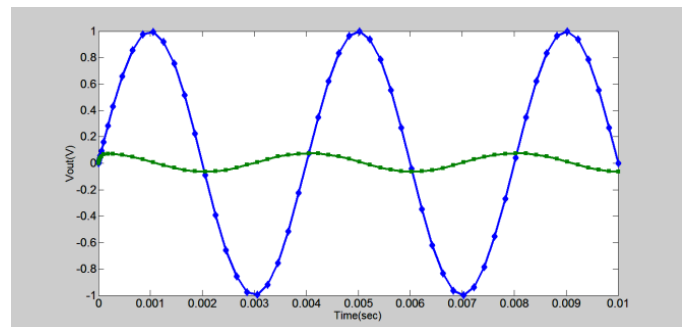


Fig. 9: Input and Output response at 250Hz

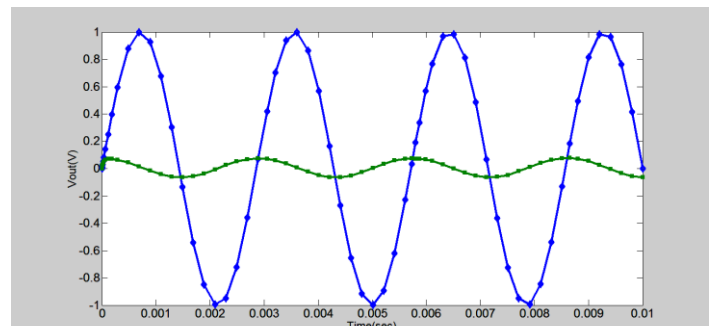


Fig. 10: Input and Output response at 350 Hz

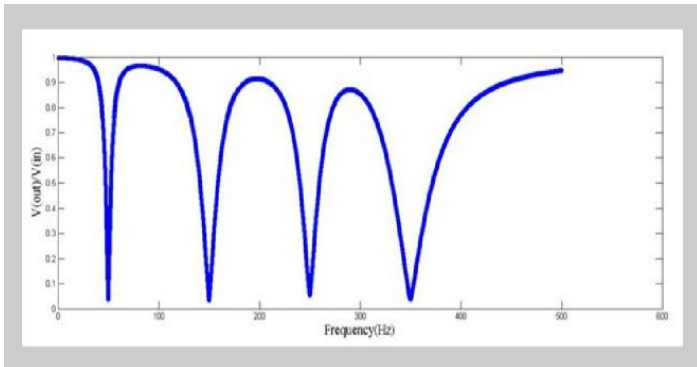


Fig. 11: Frequency response of active comb filter

IV. CONCLUSION

A new active comb filter employing voltage differencing transconductance amplifiers is proposed. The functionality of the circuit has been verified by using PSPICE with TSMC CMOS 0.18 μ m process parameters. The simulation graph of figure 11 has a comb like structure that is why it is called a comb filter. The simulated and theoretical results closely relate to each other.

REFERENCES

- [1] G. Kadam, P.C. Bhaskar, "Reduction of power line interference in ECG signal using fir Filter", *Int. J. of Comput. Engg. Rese.*, vol. 2, pp 315, 2012.
- [2] J. Piskorowski, "Power line interference removal from ECG signal using notch filter with non-zero initial conditions," in *Proceedings of the IEEE International Symposium on Medical Measurements and Application (MeMeA '12)*, pp. 1–3, University of Technology, Budapest, Hungary, May 2012.
- [3] S. M. M. Martens, M. M. Mischi, S. G. Oei, and J. W. M. Bergmans, "An improved adaptive power line interference canceller for electrocardiography," *IEEE Trans. on Biomedical Engineering*, vol. 53, no. 11, pp. 2220–2231, 2006.
- [4] T. W. Dawson, K. Caputa, M. A. Stuchly, and R. Kavet, "Pacemaker interference by 60-Hz contact currents," *IEEE Trans. on Biomedical Engineering*, vol. 49, no. 8, pp. 878–886, 2002.
- [5] C. T. Tsai, H.L. Chan, C. C. Tseng, and C.-P. Wu,, "Harmonic interference elimination by an active comb filter [ECG application]," in *Proc. of 16th Annual International Conf. of IEEE Engineering in Medicine and Biology Society*, vol. 2, pp.964–965, Baltimore, Md USA, November 1994.
- [6] A. Yesil, F. Kacar and H. Kuntman, "New Simple CMOS Realization of Voltage Differencing Transconductance Amplifier and Its RF Filter Application", *Radioengineering Journal*, vol. 20, No. 3, Sept., 2011.
- [7] D. Prasad and D. R. Bhaskar, "Electronically-Controllable Explicit Current Output Sinusoidal Oscillator Employing Single VDTA", *ISRN Electron.*, vol. 2012 (2012), article ID 382560, 5 pages.
- [8] D. Prasad, D. R. Bhaskar and Mayank Srivastava, "Universal voltage-Mode Biquad Filter Using a VDTA", *Indian Journal of Pure and Applied Physics*, vol. 51pp. 864-868, Dec. 2013.
- [9] R. K. Ranjan, S. P. Yalla, S. Sorya, and S. K. Paul, "Active Comb Filter Using Operational Transconductance Amplifier," *Active and Passive Electronic Components*, vol. 2014, pg- 4, 2014.

Low Voltage Mixed-mode Multi Phase Oscillator Using Single FDCCII

J. Mohan, B. Chaturvedi and S. Maheshwari

Abstract— In this paper a new low voltage mixed-mode multiphase quadrature oscillator employing a single fully differential second generation current conveyor, two resistors and two grounded capacitors is proposed. The proposed circuit provides two quadrature voltage outputs and three quadrature current outputs simultaneously. In addition, the proposed circuit has been made load insensitive so that it is capable of providing high output impedance current outputs without using additional current followers. Moreover, the proposed circuit of load insensitive quadrature oscillator provides four phase current outputs and two voltage outputs, simultaneously. Non ideal study is also included. Both the proposed circuits enjoy low active and passive sensitivities. This paper further presents an active-C multiphase oscillator with a single FDCCII and two grounded capacitors. The proposed structures are suitable for low voltage applications. Simulation results using PSPICE program on cadence tool are included.

Index Terms— Mixed-mode, FDCCII, Quadrature oscillator.

Original Research Paper
DOI: 10.7251/ELS1620036M

I. INTRODUCTION

QUADRATURE oscillators play an important role in the field of communication and instrumentation systems as they provide two or more sinusoids signals with 90° phase difference. Multi-phase oscillators are an inimitable case of quadrature oscillators. They are also used in many areas of electrical engineering, signal processing, and measurement. The realizations of quadrature oscillators using different variation of current conveyors have received significant attention due to their numerous advantages. Therefore, a number of voltage/current/mixed mode quadrature oscillators using current conveyor and its different variations have been

reported in the literature [1]–[19], [22]–[26]. However, these reported circuits suffer from the one or more limitations as follows

- Use of more than one active element [2]–[4], [6]–[8], [10], [12]–[18], [19], [22]–[24], [26].
- Excessive use of passive components [3], [4], [6], [8]–[10], [12], [14]–[18], [19], [25].
- Non-availability of three or four quadrature current outputs and two quadrature voltage outputs simultaneously [2]–[7], [9]–[11], [13]–[19], [24]–[26].

In this paper, a new low voltage mixed-mode multi-phase oscillator (MPO) circuit using single fully differential second generation current conveyor (FDCCII), two resistors and two grounded capacitors is presented. The proposed circuit offers two quadrature voltage outputs and three quadrature current outputs simultaneously. In addition, the proposed circuit is made to provide four phase load insensitive current outputs with two phase voltage outputs from the same configuration. Moreover, this paper explores another oscillator, namely the active-C MPO which also has the same features as the previous proposed structures with the added advantage of resistorless realization. A comparison study with existing relevant works has been given in Table I.

II. PROPOSED MIXED-MODE MULTI PHASE OSCILLATOR

In 2005, the fully differential second generation current conveyor (FDCCII) is reported to improve the dynamic range in mixed-mode applications where fully differential signal processing is required [20]. The CMOS implementation of FDCCII is shown in Fig. 1. Additional current output terminals ($-Z+$ and $-Z-$) can also be obtained by adding extra current mirrors at the $Z+$ and $Z-$ terminals respectively. The fully differential input voltages from the Y terminals are conveyed to the X terminals and the currents from the X terminals are conveyed to the Z terminals. Using standard notations, the terminals relationship of an ideal FDCCII can be characterized as

Manuscript received 13 January 2016. Received in revised form 16 June 2016. Accepted for publication 5 July 2016.

J. Mohan is with the Department of Electronics and Communication Engineering, Jaypee Institute of Information Technology, Noida-201304 (India).

B. Chaturvedi is with the Department of Electronics and Communication Engineering, Jaypee Institute of Information Technology, Noida-201304 (India) (phone: +91-120-24195866; e-mail: bhartendu.prof@gmail.com).

S. Maheshwari is with the Department of Electronics Engineering, Z. H. College of Engineering and Technology, Aligarh Muslim University, Aligarh-202002 (India).

TABLE I: COMPARISON WITH OTHER EXISTING RELEVANT WORKS

Refs.	Single Active Element Based Structure	Active Element Used	No. of Passive Components	No. of Available Current Outputs	No. of Available Voltage Outputs	Power Supply Used	Designed Frequency Of Oscillation	Technology Used
1	No	CC	4	0	2	-	-	-
2	No	OTA	3	0	2	NA	300KHz	NA
7	No	OTA	2	0	4	NA	10KHz	NA
9	No	DVCC	4/6	1	1	$\pm 2.5V$	1.127MHz	0.35 μm
10	No	CDTA	6	2	0	NA	1MHz	0.5 μm
11	Yes	FDCCII	5	2	3	NA	15.9KHz	NA
13	No	DDCC	5	0	2	$\pm 2.5V$	649KHz	0.5 μm
14	No	CCII	10	0	3	$\pm 10V$	50KHz	NA
16	No	DVCC	5	4	0	$\pm 2.5V$	1MHz	0.5 μm
17	No	OPA	5	0	4	NA	10KHz	NA
18	Yes	DO-CIBA	5/6	0	4	NA	1MHz	NA
22	No	CCCH	2	4	2	$\pm 2.5V$	140KHz	NA
23	No	DVCC	4	3	2	$\pm 2.5V$	4.15MHz	NA
24	No	DXCCII	4	0	2	$\pm 2.5V$	24.93MHz	0.5 μm
25	Yes	FDCCII	5	0	4	$\pm 3.3V$	15.9MHz	0.35 μm
26	No	FDCCII	4	0	3	$\pm 3V$	159KHz	0.35 μm
Proposed	Yes	FDCCII	4	4	2	$\pm 1V$	15.92MHz	0.18 μm

Abbreviations: CC: Current Conveyor, OTA: Operational Transconductance Amplifier, DVCC: Differential Voltage Current Conveyor, CDTA: Current Differencing Transconductance Amplifier, FDCCII: Fully Differential Second Generation Current Conveyor, DDCC: Differential Difference Current Conveyor, CCII: Second Generation Current Conveyor, OPA: Operational Amplifier, DO-CIBA: Differential Output Current Inverter Buffered Amplifier, CCCII: Current Controlled Second Generation Current Conveyor, DXCCII: Dual-X Second Generation Current Conveyor, NA: Not Available.

$$V_{X+} = V_{Y3} + V_{Y1} - V_{Y2}, \quad V_{X-} = V_{Y4} - V_{Y1} + V_{Y2} \quad (1)$$

$$I_{Z1+} = I_{Z2+} = I_{Z3+} = I_{X+}, \quad I_{-Z1+} = I_{-Z2+} = I_{-Z3+} = -I_{X+}, \\ I_{Z1-} = I_{X-}, \quad I_{-Z1-} = -I_{X-} \quad (2)$$

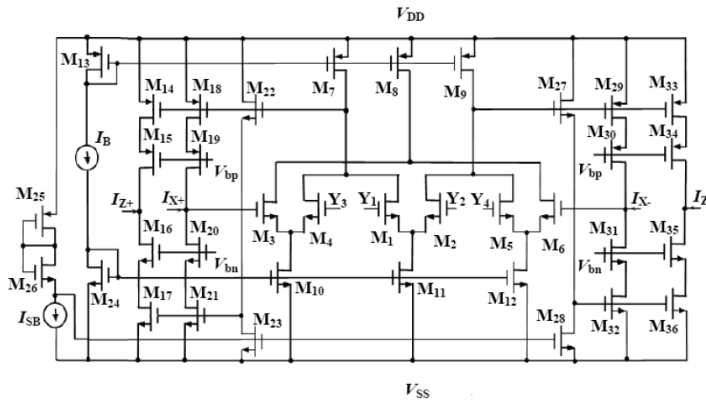


Fig. 1. The CMOS implementation of FDCCII [20]

The proposed mixed-mode MPO is shown in Fig. 2. The proposed circuit employs single FDCCII, two resistors and two grounded capacitors. The analysis of this circuit using (1) and (2) yields the following characteristic equation

$$s^2 + s \left(\frac{1}{R_2 C_1} - \frac{1}{R_1 C_1} \right) + \frac{1}{R_1 R_2 C_1 C_2} = 0 \quad (3)$$

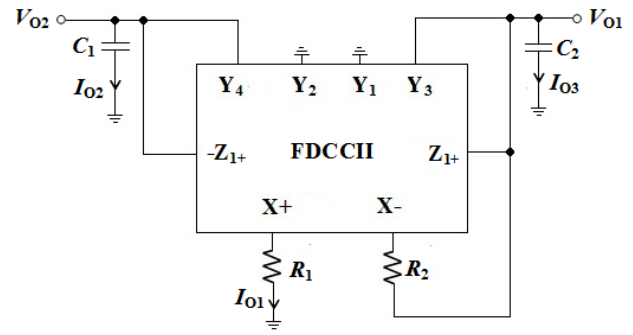


Fig. 2. Proposed low voltage mixed-mode MPO

The frequency of oscillation (FO) and the condition of oscillation (CO) can be obtained as:

$$FO: \omega_o = \left(\frac{1}{C_1 C_2 R_1 R_2} \right)^{\frac{1}{2}} \quad (4)$$

$$CO: R_1 \leq R_2 \quad (5)$$

The two quadrature voltage outputs (V_{O1} and V_{O2}) and three quadrature current outputs (I_{O1} , I_{O2} and I_{O3}) of the proposed circuit, depicted in Fig. 2, are related as

$$V_{O1} = -j\omega C_2 R_1 V_{O2} \quad (6)$$

$$I_{O3} = -j\omega C_1 R_1 I_{O2}, \quad I_{O1} = -I_{O2} \quad (7)$$

It is to be observed from (6) and (7) that the proposed circuit is capable to realize three quadrature current outputs (I_{O1} , I_{O2} and I_{O3}) and two quadrature voltage outputs (V_{O1} and V_{O2}), simultaneously.

Further, the proposed mixed-mode MPO shown in Fig. 2 is made load insensitive to provide high output impedance current outputs without using additional current followers by adding extra Z terminals as shown in Fig. 3.

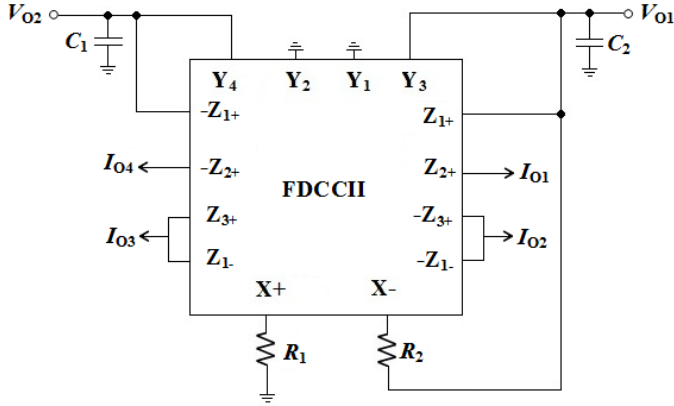


Fig. 3. Proposed Load Insensitive MPO

The proposed circuit of Fig. 3 now provides four load insensitive quadrature current outputs and two quadrature voltage outputs simultaneously. The four quadrature current outputs (I_{O1} , I_{O2} , I_{O3} and I_{O4}) and two quadrature voltage outputs (V_{O1} and V_{O2}) of the proposed circuit, depicted in Fig. 3, are now related as

$$I_{O3} = -j\omega C_1 R_1 I_{O2}, \quad I_{O1} = -I_{O2}, \quad I_{O3} = -I_{O4} \quad (8)$$

$$V_{O1} = -j\omega C_2 R_1 V_{O2} \quad (9)$$

III. NON-IDEAL STUDY

Taking the non-idealities of the FDCCII into account, the relationship of the voltages and currents can be rewritten as

$$V_{X+} = \beta_1 V_{Y1} - \beta_2 V_{Y2} + \beta_3 V_{Y3}, \quad V_{X-} = \beta_6 V_{Y4} - \beta_4 V_{Y1} + \beta_5 V_{Y2} \quad (10)$$

$$I_{Z1+} = \alpha_1 I_{X+}, \quad I_{-Z1+} = -\alpha_2 I_{X+}, \quad I_{Z1-} = \alpha_3 I_{X-}, \quad I_{-Z1-} = -\alpha_4 I_{X-} \quad (11)$$

The parameters $\beta_j(s)$ where, $j=1, 2, 3, 4, 5, 6$ and $\alpha_k(s)$ for $k=1, 2, 3, 4$ are the voltage and current transfer gains from Y terminals to X terminals. These transfer gains differ from unity by the voltage and current tracking errors of the FDCCII. More specifically, $\beta_j = (1-\varepsilon_j)$ and $\alpha_k = (1-\delta_k)$, where ε_j is the voltage tracking error of the FDCCII and δ_k is the current tracking error of the FDCCII. Note that the voltage

and current transfer gains ($\beta_j(s)$ and $\alpha_k(s)$) in the ideal case are equal to unity. The circuits of Fig. 2 and Fig. 3 are reanalyzed using (10) and (11). The modified characteristic equation is given as

$$s^2 + s \left(\frac{\alpha_2 \beta_1}{R_2 C_1} - \frac{\alpha_1 \beta_1}{R_1 C_1} \right) + \frac{\alpha_2 \alpha_3 \beta_1 \beta_2}{R_1 R_2 C_1 C_2} = 0 \quad (12)$$

The modified frequency of oscillation and the condition of oscillation can be obtained as:

$$\text{FO: } \omega_o = \left(\frac{\alpha_2 \alpha_3 \beta_1 \beta_2}{R_1 R_2 C_1 C_2} \right)^{\frac{1}{2}} \quad (13)$$

$$\text{CO: } R_1 \alpha_2 \leq R_2 \alpha_1 \quad (14)$$

The active and passive sensitivities with respect to ω_o are given as follows

$$S_{\alpha_2, \alpha_3, \beta_1, \beta_2}^{\omega_o} = -S_{R_1, R_2, C_1, C_2}^{\omega_o} = \frac{1}{2}, \quad S_{\alpha_1, \alpha_4, \beta_3, \beta_4}^{\omega_o} = 0 \quad (15)$$

Equation (15) shows that all the active and passive sensitivities with respect to ω_o are less than unity in magnitude.

IV. SIMULATION RESULTS

The performance of the proposed mixed-mode MPO is verified using PSPICE with 0.18 μm process CMOS parameters. The supply voltages and currents are $V_{DD} = -V_{SS} = 1\text{ V}$, $V_{bp} = V_{bn} = 0\text{ V}$, $I_B = 1.34\text{ mA}$ and $I_{SB} = 1.12\text{ mA}$. The proposed mixed-mode MPO circuit is designed using equal values of resistors and capacitors i.e $R_1 = R_2 = 1\text{ k}\Omega$, $C_1 = C_2 = 10\text{ pF}$. The theoretical frequency of oscillation is 15.92 MHz. The simulated frequency of oscillation is found to be 15.56 MHz which is close to the designed value. The simulated results for the three current outputs and two voltage outputs are shown in Fig. 4 and Fig. 5.

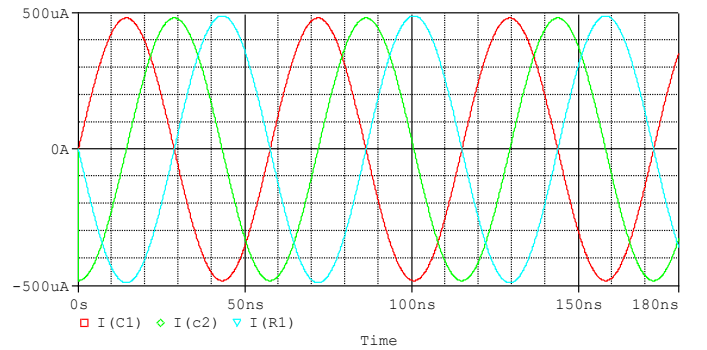


Fig. 4. Three quadrature current outputs at 15.92 MHz

The Fourier spectrum of the output waveforms of Fig. 4 and Fig. 5 are shown in Fig. 6 and Fig. 7, respectively.

Similarly, the load insensitive MPO circuit of Fig. 3 is designed for the same frequency of oscillation with the passive components values as $R_1 = R_2 = 1 \text{ k}\Omega$, $C_1 = C_2 = 10 \text{ pF}$.

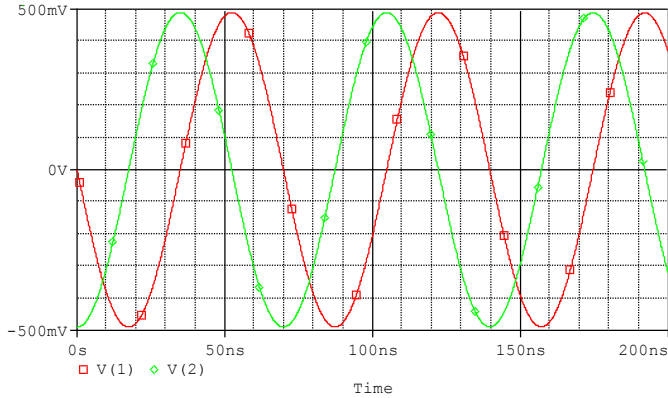


Fig. 5. Two quadrature voltage outputs at 15.92 MHz

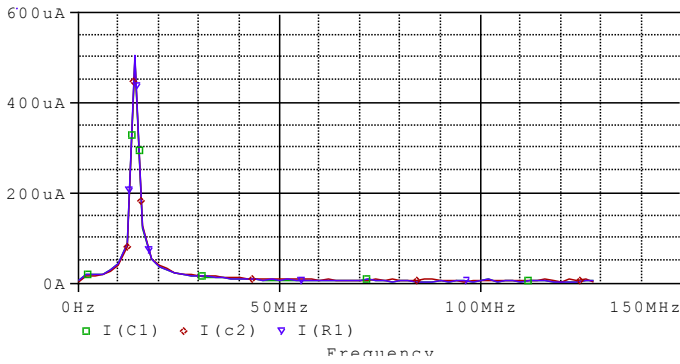


Fig. 6. Fourier spectrums of current outputs

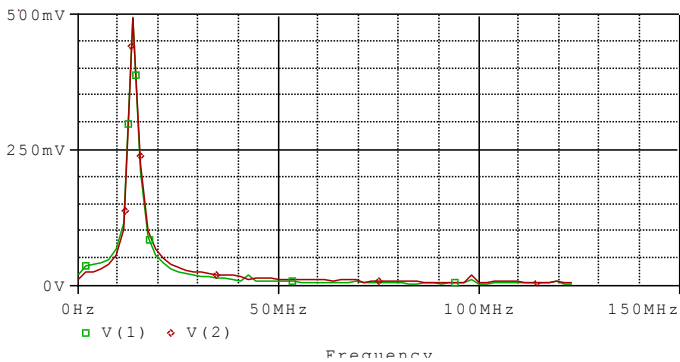


Fig. 7. Fourier spectrums of voltage outputs

The simulated four current output waveforms and two voltage output wave forms are shown in Fig. 8 and Fig. 9.

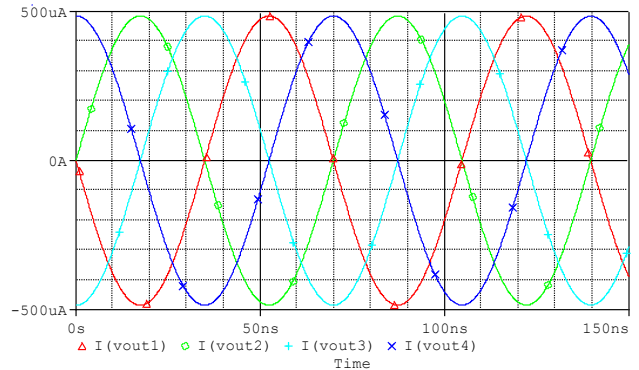


Fig. 8. Four quadrature current outputs at 15.92 MHz



Fig. 9. Two quadrature voltage outputs at 15.92 MHz

The Fourier spectrum of the output waveforms are shown in Fig. 10 and Fig. 11.

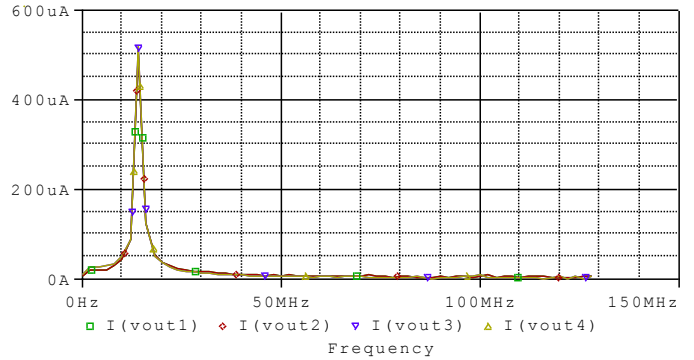


Fig. 10. Fourier spectrums of current outputs

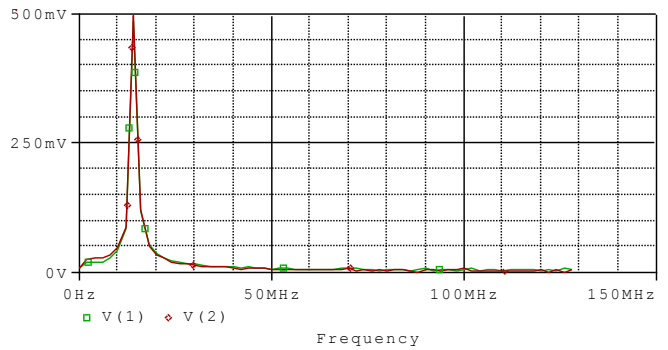


Fig. 11. Fourier spectrums of the voltage outputs

Moreover, the X-Y plots are also shown in Fig. 12 (a)-(e) to verify the quadrature relationships between four current outputs and two voltage outputs.

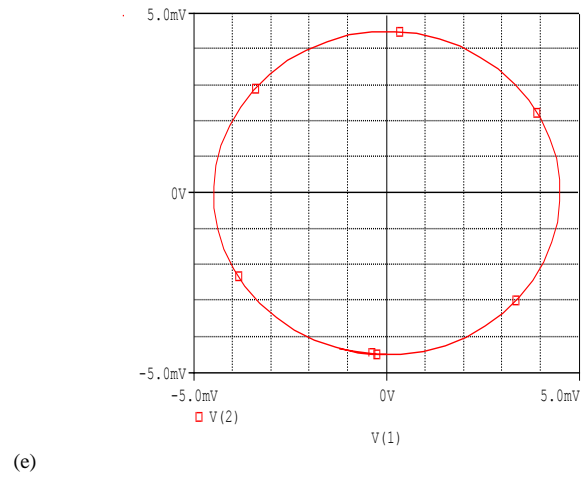
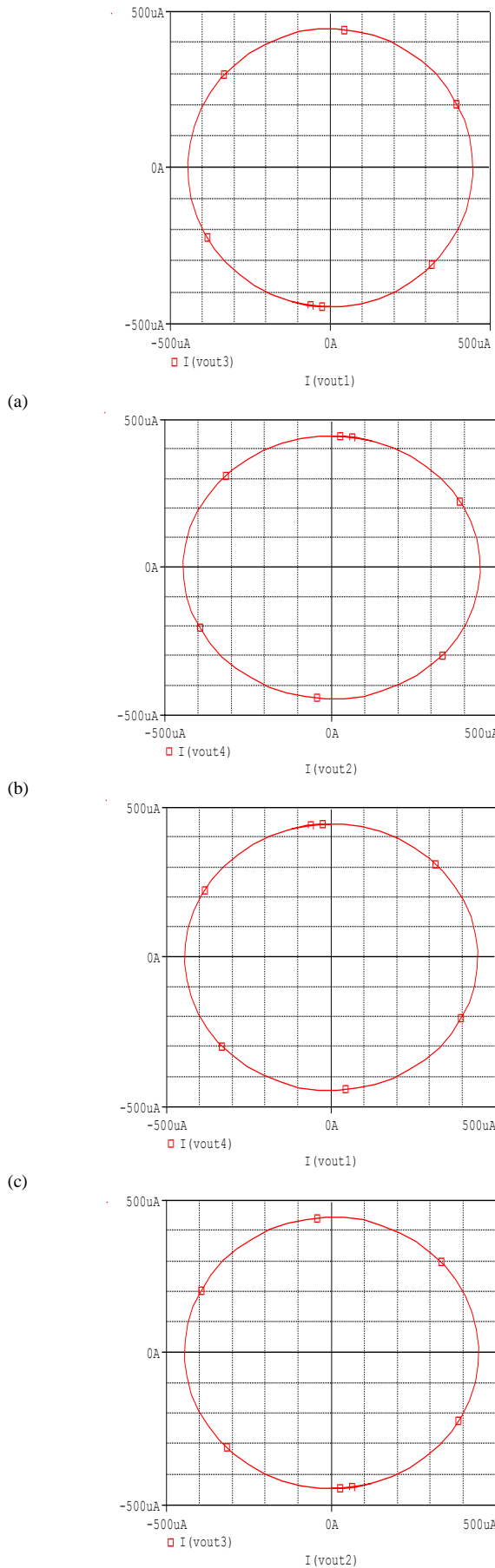


Fig. 12. The X-Y plots showing quadrature current and voltage relationships

V. ACTIVE-C MULTI PHASE OSCILLATOR

In this section, the proposed MPO of Fig. 3 is made resistorless by replacing the grounded resistor with the two n-MOS transistor based grounded resistor [21] and by replacing the floating resistor with the single n-MOS transistor biased in the triode region. The proposed active-C MPO is shown in Fig. 13.

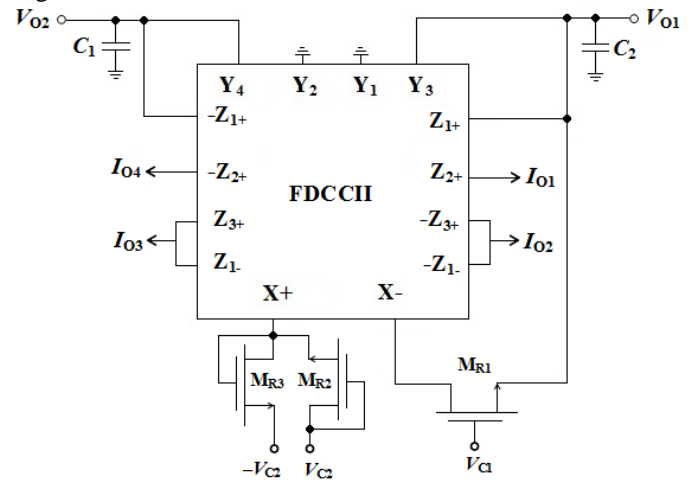


Fig. 13. Proposed active-C MPO

The frequency of oscillation and the condition of oscillation for the proposed active-C MPO can be given as

$$FO: \omega_o = \left(\frac{1}{C_1 C_2 R_{MOS1} R_{MOS2}} \right)^{\frac{1}{2}} \quad (16)$$

$$CO: R_{MOS1} \leq R_{MOS2} \quad (17)$$

where, R_{MOS1} is the equivalent resistance of the n-MOS transistors (M_{R2} and M_{R3}) in Fig. 13 and is given by

$$R_{MOS1} = \left[2\mu C_{OX} \left(\frac{W}{L} \right) (V_{C2} - V_T) \right]^{-1} \quad (18)$$

R_{MOS2} is the equivalent resistance of the n-MOS transistor (M_{R1}) in Fig. 13 and is given by

$$R_{MOS2} = \left[\mu C_{OX} \left(\frac{W}{L} \right) (V_{C1} - V_T) \right]^{-1} \quad (19)$$

where, μ , C_{OX} , V_T , W and L are the carrier mobility, gate capacitance per unit area, threshold voltage, channel width and the length of n-MOS.

The active-C MPO of Fig. 13 was simulated and designed for frequency 15.92MHz. The transistor aspect ratios for the MOS based electronic resistors are selected as $(W/L)_{MR1} = 28.8\mu\text{m}/0.18\mu\text{m}$, $(W/L)_{MR2} = (W/L)_{MR3} = 14.4\mu\text{m}/0.18\mu\text{m}$ and capacitors values are selected as $C_1 = C_2 = 10\text{pF}$. The frequency of oscillation for the proposed circuit is tuned to 15.92MHz by selecting the control voltages as $V_{C1} \cong V_{C2} = -V_{C2} = 0.91$. The four current and two voltage quadrature outputs are shown in Fig. 14 and Fig. 15, respectively.

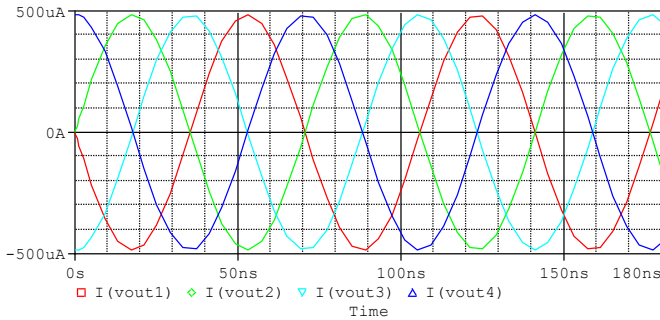


Fig. 14. Four quadrature current outputs at 15.92 MHz

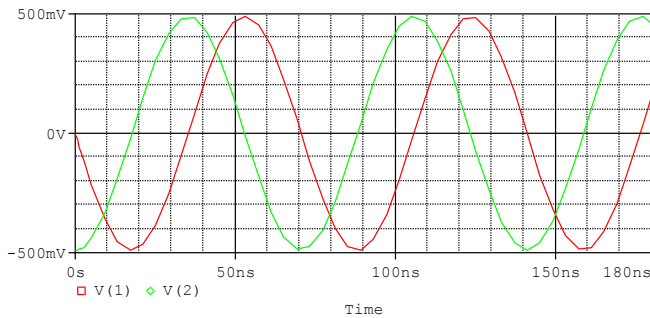


Fig. 15. Two quadrature voltage outputs at 15.92 MHz

The obtained results validate the active-C MPO realization. In order to further support the practical utility of active-C MPO, the control voltage ($V_{C1} \cong V_{C2} = V_C$) was varied so as to vary the FO. Fig. 16 shows the tuning of frequency of oscillation with the control voltages. Both theoretical and simulated FO is found to be close to each other.

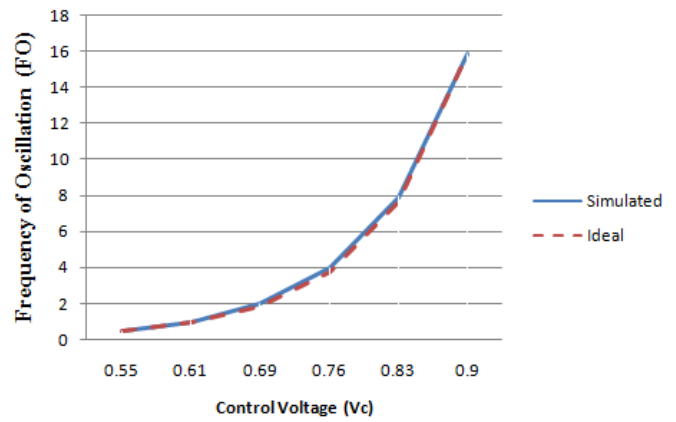


Fig. 16. Variation of FO with control voltage

VI. CONCLUSION

In this paper, a new single FDCCII based low voltage mixed-mode MPO realizing three quadrature current outputs and two quadrature voltage outputs has been proposed. The proposed circuit employs two resistors and two grounded capacitors. Moreover, a load insensitive MPO is also presented. The load insensitive circuit enjoys high impedance current outputs with no additional current followers. The active and passive sensitivities are not more than unity. By employing FDCCII, MOS based active resistors and two grounded capacitors, a new active-C MPO is also realized. All the proposed circuits are operated at low voltage power supply therefore suitable for low voltage applications. PSPICE simulation results on cadence tool have verified the workability of the circuits.

REFERENCES

- [1] A. M. Soliman, "Simple sinusoidal RC oscillators using current conveyors," *International Journal of Electronics*, vol. 42, pp. 309–311, 1975.
- [2] M. T. Ahmed, I. A. Khan, N. Minhaj, "On transconductance-C quadrature oscillators," *International Journal of Electronics*, vol. 83, pp. 201–207, 1997.
- [3] S. J. G. Gift, "Multiphase sinusoidal oscillator system using operational amplifiers," *International Journal of Electronics*, vol. 83, pp. 61–67, 1997.
- [4] M. T. Abuelma'atti, M. A. Alqahatani, "A new current controlled multiphase sinusoidal oscillator using translinear conveyors," *IEEE Transactions CAS-II*, vol. 45, pp. 881–885, 1998.
- [5] M. T. Abuelma'atti, M.A. Al-Qahtani, "Low component count second-generation current conveyor-based multiphase sinusoidal oscillators," *International Journal of Electronics*, vol. 84, pp. 45–52, 1998.
- [6] S. J. G. Gift, "The applications of all-pass filters in design of multiphase sinusoidal systems," *Microelectronics Journal*, vol. 31, pp. 9–13, 2000.
- [7] I. A. Khan, S. Khwaja, "An integrable gm-C quadrature oscillator," *International Journal of Electronics*, vol. 87, pp. 1353–1357, 2000.
- [8] S. Maheshwari, I. A. Khan, "Current controlled third order quadrature oscillator," *IEE Proceedings-Circuits, Devices and Systems*, vol. 152, pp. 605–607, 2005.
- [9] V. Kumar, A.U. Keskin, K. Pal, "DVCC based single element controlled oscillators using all grounded components and simultaneous current voltage mode outputs," *Frequenz*, vol. 59, pp. 7–8, 2005.
- [10] A. U. Keskin, D. Biolek, "Current mode quadrature oscillator using current differencing transconductance amplifiers (CDTA)," *IEE Proceedings-Circuits, Devices and Systems*, vol. 153, pp. 214–218, 2006.
- [11] J. Mohan S. Maheshwari, I. A. Khan, "Mixed mode quadrature oscillator using a single FDCCII," *Journal of Active and Passive Electronics Devices*, vol. 2, pp. 227–234, 2007.

- [12] S. Maheshwari, "Quadrature oscillator using grounded components with current and voltage outputs," *IET Circuits Devices and Systems*, vol. 3, pp. 153–160, 2009.
- [13] M. Kumngern, K. Dejhan, "DDCC based quadrature oscillators with grounded capacitors and resistors," *Active and Passive Electronics Component*, vol. 2009, Article ID 987304, 4 pages, 2009.
- [14] G. D. Skotis, C. Psychalinos, "Multiphase sinusoidal oscillators using second generation current conveyors," *AEU-International Journal of Electronics and Communications*, vol. 64, pp.1178-1181, 2010.
- [15] A. M. Soliman, "Two integrator loop quadrature oscillators: a review," *Journal of Advanced Research*, vol. 4, pp. 1–11, 2013.
- [16] S. Maheshwari, B. Chaturvedi, "High output impedance CMQOs using DVCCs and grounded components," *International Journal of Circuit Theory and Applications*, vol. 39, pp. 427–435, 2011.
- [17] T. Parveen, I. A. Khan, M. T. Ahmad, "Realization of four phase sinusoidal quadrature oscillator using operational amplifier", *Journal of Active and Passive Electronic Devices*, vol. 2, pp. 171–176, 2007.
- [18] V. Biolkova, J. Bajer, D. Biolek, "Four-phase oscillators employing two active elements," *Radioengineering*, vol. 20, pp. 334–339, 2011.
- [19] S. Maheshwari, "Voltage-mode four-phase sinusoidal generator and its useful extensions," *Active and Passive Electronic Components*, vol. 2013, Article ID 685939, 8 pages, 2013.
- [20] A. A. El-Adwy, A. M. Soliman, H. O. Elwan, "A novel fully differential current conveyor and applications for analog VLSI," *IEEE Transactions on Circuits and Systems-II: Analog and Signal Digital Processing*, vol. 47, pp. 306-313, 2000.
- [21] Z. Wang, "2-MOSFET transresistor with extremely low distortion for output reaching supply voltages," *Electronics Letters*, vol. 26, pp. 951-952, 1990.
- [22] S. Maheshwari, I. A. Khan, "Mixed mode quadrature oscillator using translinear conveyors and grounded components", *International Conference on Multimedia Signal Processing and Communication Technologies-2011*, pp. 153–155, 2011.
- [23] B. Chaturvedi, S. Maheshwari, "Second order mixed mode quadrature oscillator using dvccs and grounded components", *International Journal of Computer Applications*, vol. 58, pp. 42–45, 2012.
- [24] S. Maheshwari, B. Chaturvedi, "High-input low-output impedance all-pass filters using one active element", *IET Circuits, Devices and Systems*, vol. 6, pp. 103–110, 2012.
- [25] J. Mohan, S. Maheshwari, D. S. Chauhan, "Voltage mode cascadable all-pass sections using single active element and grounded passive components," *Circuits and Systems*, vol. 1, pp. 5-11, 2010.
- [26] S. Maheshwari, J. Mohan, D.S. Chauhan, "Voltage-mode cascadable all-pass sections with two grounded passive components and one active element," *IET Circuits Devices and Systems*, vol. 4, pp. 113–122, 2010.

Instructions for Authors

First A. Author, Second B. Author, and Third C. Author

Abstract—These instructions give you guidelines for preparing papers for ELECTRONICS journal. Use this document as a template if you are using Microsoft *Word* 6.0 or later. Otherwise, use this document as an instruction set. The electronic file of your paper will be formatted further. Define all symbols used in the abstract. Do not cite references in the abstract. Do not delete the blank line immediately above the abstract; it sets the footnote at the bottom of this column.

Index Terms—About four key words or phrases in alphabetical order, separated by commas.

I. INTRODUCTION

THIS document is a template for Microsoft *Word* versions 6.0 or later.

When you open the file, select “Page Layout” from the “View” menu in the menu bar (View | Page Layout), which allows you to see the footnotes. Then, type over sections of file or cut and paste from another document and use markup styles. The pull-down style menu is at the left of the Formatting Toolbar at the top of your *Word* window (for example, the style at this point in the document is “Text”). Highlight a section that you want to designate with a certain style, then select the appropriate name on the style menu. The style will adjust your fonts and line spacing. **Do not change the font sizes or line spacing to squeeze more text into a limited number of pages.** Use italics for emphasis; do not underline. The length of the manuscript is limited to the maximum of 15 pages.

To insert images in *Word*, position the cursor at the insertion point and either use Insert | Picture | From File or

copy the image to the Windows clipboard and then Edit | Paste Special | Picture (with “float over text” unchecked).

We will do the final formatting of your paper.

II. PROCEDURE FOR PAPER SUBMISSION

A. Review Stage

The manuscripts are to be delivered to the editor by e-mail: electronics@etfbl.net. Prepare it in two-column format as shown in this template. Place all figures and tables at the end of the paper (after the references) on separate page(s). Figures and tables must have the same caption names as referenced in the text. Only PDF format of the manuscript is allowed at the review stage. Please, check if all fonts are embedded and subset and that the quality of diagrams, illustrations, and graphics is satisfactory. Failing to provide above listed requirements is a valid reason for rejection.

B. Final Stage

When you submit your final version (after your paper has been accepted), prepare it in two-column format, including figures and tables in accordance with this template. Pack all of your files (manuscript source file in *Word*, figures, and manuscript PDF form) within one archive file (you may use any of the available file compression tools: *WinZip*, *WinRAR*, *7-Zip*, etc.). Do not forget to provide the manuscript converted in PDF format that will be used as a reference for final formatting of your paper. Figures should be named as referenced in the manuscript (e.g. *fig1.eps*, *fig2.tif*, etc.)

C. Figures and Tables

Format and save your graphic images using a suitable graphics processing program and adjusts the resolution settings. We accept images in the following formats: PS, EPS, TIFF, GIF, and PNG. Additionally, it is allowed to use images generated by using one of the following software tools: Microsoft Word, Microsoft PowerPoint, or Microsoft Excel. The resolution of a RGB color file should be 400 dpi. Please note that JPG and other lossy-compressed image formats are not allowed. Use available software tools to convert these images to appropriate format.

Image quality is very important to how yours graphics will reproduce. Even though we can accept graphics in many formats, we cannot improve your graphics if they are poor quality when we receive them. If your graphic looks low in quality on your printer or monitor, please keep in mind that cannot improve the quality after submission.

Manuscript received 15 September 2011 (write the date when you have first sent the manuscript for review). Received in revised form 20 October 2011 (write the date when you have sent the manuscript in its revised form if revisions required for your paper after review).

(Place here any sponsor and financial support acknowledgments).

F. A. Author is with the Faculty of Electrical Engineering, University of Banja Luka, Banja Luka, Bosnia and Herzegovina (corresponding author to provide phone: +387-51-222-333; fax: +387-51-111-222; e-mail: author@etfbl.net).

S. B. Author was with Faculty of Technical Sciences, University of Novi Sad, Novi Sad, Serbia. He is now with the Institute “Mihailo Pupin”, Belgrade, Serbia (e-mail: author@pupin.rs).

T. C. Author is with the School of Electrical Engineering, University of Belgrade, Belgrade, Serbia, on leave from the Faculty of Electronic Engineering, University of Niš, Niš, Serbia (e-mail: author@elfak.ni.ac.rs).

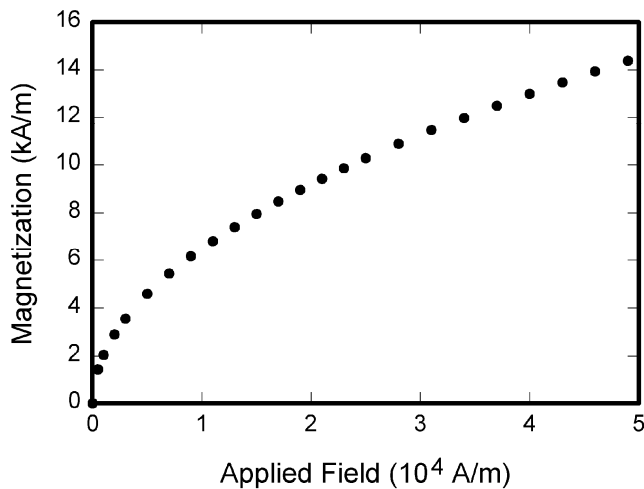


Fig. 1. Magnetization as a function of applied field. Note that “Fig.” is abbreviated. There is a period after the figure number, followed by two spaces. It is good practice to explain the significance of the figure in the caption.

If you are importing your graphics into this Word template, please use the following steps:

Under the option EDIT select PASTE SPECIAL. A dialog box will open, select paste picture, then click OK. Your figure should now be in the Word Document.

If you are preparing images in TIFF, EPS, or PS format, note the following. High-contrast line figures and tables should be prepared with 600 dpi resolution and saved with no compression, 1 bit per pixel (monochrome).

Photographs and grayscale figures should be prepared with 300 dpi resolution and saved with no compression, 8 bits per pixel (grayscale).

Most charts graphs and tables are one column wide (3 1/2 inches or 21 picas) or two-column width (7 1/16 inches, 43 picas wide). We recommend that you avoid sizing figures less than one column wide, as extreme enlargements may distort your images and result in poor reproduction. Therefore, it is better if the image is slightly larger, as a minor reduction in size should not have an adverse affect the quality of the image.

III. MATH

If you are using *Word*, use either the Microsoft Equation Editor or the *MathType* add-on (<http://www.mathtype.com>) for equations in your paper (Insert | Object | Create New | Microsoft Equation *or* MathType Equation). “Float over text” should *not* be selected.

IV. UNITS

Use either SI (MKS) or CGS as primary units. (SI units are strongly encouraged.) English units may be used as secondary units (in parentheses). **This applies to papers in data storage.** For example, write “15 Gb/cm² (100 Gb/in²).” An exception is when English units are used as identifiers in trade, such as “3½-in disk drive.” Avoid combining SI and

TABLE I
UNITS FOR MAGNETIC PROPERTIES

Symbol	Quantity	Conversion from Gaussian and CGS EMU to SI ^a
Φ	magnetic flux	1 Mx \rightarrow 10^{-8} Wb = 10^{-8} V·s
B	magnetic flux density, magnetic induction	1 G \rightarrow 10^{-4} T = 10^{-4} Wb/m ²
H	magnetic field strength	1 Oe \rightarrow $10^3/(4\pi)$ A/m
m	magnetic moment	1 erg/G = 1 emu \rightarrow 10^{-3} A·m ² = 10^{-3} J/T
M	magnetization	1 erg/(G·cm ³) = 1 emu/cm ³ \rightarrow 10^3 A/m
$4\pi M$	magnetization	1 G \rightarrow $10^3/(4\pi)$ A/m
σ	specific magnetization	1 erg/(G·g) = 1 emu/g \rightarrow 1 A·m ² /kg
j	magnetic dipole moment	1 erg/G = 1 emu \rightarrow $4\pi \times 10^{-10}$ Wb·m
J	magnetic polarization	1 erg/(G·cm ³) = 1 emu/cm ³ \rightarrow $4\pi \times 10^{-4}$ T
χ, κ	susceptibility	1 \rightarrow 4π
χ_ρ	mass susceptibility	1 cm ³ /g \rightarrow $4\pi \times 10^{-3}$ m ³ /kg
μ	permeability	1 \rightarrow $4\pi \times 10^{-7}$ H/m = $4\pi \times 10^{-7}$ Wb/(A·m)
μ_r	relative permeability	$\mu \rightarrow \mu_r$
w, W	energy density	1 erg/cm ³ \rightarrow 10^{-1} J/m ³
N, D	demagnetizing factor	1 \rightarrow $1/(4\pi)$

Vertical lines are optional in tables. Statements that serve as captions for the entire table do not need footnote letters.

^aGaussian units are the same as cgs emu for magnetostatics; Mx = maxwell, G = gauss, Oe = oersted; Wb = weber, V = volt, s = second, T = tesla, m = meter, A = ampere, J = joule, kg = kilogram, H = henry.

CGS units, such as current in amperes and magnetic field in oersteds. This often leads to confusion because equations do not balance dimensionally. If you must use mixed units, clearly state the units for each quantity in an equation.

The SI unit for magnetic field strength H is A/m. However, if you wish to use units of T, either refer to magnetic flux density B or magnetic field strength symbolized as $\mu_0 H$. Use the center dot to separate compound units, e.g., “A·m².”

V. HELPFUL HINTS

A. Figures and Tables

Because we will do the final formatting of your paper, you do not need to position figures and tables at the top and bottom of each column. In fact, all figures, figure captions, and tables can be at the end of the paper. Large figures and tables may span both columns. Place figure captions below the figures; place table titles above the tables. If your figure has two parts, include the labels “(a)” and “(b)” as part of the artwork. Please verify that the figures and tables you mention in the text actually exist. **Please do not include captions as part of the figures. Do not put captions in “text boxes” linked to the figures. Do not put borders around the outside of your figures.** Use the abbreviation “Fig.” even at the beginning of a sentence. Do not abbreviate “Table.” Tables are numbered with Roman numerals.

Color printing of figures is not available Do not use color unless it is necessary for the proper interpretation of your figures.

Figure axis labels are often a source of confusion. Use

words rather than symbols. As an example, write the quantity “Magnetization,” or “Magnetization M ,” not just “ M .” Put units in parentheses. Do not label axes only with units. As in Fig. 1, for example, write “Magnetization (A/m)” or “Magnetization ($A \cdot m^{-1}$),” not just “A/m.” Do not label axes with a ratio of quantities and units. For example, write “Temperature (K),” not “Temperature/K.”

Multipliers can be especially confusing. Write “Magnetization (kA/m)” or “Magnetization (10^3 A/m).” Do not write “Magnetization (A/m) \times 1000” because the reader would not know whether the top axis label in Fig. 1 meant 16000 A/m or 0.016 A/m. Figure labels should be legible, approximately 8 to 12 point type.

B. References

Number citations consecutively in square brackets [1]. The sentence punctuation follows the brackets [2]. Multiple references [2], [3] are each numbered with separate brackets [1]–[3]. When citing a section in a book, please give the relevant page numbers [2]. In sentences, refer simply to the reference number, as in [3]. Do not use “Ref. [3]” or “reference [3]” except at the beginning of a sentence: “Reference [3] shows” Please do not use automatic endnotes in *Word*, rather, type the reference list at the end of the paper using the “References” style.

Number footnotes separately in superscripts (Insert | Footnote).¹ Place the actual footnote at the bottom of the column in which it is cited; do not put footnotes in the reference list (endnotes). Use letters for table footnotes (see Table I).

Please note that the references at the end of this document are in the preferred referencing style. Give all authors’ names; do not use “*et al.*” unless there are six authors or more. Use a space after authors’ initials. Papers that have not been published should be cited as “unpublished” [4]. Papers that have been accepted for publication, but not yet specified for an issue should be cited as “to be published” [5]. Papers that have been submitted for publication should be cited as “submitted for publication” [6]. Please give affiliations and addresses for private communications [7].

Capitalize only the first word in a paper title, except for proper nouns and element symbols. For papers published in translation journals, please give the English citation first, followed by the original foreign-language citation [8]. All references **must be** written in Roman alphabet.

C. Abbreviations and Acronyms

Define abbreviations and acronyms the first time they are used in the text, even after they have already been defined in the abstract. Abbreviations such as IEEE, SI, ac, and dc do not have to be defined. Abbreviations that incorporate periods should not have spaces: write “C.N.R.S.,” not “C. N. R. S.” Do not use abbreviations in the title unless they are

¹It is recommended that footnotes be avoided (except for the unnumbered footnote with the receipt date and authors’ affiliations on the first page). Instead, try to integrate the footnote information into the text.

unavoidable (for example, “IEEE” in the title of this article).

D. Equations

Number equations consecutively with equation numbers in parentheses flush with the right margin, as in (1). First use the equation editor to create the equation. Then select the “Equation” markup style. Press the tab key and write the equation number in parentheses. To make your equations more compact, you may use the solidus (/), the exp function, or appropriate exponents. Use parentheses to avoid ambiguities in denominators. Punctuate equations when they are part of a sentence, as in

$$\int_0^{r_2} F(r, \varphi) dr d\varphi = [\sigma r_2 / (2\mu_0)] \cdot \int_0^\infty \exp(-\lambda |z_j - z_i|) \lambda^{-1} J_1(\lambda r_2) J_0(\lambda r_i) d\lambda. \quad (1)$$

Be sure that the symbols in your equation have been defined before the equation appears or immediately following. Italicize symbols (T might refer to temperature, but T is the unit tesla). Refer to “(1),” not “Eq. (1)” or “equation (1),” except at the beginning of a sentence: “Equation (1) is”

E. Other Recommendations

Use one space after periods and colons. Hyphenate complex modifiers: “zero-field-cooled magnetization.” Avoid dangling participles, such as, “Using (1), the potential was calculated.” [It is not clear who or what used (1).] Write instead, “The potential was calculated by using (1),” or “Using (1), we calculated the potential.”

Use a zero before decimal points: “0.25,” not “.25.” Use “ cm^3 ,” not “cc.” Indicate sample dimensions as “0.1 cm \times 0.2 cm,” not “0.1 \times 0.2 cm^2 .” The abbreviation for “seconds” is “s,” not “sec.” Do not mix complete spellings and abbreviations of units: use “Wb/m²” or “webers per square meter,” not “webers/m².” When expressing a range of values, write “7 to 9” or “7-9,” not “7~9.”

A parenthetical statement at the end of a sentence is punctuated outside of the closing parenthesis (like this). (A parenthetical sentence is punctuated within the parentheses.) In American English, periods and commas are within quotation marks, like “this period.” Other punctuation is “outside”! Avoid contractions; for example, write “do not” instead of “don’t.” The serial comma is preferred: “A, B, and C” instead of “A, B and C.”

If you wish, you may write in the first person singular or plural and use the active voice (“I observed that ...” or “We observed that ...” instead of “It was observed that ...”). Remember to check spelling. If your native language is not English, please get a native English-speaking colleague to carefully proofread your paper.

VI. SOME COMMON MISTAKES

The word “data” is plural, not singular. The subscript for the permeability of vacuum μ_0 is zero, not a lowercase letter “o.” The term for residual magnetization is “remanence”; the

adjective is “remanent”; do not write “remnance” or “remnant.” Use the word “micrometer” instead of “micron.” A graph within a graph is an “inset,” not an “insert.” The word “alternatively” is preferred to the word “alternately” (unless you really mean something that alternates). Use the word “whereas” instead of “while” (unless you are referring to simultaneous events). Do not use the word “essentially” to mean “approximately” or “effectively.” Do not use the word “issue” as a euphemism for “problem.” When compositions are not specified, separate chemical symbols by en-dashes; for example, “NiMn” indicates the intermetallic compound $\text{Ni}_{0.5}\text{Mn}_{0.5}$ whereas “Ni–Mn” indicates an alloy of some composition $\text{Ni}_x\text{Mn}_{1-x}$.

Be aware of the different meanings of the homophones “affect” (usually a verb) and “effect” (usually a noun), “complement” and “compliment,” “discreet” and “discrete,” “principal” (e.g., “principal investigator”) and “principle” (e.g., “principle of measurement”). Do not confuse “imply” and “infer.”

Prefixes such as “non,” “sub,” “micro,” “multi,” and “ultra” are not independent words; they should be joined to the words they modify, usually without a hyphen. There is no period after the “et” in the Latin abbreviation “*et al.*” (it is also italicized). The abbreviation “i.e.,” means “that is,” and the abbreviation “e.g.,” means “for example” (these abbreviations are not italicized).

An excellent style manual and source of information for science writers is [9].

VII. EDITORIAL POLICY

Each manuscript submitted is subjected to the following review procedure:

- It is reviewed by the editor for general suitability for this publication
- If it is judged suitable, two reviewers are selected and a single-blinded review process takes place
- Based on the recommendations of the reviewers, the editor then decides whether the particular paper should be accepted as is, revised or rejected.

Do not submit a paper you have submitted or published elsewhere. Do not publish “preliminary” data or results. The submitting author is responsible for obtaining agreement of all coauthors and any consent required from sponsors before submitting a paper. It is the obligation of the authors to cite relevant prior work.

Every paper submitted to “Electronics” journal are single-blind reviewed. For conference-related papers, the decision to accept or reject a paper is made by the conference editors and publications committee; the recommendations of the referees are advisory only. Undecipherable English is a valid reason for rejection.

VIII. PUBLICATION PRINCIPLES

The contents of “Electronics” are peer-reviewed and archival. The “Electronics” publishes scholarly articles of

archival value as well as tutorial expositions and critical reviews of classical subjects and topics of current interest.

Authors should consider the following points:

- 1) Technical papers submitted for publication must advance the state of knowledge and must cite relevant prior work.
- 2) The length of a submitted paper should be commensurate with the importance, or appropriate to the complexity, of the work. For example, an obvious extension of previously published work might not be appropriate for publication or might be adequately treated in just a few pages.
- 3) Authors must convince both peer reviewers and the editors of the scientific and technical merit of a paper; the standards of proof are higher when extraordinary or unexpected results are reported.
- 4) Because replication is required for scientific progress, papers submitted for publication must provide sufficient information to allow readers to perform similar experiments or calculations and use the reported results. Although not everything need be disclosed, a paper must contain new, useable, and fully described information. For example, a specimen’s chemical composition need not be reported if the main purpose of a paper is to introduce a new measurement technique. Authors should expect to be challenged by reviewers if the results are not supported by adequate data and critical details.
- 5) Papers that describe ongoing work or announce the latest technical achievement, which are suitable for presentation at a professional conference, may not be appropriate for publication in “Electronics”.

IX. CONCLUSION

A conclusion section is not required. Although a conclusion may review the main points of the paper, do not replicate the abstract as the conclusion. A conclusion might elaborate on the importance of the work or suggest applications and extensions.

APPENDIX

Appendices, if needed, appear before the acknowledgment.

ACKNOWLEDGMENT

The preferred spelling of the word “acknowledgment” in American English is without an “e” after the “g.” Use the singular heading even if you have many acknowledgments. Avoid expressions such as “One of us (S.B.A.) would like to thank” Instead, write “F. A. Author thanks” **Sponsor and financial support acknowledgments are placed in the unnumbered footnote on the first page, not here.**

REFERENCES

- [1] G. O. Young, “Synthetic structure of industrial plastics (Book style with paper title and editor),” in *Plastics*, 2nd ed. vol. 3, J. Peters, Ed. New York: McGraw-Hill, 1964, pp. 15–64.
- [2] W.-K. Chen, *Linear Networks and Systems* (Book style). Belmont, CA: Wadsworth, 1993, pp. 123–135.

- [3] H. Poor, *An Introduction to Signal Detection and Estimation*. New York: Springer-Verlag, 1985, ch. 4.
- [4] B. Smith, "An approach to graphs of linear forms (Unpublished work style)," unpublished.
- [5] E. H. Miller, "A note on reflector arrays (Periodical style—Accepted for publication)," *IEEE Trans. Antennas Propagat.*, to be published.
- [6] J. Wang, "Fundamentals of erbium-doped fiber amplifiers arrays (Periodical style—Submitted for publication)," *IEEE J. Quantum Electron.*, submitted for publication.
- [7] C. J. Kaufman, Rocky Mountain Research Lab., Boulder, CO, private communication, May 1995.
- [8] Y. Yorozu, M. Hirano, K. Oka, and Y. Tagawa, "Electron spectroscopy studies on magneto-optical media and plastic substrate interfaces (Translation Journals style)," *IEEE Transl. J. Magn.Jpn.*, vol. 2, Aug. 1987, pp. 740–741 [Dig. 9th Annu. Conf. Magnetism Japan, 1982, p. 301].
- [9] M. Young, *The Technical Writers Handbook*. Mill Valley, CA: University Science, 1989.
- [10] J. U. Duncombe, "Infrared navigation—Part I: An assessment of feasibility (Periodical style)," *IEEE Trans. Electron Devices*, vol. ED-11, pp. 34–39, Jan. 1959.
- [11] S. Chen, B. Mulgrew, and P. M. Grant, "A clustering technique for digital communications channel equalization using radial basis function networks," *IEEE Trans. Neural Networks*, vol. 4, pp. 570–578, Jul. 1993.
- [12] R. W. Lucky, "Automatic equalization for digital communication," *Bell Syst. Tech. J.*, vol. 44, no. 4, pp. 547–588, Apr. 1965.
- [13] S. P. Bingulac, "On the compatibility of adaptive controllers (Published Conference Proceedings style)," in *Proc. 4th Annu. Allerton Conf. Circuits and Systems Theory*, New York, 1994, pp. 8–16.
- [14] G. R. Faulhaber, "Design of service systems with priority reservation," in *Conf. Rec. 1995 IEEE Int. Conf. Communications*, pp. 3–8.
- [15] W. D. Doyle, "Magnetization reversal in films with biaxial anisotropy," in *1987 Proc. INTERMAG Conf.*, pp. 2.2-1–2.2-6.
- [16] G. W. Juette and L. E. Zeffanella, "Radio noise currents in short sections on bundle conductors (Presented Conference Paper style)," presented at the IEEE Summer Power Meeting, Dallas, TX, Jun. 22–27, 1990, Paper 90 SM 690-0 PWRS.
- [17] J. G. Kreifeldt, "An analysis of surface-detected EMG as an amplitude-modulated noise," presented at the 1989 Int. Conf. Medicine and Biological Engineering, Chicago, IL.
- [18] J. Williams, "Narrow-band analyzer (Thesis or Dissertation style)," Ph.D. dissertation, Dept. Elect. Eng., Harvard Univ., Cambridge, MA, 1993.
- [19] N. Kawasaki, "Parametric study of thermal and chemical nonequilibrium nozzle flow," M.S. thesis, Dept. Electron. Eng., Osaka Univ., Osaka, Japan, 1993.
- [20] J. P. Wilkinson, "Nonlinear resonant circuit devices (Patent style)," U.S. Patent 3 624 12, July 16, 1990.
- [21] *IEEE Criteria for Class IE Electric Systems* (Standards style), IEEE Standard 308, 1969.
- [22] *Letter Symbols for Quantities*, ANSI Standard Y10.5-1968.
- [23] R. E. Haskell and C. T. Case, "Transient signal propagation in lossless isotropic plasmas (Report style)," USAF Cambridge Res. Lab., Cambridge, MA Rep. ARCRL-66-234 (II), 1994, vol. 2.
- [24] E. E. Reber, R. L. Michell, and C. J. Carter, "Oxygen absorption in the Earth's atmosphere," Aerospace Corp., Los Angeles, CA, Tech. Rep. TR-0200 (420-46)-3, Nov. 1988.
- [25] (Handbook style) *Transmission Systems for Communications*, 3rd ed., Western Electric Co., Winston-Salem, NC, 1985, pp. 44–60.
- [26] *Motorola Semiconductor Data Manual*, Motorola Semiconductor Products Inc., Phoenix, AZ, 1989.
- [27] (Basic Book/Monograph Online Sources) J. K. Author. (year, month, day). Title (edition) [Type of medium]. Volume (issue). Available: [http://www.\(URL\)](http://www.(URL))
- [28] J. Jones. (1991, May 10). Networks (2nd ed.) [Online]. Available: <http://www.atm.com>
- [29] (Journal Online Sources style) K. Author. (year, month). Title. *Journal* [Type of medium]. Volume(issue), paging if given. Available: [http://www.\(URL\)](http://www.(URL))
- [30] R. J. Vidmar. (1992, August). On the use of atmospheric plasmas as electromagnetic reflectors. *IEEE Trans. Plasma Sci.* [Online]. 21(3), pp. 876–880. Available: <http://www.halcyon.com/pub/journals/21ps03-vidmar>

Instruction for Authors

Editorial objectives

In the journal "Electronics", the scientific papers from different fields of electronics and electrical engineering in the broadest sense are published. Main topics are electronics, automatics, telecommunications, computer techniques, power engineering, nuclear and medical electronics, analysis and synthesis of electronic circuits and systems, new technologies and materials in electronics etc. The main emphasis of papers should be on methods and new techniques, or the application of existing techniques in a novel way.

The reviewing process

Each manuscript submitted is subjected to the following review procedures:

- It is reviewed by the editor for general suitability for this publication;
- If it is judged suitable, two reviewers are selected and a double-blind review process takes place;
- Based on the recommendations of the reviewers, the editor then decides whether the particular paper should be accepted as it is, revised or rejected.

Submissions Process

The manuscripts are to be delivered to the editor by e-mail: electronics@etfbl.net.

Manuscripts have to be prepared in accordance with the instructions given in the template for paper preparation that can be found on the journal's web page (www.electronics.etfbl.net).

Authors should note that proofs are not supplied prior to publication and ensure that the paper submitted is complete and in its final form.

Copyright

Articles submitted to the journal should be original contributions and should not be under consideration for any other publication at the same time. Authors submitting articles for publication warrant that the work is not an infringement of any existing copyright and will indemnify the publisher against any breach of such warranty. For ease of dissemination and to ensure proper policing of use, papers and contributions become the legal copyright of the publisher unless otherwise agreed.

ELECTRONICS, VOL. 20, NO. 1, JUNE 2016

PAPERS

PREVENTIVE THERMOGRAPHIC DIAGNOSTIC OF A HV BUSBAR DISCONNECTOR.....	3
Predrag Šaraba, Zoran Ljuboje, Božidar Popović and Dražan Krsmanović	
DESIGN OF TERNARY CONTENT-ADDRESSABLE MEMORIES WITH DYNAMICALLY POWER-GATED STORAGE CELLS USING FINFETS.....	9
Meng-Chou Chang, Kai-Lun He and Yu-Chieh Wang	
AN IMPROVED DESIGN OF GALLAGER MAPPING FOR LDPC-CODED BICM-ID SYSTEM.....	16
Lin Zhou, Weicheng Huang, Shengliang Peng, Yan Chen and Yucheng He	
DESIGN AND IMPLEMENTATION OF A NOVEL DIRECTIONAL COUPLER FOR UHF RFID READER.....	22
Jianxiong Li, Shanlin Song, Xiaoyu Chen, Hua Nian and Weiguang Shi	
HIGH DIMENSIONAL ELECTROMAGNETIC INTERFERENCE SIGNAL CLUSTERING BASED ON SOM NEURAL NETWORK.....	27
Di Zhao, Shaofeng Xu and Hongyi Li	
ACTIVE COMB FILTER USING VOLTAGE DIFFERENCING TRANSCONDUCTANCE AMPLIFIERS.....	32
Dinesh Prasad, Akshat Jain, Pankaj Dhingra and Aditya Panchal	
LOW VOLTAGE MIXED-MODE MULTI PHASE OSCILLATOR USING SINGLE FDCCII.....	36
J. Mohan, B. Chaturvedi and S. Maheshwari	

ISSN 1450-5843

UDK 621.38